TABLE OF CONTENTS

LIST OF FIGURES iii

Chapter 1 INTRODUCTION.....1
1.1 Overview 1
1.2 Previous Research.....5
1.2.1 Radiated Noise.....5
1.2.2 Laser Doppler Vibrometry.....7
1.2.3 Nearfield Acoustical Holography.....7
1.2.4 Accelerometers in Contact Patch.....12
1.2.5 Modeling Static, Time-Invariant Portion of Accelerometer.....12
1.3 Research Objectives 13
1.4 Experimental Approach.....14

Chapter 2 EXPERIMENTAL PROCEDURE 16
2.1 Equipment 16
2.1.1 Tires 16
2.1.2 Slip Ring.....17
2.1.3 Accelerometers 18
2.1.3.1 Embedded Accelerometers – Attempt #1.....19
2.1.3.2 Embedded Accelerometers – Attempt #2.....21
2.1.3.3 Embedded Accelerometers – Attempt #3.....22
2.1.3.4 Embedded Accelerometers – Attempt #4.....23
2.2 Frequencies of Resonance 25
2.3 Tire Testing.....25

Chapter 3 DATA PROCESSING 29
3.1 Recorded Signal.....29
3.2 Non-Radiating Component.....31
3.2.1 Analytic Model.....32
3.2.1.1 Verification of Model.....34
3.2.1.2 Comparison of Model to Recorded Signal.....36
3.2.2 Average of Several Rotations 41
3.2.3 Segmenting a Rotation.....42

Chapter RESULTS.....44
4.1 Single Rotation Time-Traces.....44
4.1.1 Various Speeds 44
4.1.2 Smooth and Rough Pavements 46
4.1.3 Radial, Tangential, and Axial Acceleration.....47
4.2 Analysis of Results.....48

4.2.1 Segment One Rotation....48
4.2.1.1 Smooth Pavement, Radial Acceleration....49
4.2.1.2 Rough Pavement, Radial Accelerations....52
4.2.1.3 Smooth Pavement, Tangential Acceleration....56
4.2.14 Smooth Pavement, Axial Acceleration....59
4.2.1.5 Vibration Spectra for Three Accelerometer Orientations....62
4.2.2 Removing Non-Radiating Component....66
4.2.2.1 Average Several Periods of Rotation....67
4.2.2.1.1 Various Speeds....67
4.2.2.1.2 Smooth and Rough Pavements....72
4.2.2.1.3 Radial, Axial, and Tangential Acceleration....80
4.2.2.2 Analytic Model....85

Chapter 5 CONCLUSION....91
5.1 Summary....91
5.2 Conclusions....92
5.3 Recommendations....93
5.4 Future Work....94

Bibliography....96

Appendix ADDITIONAL DATA....98

LIST OF FIGURES

Figure 1-1: Mechanisms producing tire/pavement interaction noise....4
Figure 1-2: Pass-by levels of power-train noise compared with tire/road noise Measured on dry pavement....6
Figure 1-3: Acoustic pressure reconstructed on the source plan (closest to the tire) In the frequency range 300-1550 Hz for a blank tire on smooth pavement 9
Figure 1-4: Acoustic pressure reconstructed on a source plan (closest to the tire) In the frequency range 300-1550 Hz for a blank tire on rough pavement....10
Figure 1-5: Acoustic pressure reconstructed on the source plan (closes to the tire) In the frequency range 300-1550 Hz for a ribbed tire on smooth pavement .11
Figure 1-6 Tire rotation through contact patch....13
Figure 2-1: Tire cross-section....17
Figure 2-2 Slip ring mounted on tire, connected to 4 accelerometers 18
Figure 2-3 Accelerometer mounting attempt #1: Accelerometer embedded directly into tire surface....20
Figure 2-4 Uncalibrated voltage output from DAT recorder for accelerometer mounted attempt #1 measured over two rotations 20
Figure 2-5: Accelerometer mounting attempt #2: Accelerometer embedded inside of tire on aluminum post 21
Figure 2-6: Uncalibrated voltage output from DAT recorder for attempt #2 measured over two tire rotations 22
Figure 2-7: Accelerometer mounting attempt #3: Accelerometer mounted on aluminum disk....23
Figure 2-8: Accelerometer mounting attempt #4: Accelerometer mounted on aluminum disk and wire drawn out through sidewall of tire 24
Figure 2-9: Uncalibrated voltage output from DAT recorder for attempt #4 measured over two tire rotations 24
Figure 2-10: Diagram of tire with accelerometers embedded in three orientations 26
Figure 2-11: Goodyear test setup with tire on road wheel....27
Figure 2-12: Rough (left) and smooth (right) pavements on Goodyear road-wheel 28
Figure 3-1: Five rotations of radial acceleration at 20 mph on smooth pavement 30
Figure 3-2: One rotation of radial acceleration at 20 mph on smooth pavement 31
Figure 3-3: Shear and normal pressure experienced by the surface of the tire as it rolls through the contact patch....37
Figure 3-4: Diagram of rolling tire identifying rotation and contact patch size 38
Figure 3-5: Analytic model of one rotation of tangential and radial displacement 39
Figure 3-6: Analytic model of one rotation of tangential and radial acceleration....40
Figure 3-7: Comparison of theoretical model to measured radial acceleration....41
Figure 3-8: One rotation of radial acceleration with segmented entrance and exit to contact patch....43
Figure 4-1: One rotation of radial acceleration on smooth pavement at various speeds....44
Figure 4-2: Average minimum acceleration levels versus speed....46
Figure 4-3: One rotation of radial acceleration at 20 mph on smooth and rough pavement 47
Figure 4-4: Radial, tangential, and axial acceleration on smooth pavement at 40 mph.48

Figure 4-5: Segmented entrance and exit to contact patch of one rotation of radial Acceleration measured on smooth pavement at 40 mph 49
Figure 4-6: Vibration spectra of segments in entrance to contact patch measured in the radial direction on smooth pavement at 40 mph. The frequency is 6 Hz 50
Figure 4-7: Vibration spectra of segments in exit to contact patch measured in the radial direction on smooth pavement at 40 mph. The frequency is resolution is 6 Hz 51
Figure 4-8: Vibration levels at entrance and exit to the contact patch measured in the radial direction on smooth pavement at 40 mph. The frequency resolution is 6 Hz 52
Figure 4-7: Segmented entrance and exit to contact patch of one rotation of radial acceleration measured on rough pavement at 40 mph 53
Figure 4-10: Vibration spectra of segments in entrance to contact patch measured in the radial direction on rough pavement at 40 mph. The frequency resolution is 6 Hz 54
Figure 4-11: Vibration spectra of segments in exit to contact patch measured in the radial direction on rough pavement at 40 mph. The frequency resolution is 6 Hz 55
Figure 4-12: Vibration levels at entrance and exit to the contact patch measured in the radial direction on rough pavement at 40 mph. The frequency resolution is 6 Hz 56
Figure 4-13: Segmented entrance and exit to contact patch of one rotation of t tangential acceleration measured on smooth pavement at 40 mph.....57
Figure 4-14: Vibration spectra of segments in entrance to contact patch measured in the tangential direction on smooth pavement at 40 mph. The frequency resolution is 6 Hz 58
Figure 4-15: Vibration spectra of segments in exit to contact patch measured in the tangential direction on smooth pavement at 40 mph. The frequency resolution is 6 Hz 59
Figure 4-16: Segmented entrance and exit to contact patch of one rotation of axial acceleration measured on smooth pavement at 40 mph.....60
Figure 4-17: Vibration spectra of segments in entrance to contact patch measured in the axial direction on smooth pavement at 40 mph. The frequency resolution is 6 Hz 61
Figure 4-18: Vibration spectra of segments in exit to contact patch measured in the axial direction on smooth pavement at 40 mph. The frequency resolution is 6 Hz 62
Figure 4-19: Comparison of radial, tangential, and axial acceleration over smooth pavement at 40 mph in segment 6 of the entrance to the contact patch. The frequency resolution is 6 Hz 63
Figure 4-20: Comparison of radial, tangential, and axial acceleration over smooth pavement at 40 mph in segment 7 of the exit to the contact patch. The frequency resolution is 6 Hz 64

Figure 4-21: Comparison of radial, tangential, and axial acceleration over smooth pavement at 20 mph in segment 6 of the exit to the contact patch. The frequency resolution is 6 Hz 65
Figure 4-22: Comparison of radial, tangential, and axial acceleration over smooth pavement at 20 mph in segment 7 of the exit to the contact patch. The frequency resolution is 6 Hz 66
Figure 4-23: Averages of twenty rotations of radial acceleration on smooth pavement at various speeds 68
Figure 4-24: Radiating component of radial acceleration on smooth pavement 69
Figure 4-25: Frequency spectra of radial acceleration at various speeds on smooth pavement. The frequency resolution is 6 Hz. 70
Figure 4-26: Frequency spectra of radiated noise measured at various speeds on smooth pavement. The frequency resolution is 6 Hz. 71
Figure 4-27: Averages of radial acceleration on smooth and rough pavements at 20 mph. 72
Figure 4-28: Radiating component of radial acceleration on smooth and rough pavement at 20 mph 73
Figure 4-29: Frequency spectra of radial acceleration at 20 mph on smooth and rough pavements. The frequency resolution is 6 Hz. 74
Figure 4-30: Radiated noise measured at 20 mph on smooth and rough pavements. The frequency resolution is 6 Hz 75
Figure 4-31: Transfer functions between radiated noise and measured radial acceleration vibration levels for all speeds on smooth pavement. The frequency resolution is 12 Hz 76
Figure 4-32: Transfer functions between radiated noise and measured radial acceleration vibration levels for all speeds on rough pavement. The frequency resolution is 12 Hz 77
Figure 4-33: Transfer functions between radiated noise and measured radial acceleration vibration levels for all speeds on smooth pavement with speeds 30-50 mph averaged 78
Figure 4-34: Transfer functions between radiated noise and measured radial acceleration vibration levels for all speeds on rough pavements with speeds 30-50 mph averaged 79
Figure 4-35: Transfer functions between radiated and measured radial acceleration vibration levels on smooth and rough pavements at speeds 30-50 mph averaged 80
Figure 4-36: Average of twenty rotations of radial, axial, and tangential acceleration on smooth pavement at 40 mph 81
Figure 4-37: Radiating component of radial, axial, and tangential acceleration on smooth pavement at 40 mph 82
Figure 4-38: Frequency spectra of radial, tangential, and axial acceleration on smooth pavement at 40 mph. The frequency resolution is 12 Hz 83
Figure 4-39: Average of twenty rotations of radial, axial, and tangential acceleration on smooth pavement at 20 mph 84
Figure 4-40: Radiating component of radial, axial, and tangential acceleration on smooth pavement at 20 mph 84

Figure 4-41: Frequency spectra of radial, tangential and axial acceleration on smooth pavement at 20 mph. The frequency resolution is 12 Hz 85
Figure 4-42: Analytic model compared with measured radial acceleration at 20 mph on smooth pavement 86
Figure 4-43: Radiated portion of the radial acceleration at 20 mph on smooth pavement determined by subtracting analytic model.....87
Figure 4-44: Radiating component of radial acceleration measured on smooth pavement at speeds of 10-50 mph, computed by subtracting analytic model.....88
Figure 4-45: Frequency spectra of radial acceleration measured at various speeds on smooth pavement determined by subtracting analytic model. The frequency resolution is 12 Hz 89
Figure 4-46: Comparison of the analytic model with the averaged radial acceleration for 20 mph on smooth pavement 90
Figure A-1: One rotation of radial acceleration at 40 mph on smooth and rough pavement 98
Figure A-1: Radial acceleration on smooth and rough pavement at 40 mph averaged over 20 rotations 99
Figure A-3: Radiating component of radial acceleration on smooth and rough pavements at 40 mph computed by subtracting the average of 20 rotations 100
Figure A-4: Frequency spectra of radial acceleration on smooth and rough pavements at 40 mph, computed after subtracting the average of 20 rotations from a single rotation. The frequency resolution is 12 Hz 101
Figure A-5: Frequency spectra of radiated noise measured over one rotation at 40 mph on smooth pavement and rough pavements. The frequency resolution is 12 Hz 102
Figure A-6: One rotation of radial, tangential, and axial acceleration on smooth pavement at 20 mph.....103
Figure A-7: Segmented time trace of radial acceleration on smooth pavement at 10 mph.....104
Figure A-8: Vibration spectra of segments in entrance to contact patch measured in the radial direction on smooth pavement at 10 mph. The frequency resolution is 6 Hz 105
Figure A-9: Vibration spectra of segments in exit to contact patch measured in the radial direction on smooth pavement at 10 mph. The frequency resolution is 6 Hz 106
Figure A-10: Segmented time trace of radial acceleration on smooth pavement at 20 mph 107
Figure A-11: Vibration spectra of segments in entrance to contact patch measured in the radial direction on smooth pavement at 20 mph. The frequency resolution is 6 Hz. 108
Figure A-12: Vibration spectra of segments in exit to contact patch measured in the radial direction on smooth pavement at 20 mph. The frequency resolution is 6 Hz 109

Figure A-13: Segmented time trace of radial acceleration on smooth pavement at 30 mph.....110
Figure A-14: Vibration spectra of segments in entrance to contact patch measured in the radial direction on smooth pavement at 30 mph. The frequency resolution is 6 Hz.....111
Figure A-15: Vibration spectra of segments in exit to contact patch measured in the radial direction on smooth pavement at 30 mph. The frequency resolution is 6 Hz.....112
Figure A-16: Segmented time trace of radial acceleration on smooth pavement at 50 mph.....113
Figure A-17: Vibration spectra of segments in entrance to contact patch measured in the radial direction on smooth pavement at 50 mph. The frequency resolution is 6 Hz.....114
Figure A-18: Vibration spectra of segments in exit to contact patch measured in the Radial direction on smooth pavement at 50 mph. The frequency resolution is 6 Hz.....115
Figure A-19: Segmented time trace of tangential acceleration on smooth pavement at 20 mph.....116
Figure A-20: Vibration spectra of segments in entrance to contact patch measured in the tangential direction on smooth pavement at 20 mph. The frequency resolution is 6 Hz.....117
Figure A-21: Vibration spectra of segments in exit to contact patch measured in the tangential direction on smooth pavement at 20 mph. The frequency resolution is 6 Hz.....118
Figure A-22: Segmented time trace of axial acceleration on smooth pavement at 20 mph.....119
Figure A-23: Vibration spectra of segments in entrance to contact patch measured in the axial direction on smooth pavement at 20 mph. The frequency resolution is 6 Hz.....120
Figure A-24: Vibration spectra of segments in exit to contact patch measured in the axial direction on smooth pavement at 20 mph. The frequency resolution is 6 Hz.....121
Figure A-25: Segmented time trace of radial acceleration on rough pavement at 20 mph.....122
Figure A-26: Vibration spectra of segments in entrance to contact patch measured in the radial direction on rough pavement at 20 mph. The frequency resolution is 6 Hz.....123
Figure A-27: Vibration spectra of segments in exit to contact patch measured in the Radial direction on rough pavement at 20 mph. The frequency resolution is 6 Hz.....124
Figure A-28: Analytic model of non-radiating component of radial acceleration for speeds of 10-20 mph.....125
Figure A-29: Analytic model compared with measured radial acceleration at 10 mph on smooth pavement.....126
Figure A-30: Analytic model compared with measured radial acceleration at 30 mph on smooth pavement.....127

Figure A-31: Analytic model compared with measured radial acceleration at 40 mph on smooth pavement 128
Figure A-32: Analytic model compared with measured radial acceleration at 50 mph on smooth pavement 129

Chapter 1

INTRODUCTION

1.1 Overview

Among many communities, traffic is a leading source of noise-related complaints. Not only is it a general nuisance, traffic noise also interferes with sleep, speech communication, and work performance. Caused by cars, trucks, buses, and motorcycles, road traffic is considered the most significant noise source in urbanized, industrial areas.

About 80 million people in Europe are exposed to A-weighted noise levels exceeding 65 dB during the daytime. At these levels, many complaints are made about the amount of noise. Busy urban areas typically will have A-weighted sound levels of 70 to 80 dB and because of urban growth and increased use of vehicles, levels will only increase unless action is taken to reduce the noise emission. [1]

Over the past few decades, measures have been taken to limit noise exposure in the European Union. In November 1996, the Green Paper [2] as published as a major step in developing a noise policy for the European Union. It identifies road traffic noise as a major problem and states that tires must be made quieter in order to reduce traffic noise. As of 1996, the A-weighted highway noise level limits in the European Union have been set at 74 dB for passenger cars, 78 dB for buses, and 80 dB for heavy trucks at a distance of 7.5 meters at speeds over 50 km/h (31 mph) in urban areas.

Noise limits in the United States are currently not as stringent as those in Europe. The federal government does not have any requirements for light vehicles, such as passenger cars; however A-weighted noise level limits for new trucks under full-throttle at low speed are set at 80 dB when measured at a distance of 7.5 meters from the truck. Some state and local governments have ordinances limiting light vehicle A-weighted noise levels to 86 or 90 dB. Vehicle manufacturers of cars used in the US generally comply with the 80 dB A-weighted sound level limit, which is similar to the European limits of the 1980's. These limits are based upon tests where the vehicle is run at full power and the power-train noise dominates. It has been found that tire noise dominates noise produced by the power-train when vehicles are driven at constant speeds. Because little has been done to reduce tire noise, the regulations only pertain to the noise produced by the power-train of the vehicle. [3]

According to the Federal Highway Administration, [4] traffic noise levels depend on traffic volume, traffic speed, pavement type, and number of trucks in the flow of traffic. If any of these factors are increased, noise levels are also increased. In order to counteract the high levels created by traffic, many different noise abatement measures can be implemented. These methods include highway noise barriers, a change in the terrain or vegetation, traffic reduction, an increase in distance between highway and populated areas, and building insulation. Despite the many methods to reduce noise exposure, the most efficient and cost-effective method is to reduce the noise at its source. [1]

At higher speeds, such as those typical on highways, the interaction of tires with pavement surfaces has the greatest contribution to the highway noise problem. Therefore,

it is important to look at the mechanisms producing tire/pavement interaction noise, which are shown in Figure 1-1. Tire/pavement interaction noise is produced by several mechanisms: the radial excitation and radiation of the tire casing due to tread pattern (a) and pavement roughness (b), the tangential excitation due to the stick/slip motion (c), the impact of the tread block at the leading edge (d), the release of the tread block at the trailing edge (e), and air pumping (f), which is the suction and ejection of air between the tire tread and pavement surface. These mechanisms and their effects depend upon the tire type and tread design in addition to the properties of the road surface. [1]

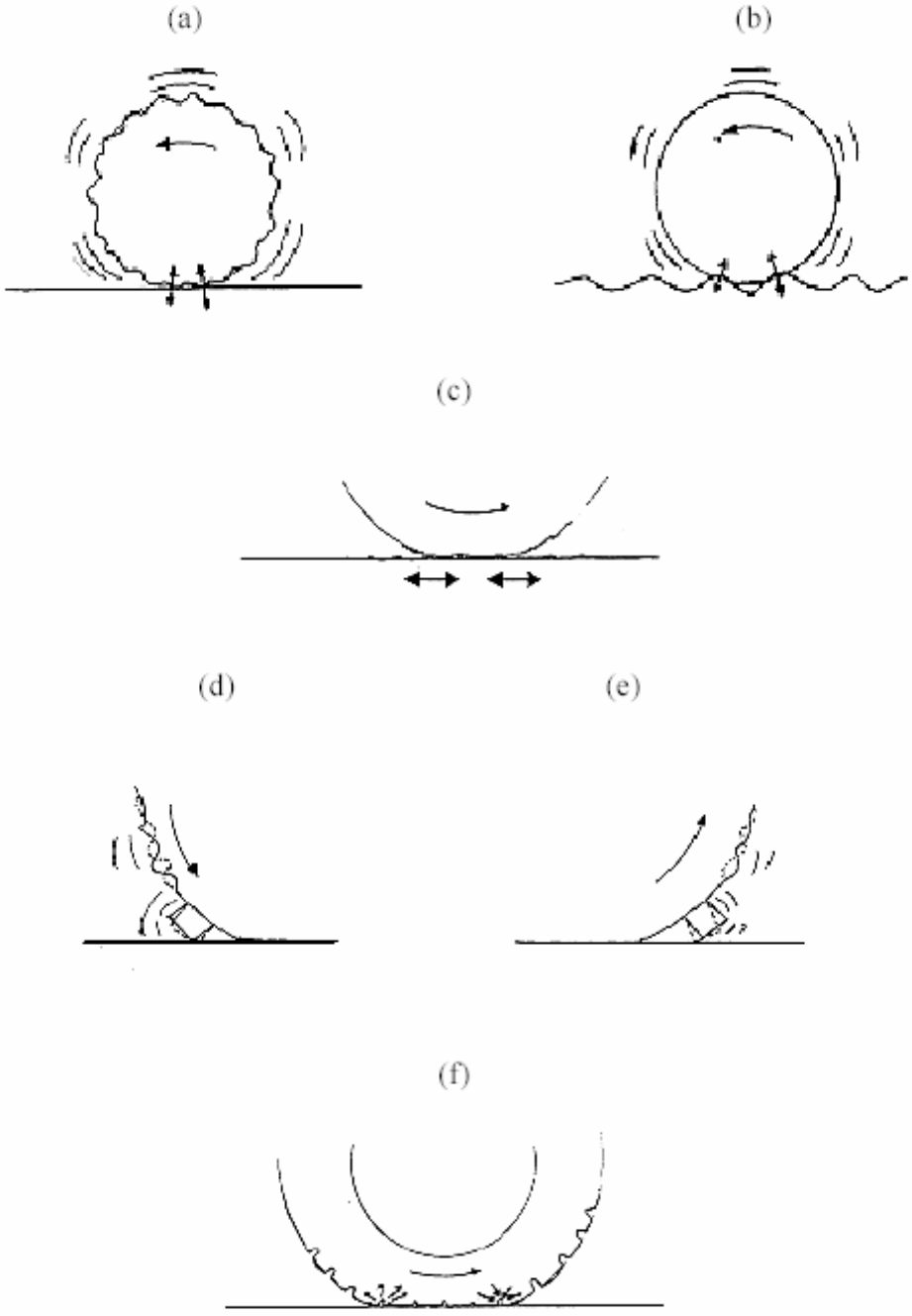

Figure 1-1: Mechanisms producing tire/pavement interaction noise.

1.2 Previous Research

The problem of tire noise has been a topic of research for many years. Much effort has been made to measure, localize, and model tire/pavement interaction noise. Previous methods of measuring tire noise include radiated noise measurements, laser vibrometry, nearfield acoustical holography, and vibration measurement using accelerometers mounted on the tire tread blocks.

1.2.1 Radiated Noise

In radiated noise measurements made by Ulf Sandberg [5] it was found that tire noise levels are higher than levels of power train noise above certain speeds. In pass-by tests, Sandberg measured vehicle noise radiated with and without the engine running. He found that the levels generated by tire/pavement interaction were higher than the noise levels produced by the power train at speeds above 50 km/hr (31 mph), as shown in Figure 1-2. In wet weather, tire noise levels are higher than power train noise levels at lower speeds because of the change in conditions between the tire and pavement.

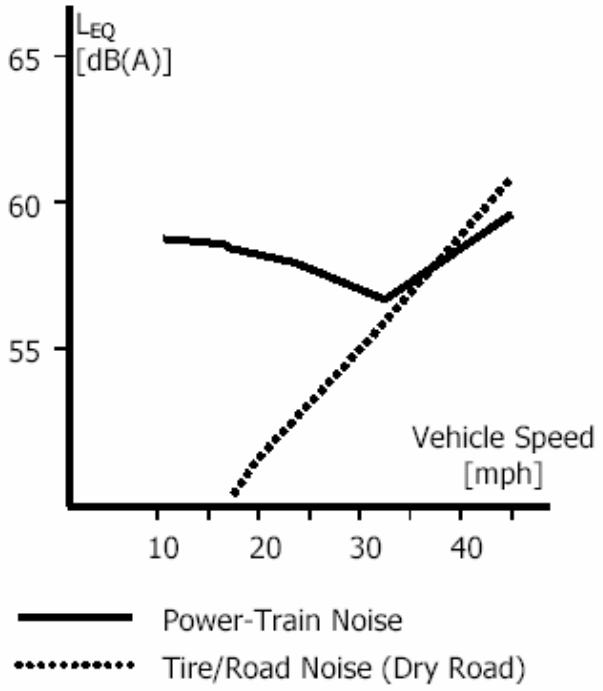

Figure 1-2: Pass-by levels of power-train noise compared with tire/road noise measured on dry pavement.

It was found that tire noise is the dominant noise source produced by automobiles at highway speeds and that it is more economical to reduce noise at its source than to build highway barriers in areas affected by highway noise. However, before effective treatment of tire/pavement interaction noise that will result in significant reductions beyond the reductions achieved so far can be developed, it will be necessary to develop a better understanding of the mechanisms producing the tire/pavement interaction noise. The noise is caused by the deformations of the tread as it enters and exits the contact patch, therefore measuring the deformations of the tire in the contact patch should help to better understand how the noise is produced.

Three approaches have been pursued in the past in attempts to measure vibration of the tire tread in the contact patch: non-contact vibration measurements, nearfield acoustic measurements, and accelerometers embedded in the tire tread.

1.2.2 Laser Doppler Vibrometry

Laser Doppler vibrometry is a non-contact method of measuring the vibration response of rolling tires. The laser Doppler vibrometer measures the normal velocity of the vibrating surface by reflecting the laser beam off of the vibrating surface. Although this is a reliable non-contact method of measuring the vibration response of rolling tires, it cannot be used to measure the vibrations within the tire/pavement contact patch.[6]

1.2.3 Nearfield Acoustical Holography

Nearfield acoustical holography (NAH) can be used to localize the noise radiation from tires by measuring the complex pressure at discrete points in a 2-dimensional plane located close to the rotating tire. Ruhala's [7] nearfield acoustic holography measurements were made using three different tires: blank, monopitch, and production tread. These tires were mounted on a trailer pulled along smooth and rough asphalt. A line array of eight uniformly-spaced microphones was scanned across the tire while three reference microphones remained fixed. The reference microphones were located close to the leading edge, the trailing edge, and the sidewall.

From these data, single and multiple coherence of the radiated noise with the noise measured by the reference microphones were mapped in the frequency range of 300 to 1500 Hz. An example of the coherence for the blank tire on smooth pavement at 56

km/hr (35 mph) is shown in Figure 1-3. In this figure, (b) shows that the dominant radiation is from the leading edge, (f) shows the high joint coherence between the leading edge and the sidewall, and (h) shows that all locations have low joint coherence. Figure 1-4 shows the coherence for the blank tire on rough pavement. Graph (h) shows that the rough pavement increases coherence between sources and that the leading and trailing edges excite the sidewall. From (b) and (f), it is apparent that the highest levels are at the leading edge. The coherence for the ribbed tire on smooth pavement is in Figure 1-5. Graphs (f) and (g) show there is low coherence between the contact patch edges and the sidewall. In graph (e), the coherence between the edges is 14%, whereas the blank tire's coherence is only 4%. This difference is attributed to air pumping between the tire tread and the pavement, which is not present in the blank tire.

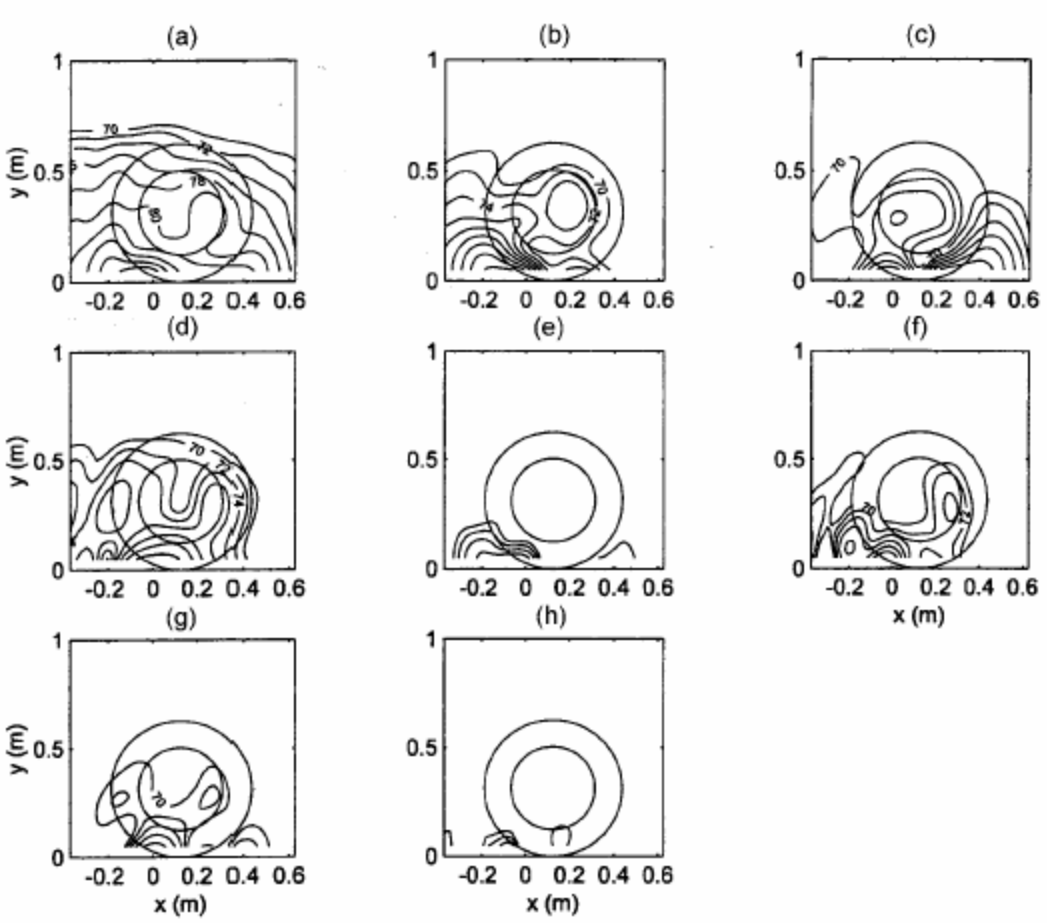

Figure 1-3: Acoustic pressure reconstructed on the source plan (closest to the tire) in the frequency range 300-1550 Hz for a blank tire on smooth pavement. Pressure fields shown are (a) total, (b) coherent to leading edge only, (c) trailing edge only, (d) sidewall only, (e) jointly coherent between leading edge and trailing edge, (f) between leading edge and sidewall, (g) between trailing edge and sidewall, and (h) jointly coherent among leading edge, trailing edge, and sidewall.

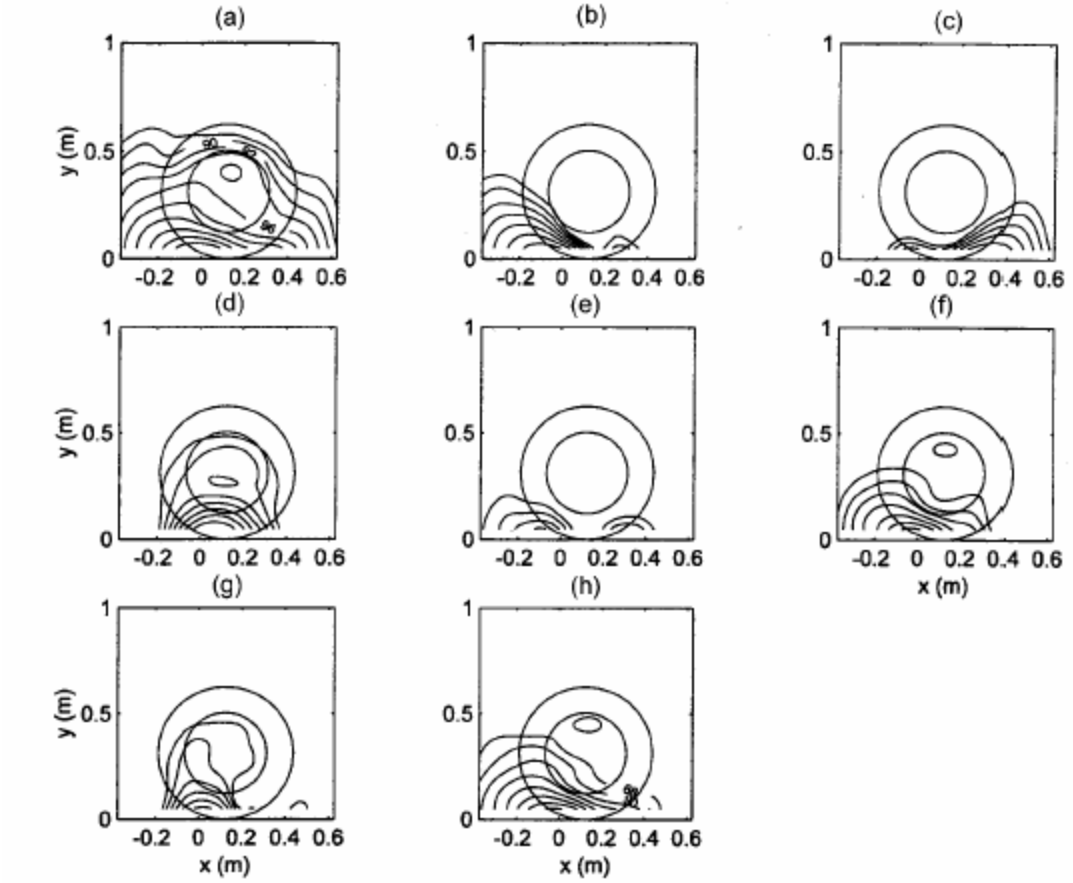

Figure 1.4: Acoustic pressure reconstructed on the source plan (closest to the tire) in the frequency range 300-1550 Hz for a blank tire on rough pavement. Pressure fields shown are (a) total, (b) coherent to leading edge only, (c) trailing edge only, (d) sidewall only, (e) jointly coherent between leading edge and trailing edge, (f) between leading edge and sidewall, (g) between trailing edge and sidewall, and (h) jointly coherent among leading edge, trailing edge, and sidewall.

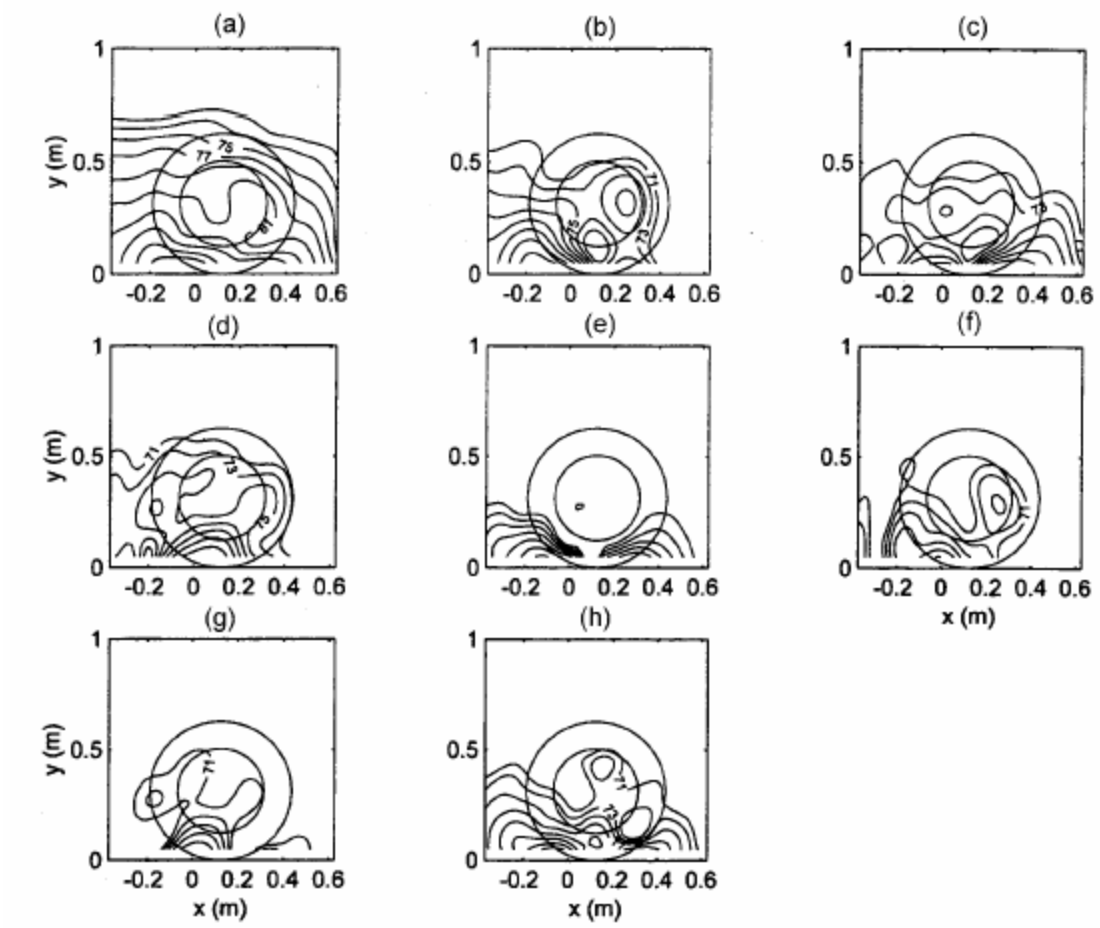

Figure 1-5: Acoustic pressure reconstructed on the source plan (closest to the tire) in the frequency range 300-1550 Hz for a ribbed tire on smooth pavement. Pressure fields shown are (a) total, (b) coherent to leading edge only, (c) trailing edge only, (d) sidewall only, (e) jointly coherent between leading edge and trailing edge, (f) between leading edge and sidewall, (g) between trailing edge and sidewall, and (h) jointly coherent among leading edge, trailing edge, and sidewall.

Generally, the NAH results show that the maximum radiation was local to the entrance and exit of the contact patch of a blank tire and that on a ribbed tire the air pumping in the tread grooves increases the acoustic radiation. Because it was found that the maximum radiation due to tire vibration exists near the tire/pavement contact patch, this location is the primary area of investigation for this thesis.

1.2.4 Accelerometers in Contact Patch

Jennewein and Bergmann [8,9] also recognized that when the tire tread element rotated through the contact patch, the excitation experienced by the tire as it enters and exits the contact patch produces large vibrations local to the contact patch. To examine the vibrations produced in this area, Jennewein and Bergmann mounted small accelerometers on the sides of the tread blocks, inside thread grooves, and at the bottom of the tread grooves of the tires and measured the radial and tangential acceleration. Three key parts of the vibration generated during one rotation were identified as the leading edge, contact patch, and trailing edge. Because of the flattening of the tire as the accelerometers moved through the contact patch, there is a static, time-invariant portion of the signal from the accelerometer that does not radiate noise. To study the signal, rather than removing the non-radiating portion, they separated the time history into the three sections, the leading edge, the contact patch, and the trailing edge, and analyzed them separately.

1.2.5 Modeling Static, Time-Invariant Portion of Acceleration

Kropp [10] and Heckl [11] both looked at methods of modeling the vibration of the outer surface of the tire. Their models were based on the circular ring model developed by Boehm so that the model was two-dimensional and predicted the radial and tangential displacement. The second derivatives of the displacements consequently determine the radial and tangential acceleration. This analytic model is used in this thesis

to model the non-radiating portion of the acceleration signal discussed in Jennewein and Bergmann's work.

1.3 Research Objectives

Because, as shown by Ruhala [7], the maximum radiation is produced from near the leading and trailing edges of the contact patch, the objective of this thesis is to measure the vibration response of the tire in the regions close to the contact patch where most of the radiation originates. The first step in this process is to embed accelerometers into the surface of blank tires to measure the vibrations at the entrance and exit to the contact patch and to extract from these measurements that portion of the measurement signal associated with the radiation by removing the time-invariant signal. The resulting acceleration signal would include the time-invariant, non-radiating component caused by the rotation of the tire as the accelerometers rotate through the contact patch, which is the flattened portion of the tire illustrated in Figure 1-6 .

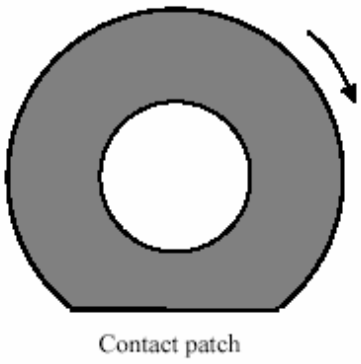

Figure 1-6: Tire rotation through contact patch.

Several methods are used to analyze the measured signals from the accelerometer. First, a single rotation is segmented around the contact patch so that different regions can be analyzed as the accelerometer approaches and exits the contact patch. Finally, two approaches will be considered to remove the time-invariant signal: the first is to average the measured signal over several rotations to isolate the time-invariant signal and the second is to use an analytic model to predict the time-invariant signal. Then the time-invariant signal is removed from the recorded signal. After removing the non-radiating, time-invariant signal, the non-time-invariant vibration response is compared to the radiated noise of the tire.

1.4 Experimental Approach

In order to measure the vibration response of the tire at the entrance and exit to the contact patch, accelerometers were embedded in the tread near the surface of the tire. After several attempts, a successful method was found to produce the desired acceleration signal. With the wheel mounted on a car, trial runs were made at the Pennsylvania Transportation Institute test track at Penn State University to determine if the accelerometer and wiring survived and produced reasonable results before conducting measurements at the Goodyear test facility in Akron, Ohio. At Goodyear, the wheel was mounted to run on the road wheel in a semi-anechoic chamber. The accelerometers were mounted in three orientations: radial, tangential, and axial. The speed of the tire was varied and measurements conducted on two wheel/pavement surfaces: a smooth and a rough surface. Microphones were placed nearby to measure the radiated noise

simultaneously with the tire vibration measurements. The experimental procedure will be discussed more in Chapter 2. The methods used to find the radiating components of the vibrations of the tire are discussed in Chapter 3.

Chapter 2

EXPERIMENTAL PROCEDURE

2.1 Equipment

2.1.1 Tires

The tire used in this research was a full tread-depth, blank tire of size P225/60R16 provided by Goodyear. The numbers given in the size specifications indicate the different dimensions of the tire. For this tire, the section width is 225 millimeters and the wheel diameter is 16 inches. The aspect ratio, or section height over section width, is 60%, which indicates that the section height is 135 millimeters. By combining the section height and wheel diameter, it is determined the outer tire diameter is 26.63 inches or 0.6764 meters. A cross-section can be seen in Figure 2-1. For a more in-depth description of radial tires, see the references used in the PhD thesis of Richard Ruhala. [7,12,13,14].

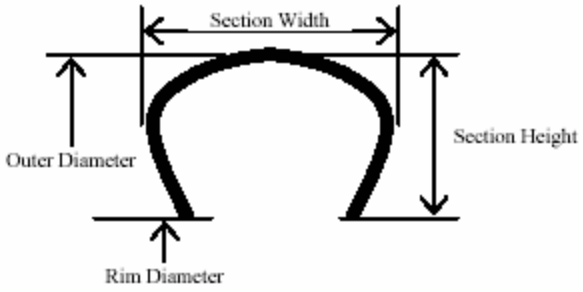

Figure **2-1**: Tire cross-section.

2.1.2 Slip Ring

In order to connect the accelerometers to data collection equipment, a slip ring was used. Initially a 4-channel slip ring was used and later an 8-channel slip ring was installed to accommodate more accelerometers. The base slip ring was attached to the wheel via the lug nuts and the top attached with a clamp with arms that were attached to a stationary surface using rope and duct tape. The 4-channel slip ring can be seen mounted on a tire in Figure 2-2.

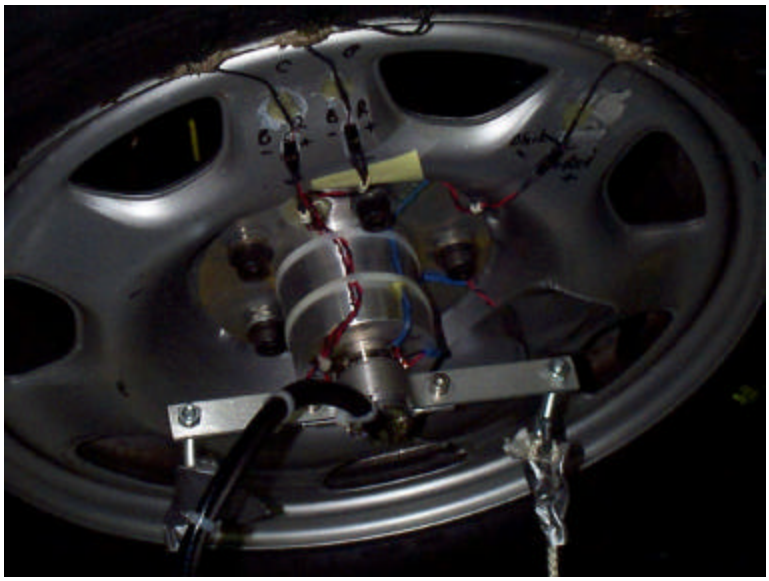

Figure **2-2**: Slip ring mounted on tire, connected to 4 accelerometers.

2.1.3 Accelerometers

The selection and mounting of the accelerometers were important parts of this research. Endevco 2250AM1-10 accelerometers were chosen because of their small size. Their sensitivity was approximately 10 mV/g and each weighed only 0.4 grams. The accelerometer dimensions were 0.5 cm in width, 0.75 cm in length, and 0.4 cm thick. The low weight of the accelerometer reduced the mass-loading effect on the measurements and the small size permitted them to be easily embedded into the tread band of a tire such that local vibration could be measured. The top surface of the accelerometers were approximately 3.5 mm below the surface of the tire tread where the desired vibration was to be measured.

Several attempts were made to embed the accelerometers within the tire. The objective was to measure the vibration as close to the surface of the tire as possible while the accelerometer moved through the entrance and exit to the contact patch. After the accelerometer was embedded into the tire, the setup was tested to ensure the accelerometer would operate successfully. The criteria for its success included: survival during contact of the tire with the pavement as the accelerometer moved through the contact patch, ability to measure the desired vibration at the tire surface, and knowledge that the vibration response was minimally affected by the presence of the accelerometers.

In order to test each setup, the tire with the embedded accelerometer was mounted on a car and the accelerometer output was connected through the slip ring to a PCB signal conditioner and a 2-channel Sony digital audio tape (DAT) recorder, model TCD-D3. The resulting signals were then viewed in Matlab to check their validity.

2.1.3.1 Embedding Accelerometers - Attempt #1

The first attempt to embed the accelerometer in the surface of the blank tire was to place the accelerometer directly into the surface of the tire under a rubber plug as shown in Figure 2-3 . The wire was routed to the slip ring in a groove cut in the tread. The vehicle was driven slowly at first, but the signal was lost after the speed was increased to 15 miles per hour. As the accelerometer traveled through the contact patch and hit the pavement, the accelerometer was compressed and the wiring eventually broke. Because the accelerometer was compressed, the resulting signal showed that the

accelerometer was reacting as a pressure sensor. An example of two rotations of the recorded signal at 8 miles per hour is given in Figure 2-4 .

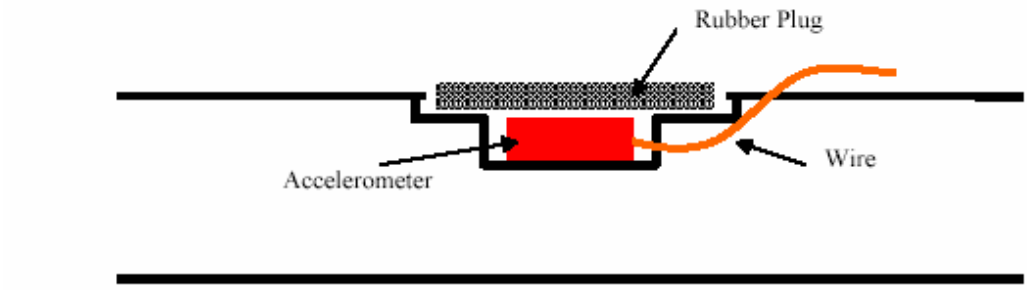

Figure **2-3**: Accelerometer mounting attempt #1: Accelerometer embedded directly into tire surface.

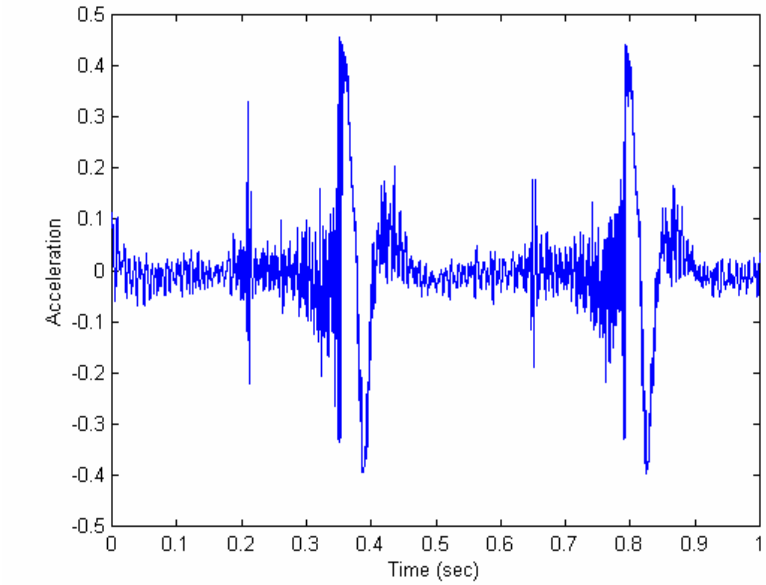

Figure **2-4**: Uncalibrated voltage output from DAT recorder for accelerometer mounting attempt #1 measured over two tire rotations.

2.1.3.2 Embedding Accelerometers - Attempt #2

In the next attempt to embed the accelerometer, extra effort was made to prevent the sensor from being compressed. The accelerometer was mounted inside of the tire on the end of an aluminum post that went through the thickness of the tire, as seen in Figure 2-5. The accelerometer did not fail and the results were examined by comparing the vibrations measured by the mounted accelerometer with those measured by an accelerometer placed on the surface of the tire, which was held stationary and excited with a shaker. The vibrations between the embedded and surface accelerometers did not match and it was concluded that the vibrations measured with the embedded accelerometer were averaging the vibrations through the thickness of the tire and therefore acting like a low-pass filter instead of sensing the surface vibrations. An example of two rotations of the signal at 10 miles per hour is given in Figure 2-6.

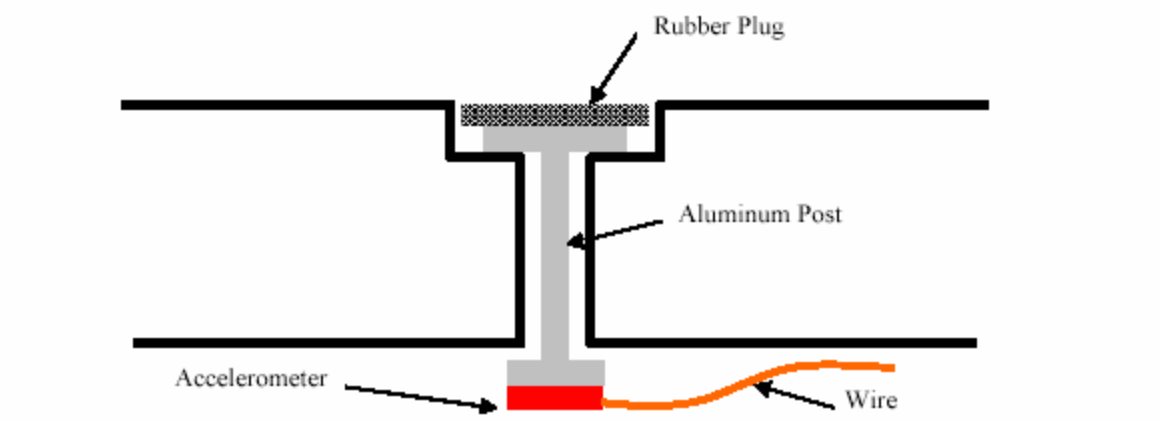

Figure **2-5**: Accelerometer mounting attempt #2: Accelerometer embedded inside of tire on aluminum post.

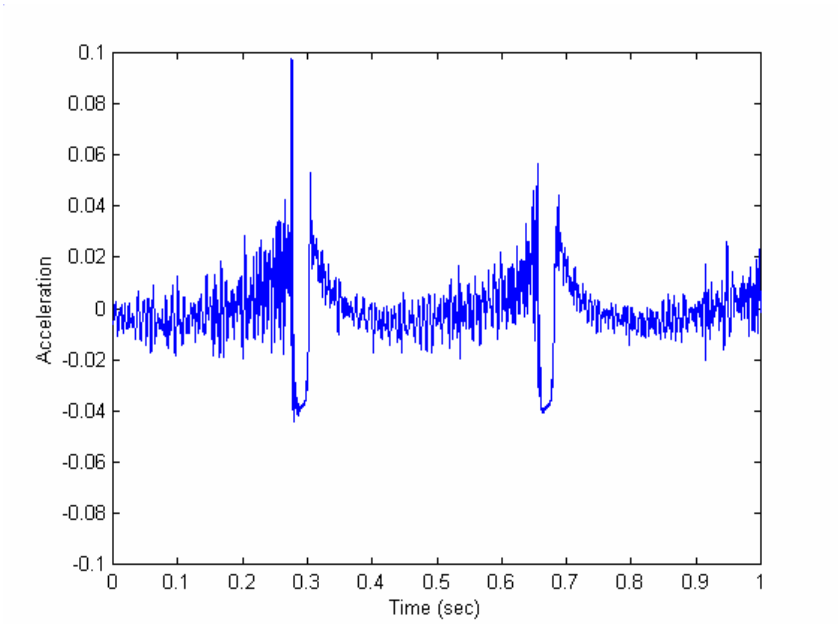

Figure **2-6**: Uncalibrated voltage output from DAT recorder for attempt #2 measured over two tire rotations.

2.1.3.3 Embedding Accelerometers - Attempt #3

For the third attempt to embed the accelerometer, it was determined that the accelerometer must be placed closer to the vibrating surface where the radiation occurs. The accelerometer was mounted on an aluminum disk with a rubber seal over it and the wire was run across the surface of the tire. This setup can be seen in Figure 2-7. Unfortunately this method also failed, although it was only due to the breakage of the wire. This was because the wire was not able to withstand the large strains produced as the accelerometer traveled through the contact patch.

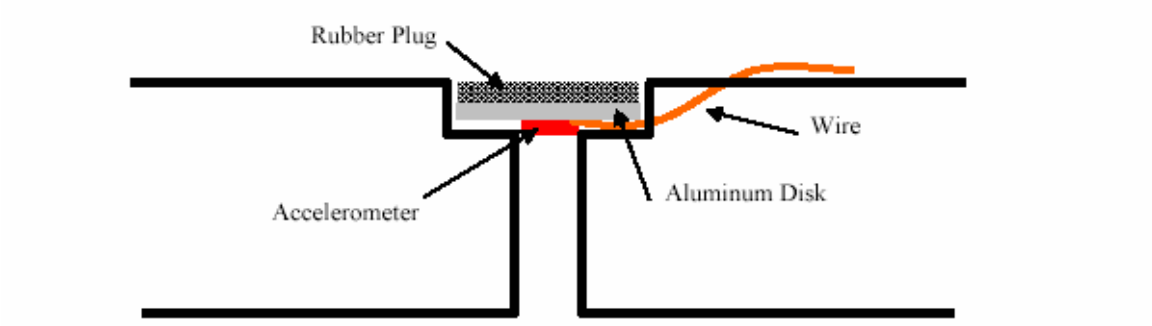

Figure **2-7**: Accelerometer mounting attempt #3: Accelerometer mounted on aluminum disk.

2.1.3.4 Embedding Accelerometers - Attempt #4

The fourth attempt to mount the accelerometer proved to be the most successful. The mounting of the accelerometer was based upon the previous attempt, but the wire was drawn underneath the accelerometer into the tire and then out to the slip ring through a sealed hole in the sidewall so that the wiring would not come in contact with the pavement and was protected from the high strains near the surface. This adaptation can be seen in Figure 2-8. Two rotations of this signal at 20 miles per hour, shown in Figure 2-9, appeared to be the most accurate representation of the vibration at the surface of the tire.

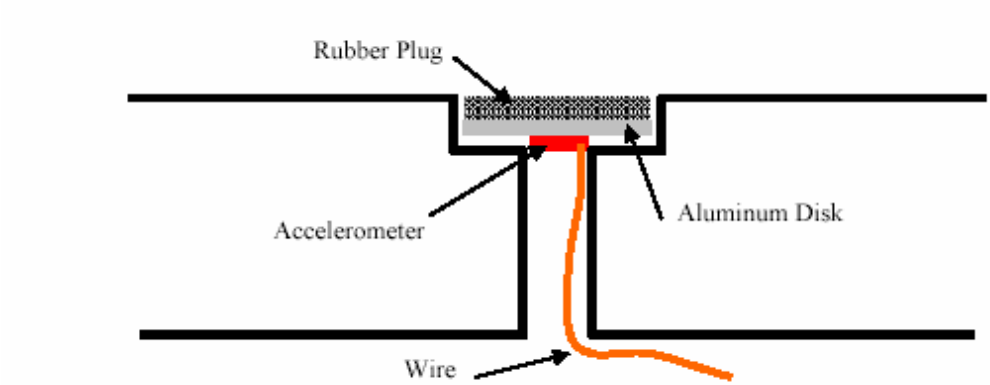

Figure **2-8**: Accelerometer mounting attempt #4: Accelerometer mounted on aluminum disk and wire drawn out through sidewall of tire.

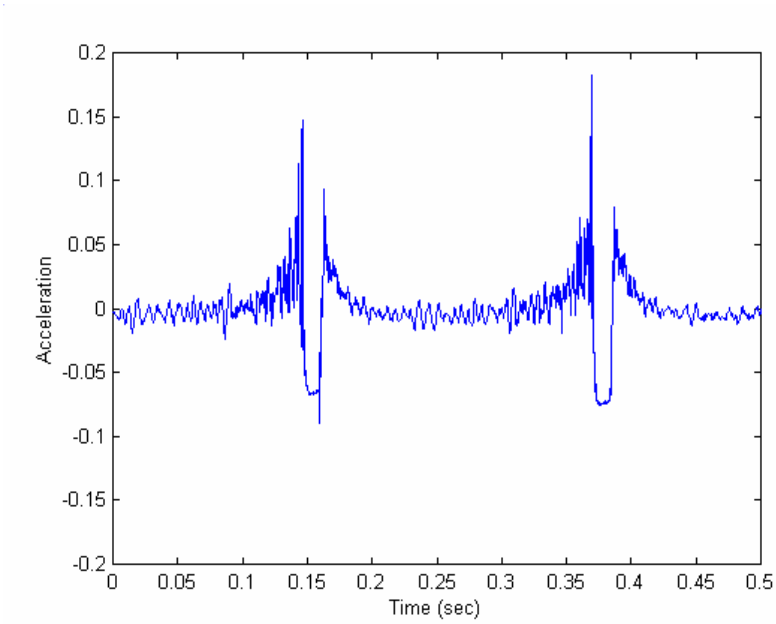

Figure **2-9**: Uncalibrated voltage output from DAT recorder for attempt #4 measured over two tire rotations.

2.2 Frequencies of Resonance

To provide data for verifying the analytic model to be used to predict the non-radiating portion of acceleration, the frequencies of resonance of the tire were measured. The blank tire was suspended with bungee cords and an accelerometer was mounted on the outer surface of the tire. The tire was then randomly excited with impacts around the tire. The accelerometer signal was recorded onto the DAT recorder and processed in Matlab. The resulting frequency spectrum was examined to find the peaks which corresponded to the resonance frequencies. More details on these measurements will be discussed in Chapter 3.

2.3 Tire Testing

The final stage of the experimental process was the data collection of the tire surface vibration under controlled conditions. On two separate occasions, measurements were conducted in the Goodyear test facility in Akron, Ohio. In the first set of measurements, two blank tires were used. The first tire had four radial accelerometers embedded in an array along the circumference of the tire. The second tire had accelerometers in three orientations: radial, tangential, and axial, which measured in the directions shown in Figure 2-10. In the second set of measurements, an array of eight radial accelerometers was embedded along the circumference of a blank tire. All of the accelerometers were embedded in the tread at a location approximately halfway between the center line and the edge of the tire, which was about 4 cm from the center of the tread band. Descriptions of the first three tests done are given in Table 2-1. Unfortunately,

many of the accelerometers were unable to survive the severe conditions they were exposed to during testing. In test 3, the tangential and axial accelerometers did not survive on the rough pavement. Many of the accelerometers failed during the second set of measurements made with the 8-accelerometer array before a sufficient amount of usable data could be obtained.

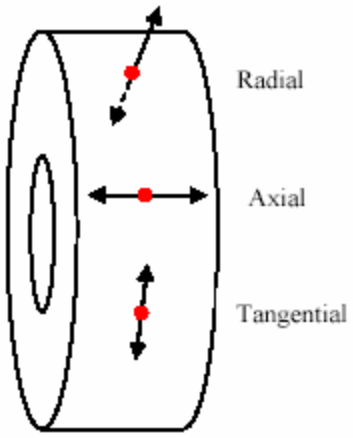

Figure **2-10**: Diagram of tire with accelerometers embedded in three orientations.

Table **2-1**: Tire/Pavement tests performed at Goodyear test facility.

Test	Tire	Accelerometers	Pavement	Speeds (mph)
1	Blank	4 Radial	Smooth	10, 20, 30, 40, 50
2	Blank	1 Radial, 1 Tangential, 1 Axial	Smooth	10, 20, 30, 40, 50
3	Blank	1 Radial, 1 Tangential, 1 Axial	Rough	10, 20, 30, 40, 50

The tires, mounted on the 16-inch wheel rims, were mounted on the road-wheel system as shown in Figure 2-11. The slip ring is also bolted onto the wheel and the cables connected to the accelerometers. The accelerometers were then connected to a

PCB Piezoelectronics, Inc. signal conditioner, model 483A, and the output connected to the TEAC RD-145T 16-channel DAT recorder. Three Brüel & Kjær microphones were arranged around the tire at distances of 10 feet in front of the tire, 10 feet from the sidewall, and 10 feet behind the trailing edge of the tire, all at heights of 4 feet. All measurements were recorded at a sample rate of 12 kHz.

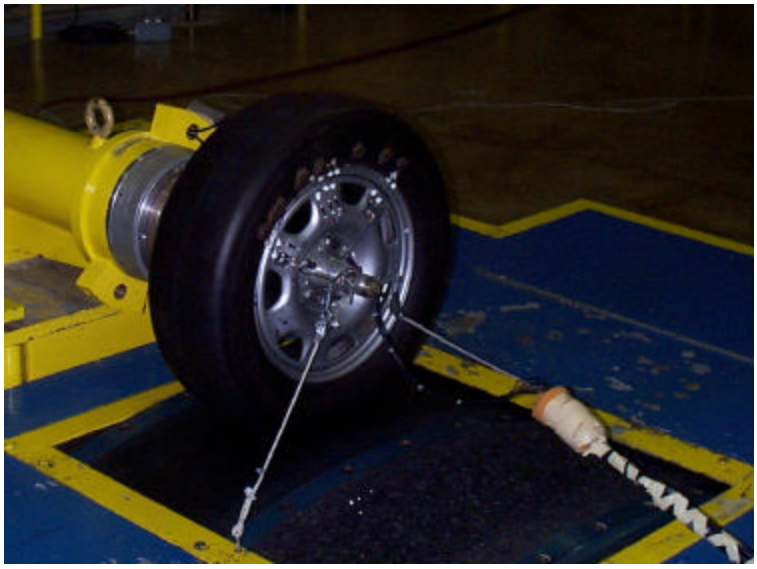

Figure **2-11**: Goodyear test setup with tire on road wheel.

The road wheel was a 10-foot diameter cylinder mounted beneath the floor of a semi-anechoic chamber. The wheel had two test pavements, smooth and rough, which are shown in Figure 2-12.

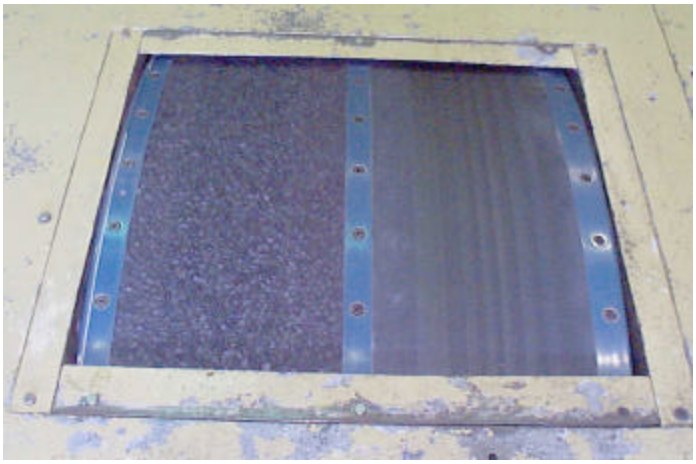

Figure **2-12**: Rough (left) and smooth (right) pavements on Goodyear road-wheel.

After everything was in place, the test tire was lowered onto the road wheel and set at a static load of approximately 800 pounds, similar to a typical load on one wheel of a passenger car. The lab technicians ran the tire at speeds of 10, 20, 30, 40, and 50 mph for periods of two minutes.

Once the recording equipment was returned to Penn State, the sets of data were downloaded from the DAT tapes and processed with Matlab. This data processing is also discussed further in Chapter 3.

Chapter 3

DATA PROCESSING

In order to better understand the mechanisms of tire/pavement interaction noise generation, it was necessary to measure the vibrations produced at the outer surface of the tread at the entrance and exit to the contact patch, where most of the radiation occurs. Measurements were made at the Goodyear test facility onto a 16-channel DAT recorder. The acceleration-versus-time signals were uploaded and processed using MATLAB version 5.3. Table 2-1 in the previous chapter displays the details of the three tests performed at Goodyear, including accelerometer orientations, speed, and pavement type.

3.1 Recorded Signal

Each rotation of the recorded radial acceleration signals generally appears with the same constant shape on which random vibrations are superimposed. The acceleration peaks sharply just as the accelerometer enters the contact patch, hits a minimum at the center of the contact patch, and drops dramatically as it leaves the pavement. The random vibrations increase while approaching the entrance and decrease after exiting the contact patch. A time trace of several rotations of the radial accelerometer signal recorded at 20 miles per hour on the smooth Goodyear surface is shown in Figure 3-1. It would be ideal to verify that the measured radial acceleration is accurate by comparing

the signals recorded by several accelerometers; however, only one accelerometer mounted in the radial direction survived at speeds of 10 mph and higher.

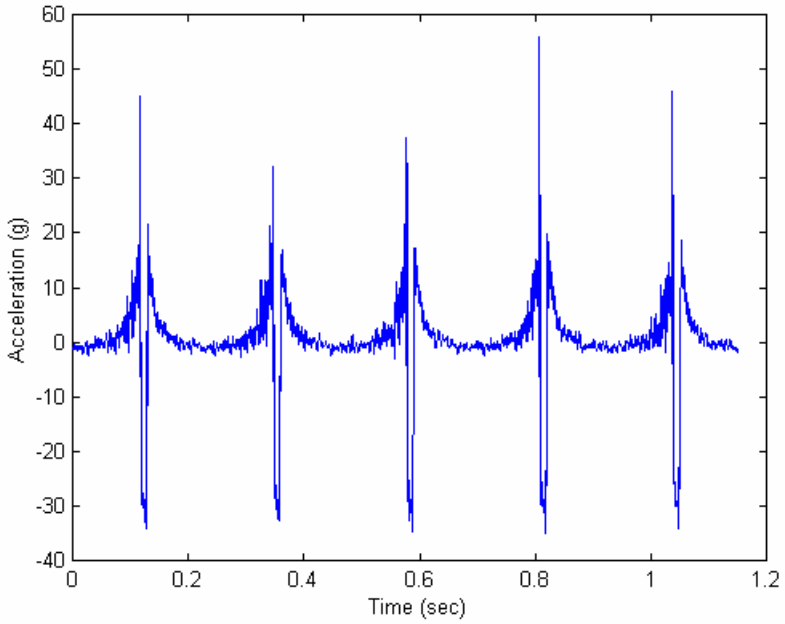

Figure **3-1**: Five rotations of radial acceleration at 20 mph on smooth pavement.

Figure 3-2 shows the recorded signal over one rotation of the tire and it is apparent that there is a distinct shape to the radial acceleration as it passes through the contact patch. The path through the contact patch is constant for each rotation and the acceleration that is produced by the deformation of the tire is not considered a radiating noise source. In order to analyze the vibrations that produce acoustic radiation more completely, this non-radiating component recorded by the embedded accelerometer needs to be removed.

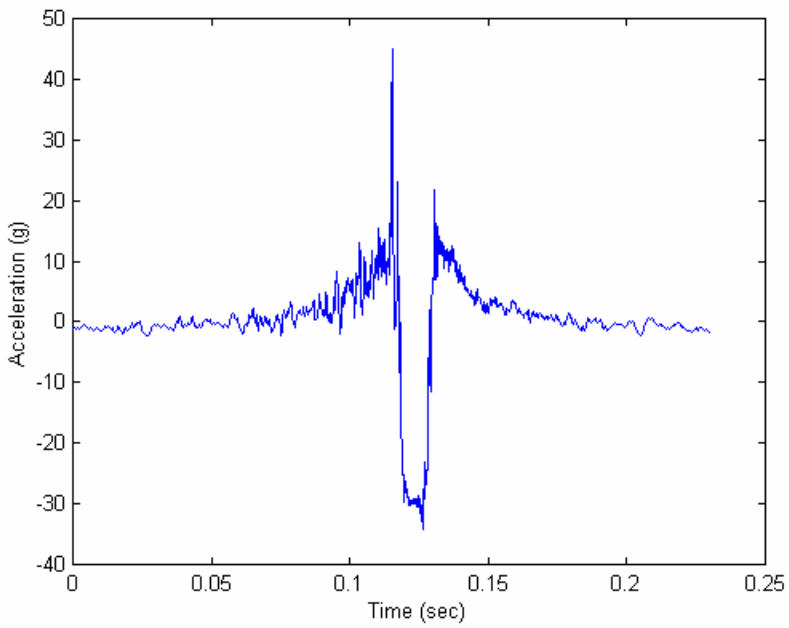

Figure **3-2**: One rotation of radial acceleration at 20 mph on smooth pavement.

3.2 Non-Radiating Component

To do a spectral analysis of the radiating component of the signal from the embedded accelerometer and accurately measure the noise-radiating vibrations, it is necessary to remove the non-radiating component. Two methods were tested to eliminate the non-radiating component. One method to remove the non-radiating component is to develop an analytic model and then subtract the non-radiating component, predicted by the model, from the recorded signal. The second is to take an average over several rotations of the recorded signal to approximate the non-radiating signal and subtract it from the signal recorded during one rotation. Alternatively, the area outside the contact

patch of the raw signal can be divided into small segments and then windowed to compute the frequency spectrum in several regions outside the contact patch.

3.2.1 Analytic Model

As mentioned previously in Chapter 1, Kropp [10] and Heckl [11] have developed methods of modeling the vibration of a tire surface. Equations 3.1 and 3.2 used by Kropp and Heckl are applied here to model the non-radiating component of the acceleration. These expressions for two-dimensional vibration are based upon Boehm's 'circular ring model'. It is assumed that the vibrations are constant across the width of the tire.

$$u'' + u' - d^2(u''' + u') + (n^2 - n_t^2)u = -\frac{q_t a^2}{ES} \qquad \textbf{3.1}$$

$$g^2(u'' + u) - (u' + u) - d^2(u'''' + u'') + (n^2 - n_a^2)u = -\frac{q_a a^2}{ES} \qquad \textbf{3.2}$$

In these expressions, u is the tangential displacement and u is the radial displacement and the derivatives with respect to the angle of rotation, f, are indicated by primes. The external forces per unit area are represented by q_t in the tangential direction and q_a in the radial direction. For this research, q_t corresponds to shear pressure and q_a represents normal pressure exerted on the tire by the pavement in the contact patch. The radius of the tire is a, E is the Young's modulus of the tire material, and S is the cross-sectional area of the tire. In Equations 3.1 and 3.2, dimensionless quantities were introduced, as given in Equations 3.3- 3.7, where r is the density, T_0 is the tension, and B is the bending stiffness of the tire material.

$$n^2 = \left(\frac{w}{w_0}\right)^2 = \frac{rSa^2w^2}{ES} \qquad \textbf{3.3}$$

$$n_t^2 = \left(\frac{w_t}{w_0}\right)^2 = \frac{k_t a^2}{ES} \qquad \textbf{3.4}$$

$$n_a^2 = \left(\frac{w_a}{w_0}\right)^2 = \frac{k_a a^2}{ES} \qquad \textbf{3.5}$$

$$g^2 = \left(\frac{c_s}{c_L}\right)^2 = \frac{T_0}{ES} \qquad \textbf{3.6}$$

$$d^2 = \frac{Ba^2}{ESa^4} \qquad \textbf{3.7}$$

The value represented by c_s is the wave speed if the tire is considered a string under tension T_0. The bending stiffness of the tire, B, is related to the thickness of the tread band, h, and Poisson's ratio, m, in Equation 3.8. The elastic properties of the sidewalls and the air pressure in the tires determine the radial and tangential bedding coefficients, k_a and k_t, and the resonance frequencies of a system with radial and tangential stiffness are w_a and w_t. The quantities were normalized by the ring frequency, w_0, defined in Equation 3.9, where c_L is the longitudinal wave speed in the ring material and is computed from Equation 3.10. [10]

$$B = \frac{Eh^3}{12(1-m^2)} \qquad \textbf{3.8}$$

$$w_0 = \frac{c_L}{a} \qquad \textbf{3.9}$$

$$c_L = \sqrt{\frac{E}{r}} \qquad \textbf{3.10}$$

3.2.1.1 Verification of Analytic Model

In order to validate the model to be used for the non-radiating portion of the acceleration signal, the frequencies of resonance predicted by the model are compared to measured frequencies of resonance of the tire.

The measured resonance frequencies were determined by mounting an accelerometer on the surface of the tire tread while the tire was impacted with a hammer in various locations around the tire. The vibration response of the accelerometer was recorded with the DAT recorder. The frequency spectrum of each impact response was examined and the frequencies at which there are peaks in the spectrum were recorded. The first four resonance frequencies inferred from several impact response functions were averaged and are given in the first column of Table 3-1.

Table **3-1**: Comparison of measured and theoretical resonance frequencies.

Resonance Frequencies (Hz)		**% Difference**
Measured	**Theoretical**	
93.3	78.8	18%
113.1	108.6	4%
132.3	133.5	1%
155.1	159.5	3%

To find the theoretical frequencies of resonance, *w*, the shear and normal pressures, q_t and q_a, are set equal to zero in Equations 3.1 and 3.2. The radial and tangential displacements, *u* and *u*, are assumed to be free waves of the form e^{inf}. [10] The equations are then solved for $\nu^2 = (\omega/\omega_0)^2$ from the quadratic equation given in Equation 3.11 to determine *w*.

$$\begin{aligned} & n^4 + n^2\left[g^2 - 1 - (n_a^2 + n_t^2) - n^2 d^2 + n^2(d^2 - g^2 - 1)\right] + n^6 d^2 + \ldots \\ & \ldots + n^4\left[g^2 + d^2(n_t^2 - 2)\right] + n^2\left[n_t^2(g^2 - d^2) - g^2 + n_a^2 - d^2\right] + \ldots \\ & \ldots + n_t^2(1 - g^2 + n_a^2) = 0 \end{aligned} \qquad \textbf{3.11}$$

The theoretical resonance frequencies were then computed with the material parameters for a smooth tire which were used by Kropp [10] and estimated from measurements of the tire used for this research. The Young's modulus, *E*, and the tension, T_0, were then modified slightly until the resulting frequencies most nearly matched those obtained empirically. The material properties used are given in Table 3-2. The final theoretical frequencies of resonance are displayed in the second column of Table 3-1 and the percent differences between the theoretical values and measured frequencies of resonance are given in the third column. Because there was a reasonable agreement between the frequencies of resonance, the model was used to predict the non-radiating component of the acceleration.

Table **3-2**: Material parameters of a smooth tire used for calculation of resonance frequencies.

Variable	Description	Value
a	Radius of tire	0.33 m
h	Thickness of tread band	0.0127 m
r	Density of tire material	1000 kg/m^3
S	Cross-sectional area of tire belt	2.2×10^{-3} m^2
k_a	Radial bedding coefficient	9.7×10^5 N/m^2
k_t	Tangential bedding coefficient	1.2×10^5 N/m^2
m	Poisson's ratio	0.45
B	Bending stiffness of tire belt	77 Nm
E	Young's modulus	3.6×10^8 N/m^2
T_0	Tension	9.5×10^3 N/m

3.2.1.2 Comparison of Model to Recorded Signal

After verifying the equations used to find the model for the non-radiating portion of the signal, the model was then solved to find the radial and tangential displacement. Using sample data provided by Goodyear, the shear and normal pressure experienced by the tire through the contact patch was determined and is plotted in Figure 3-3. The limits on the shear and normal pressure due to the contact patch, $s(f)$ and $p(f)$, are defined in Equation 3.12, where the size of the contact patch is represented by the angle f_0. Figure 3-4 shows how f_0 is identified.

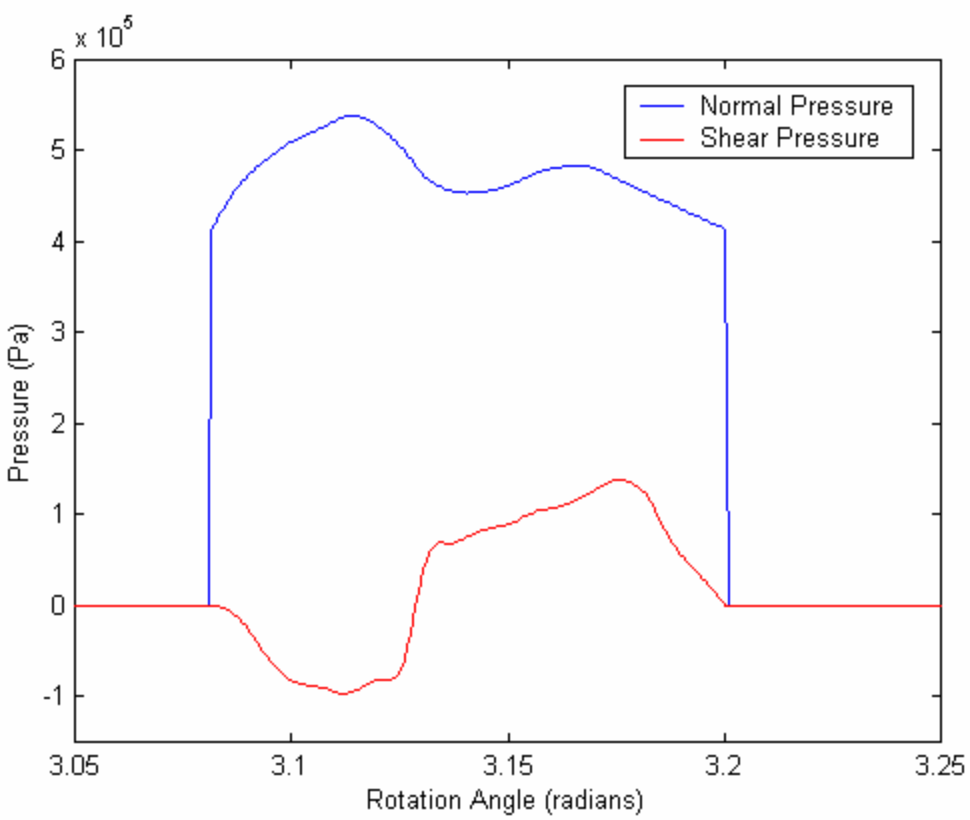

Figure **3-3**: Shear and normal pressure experienced by the surface of the tire as it rolls through the contact patch.

$$p(f) = \begin{cases} P(f) & \text{for } p - f_0 < f < p + f_0 \\ 0 & \text{for } p - f_0 > f > p + f_0 \end{cases}$$
$$s(f) = \begin{cases} S(f) & \text{for } p - f_0 < f < p + f_0 \\ 0 & \text{for } p - f_0 > f > p + f_0 \end{cases} \qquad \textbf{3.12}$$

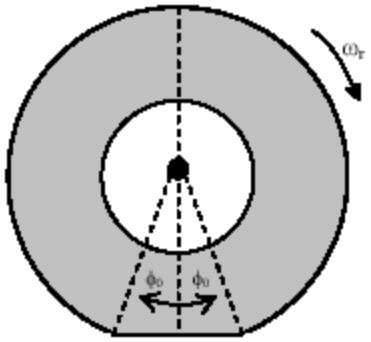

Figure **3-4**: Diagram of rolling tire identifying rotation speed and contact patch size.

The tangential and radial displacements, u and u, are each expressed as a Fourier series. The resulting solutions for u and u are given in Equations 3.13 and 3.14. The values A_n, B_n, C_n, and D_n, are given in 3.15 and a_{11}, a_{22}, c_{11}, and c_{22} are given in 3.16.

$$u = -\frac{a^2}{ES}\sum_n \left\{ \frac{[B_n c_{11} + C_n c_{22}]\cos(nw_r t) + [D_n c_{22} - A_n c_{11}]\sin(nw_r t)}{a_{11}c_{22} + a_{22}c_{11}} \right\} \qquad \textbf{3.13}$$

$$u = -\frac{a^2}{ES}\sum_n \left\{ \frac{[A_n a_{11} + D_n a_{22}]\cos(nw_r t) + [B_n a_{11} - C_n a_{22}]\sin(nw_r t)}{a_{11}c_{22} + a_{22}c_{11}} \right\} \qquad \textbf{3.14}$$

$$\begin{aligned} A_n &= \frac{2}{T}\int_0^T p(t)\cos(nw_r t)dt \\ B_n &= \frac{2}{T}\int_0^T p(t)\sin(nw_r t)dt \\ C_n &= \frac{2}{T}\int_0^T s(t)\cos(nw_r t)dt \\ D_n &= \frac{2}{T}\int_0^T s(t)\sin(nw_r t)dt \end{aligned} \qquad \textbf{3.15}$$

$$
\begin{aligned}
a_{11} &= -n^2 + n^2 - n_t^2 \\
c_{11} &= -n - d^2 n^3 + d^2 n \\
a_{22} &= n \\
c_{22} &= -g^2 n^2 + g^2 - 1 - d^2 n^4 + d^2 n^2 + n^2 - n_a^2
\end{aligned}
\qquad \textbf{3.16}
$$

Examples of one rotation of the tangential and radial displacements at 20 mph with the contact angle f_0 set at 3.4 degrees are plotted in Figure 3-5. The second derivatives of the equations yield the acceleration, which is shown in Figure 3-6.

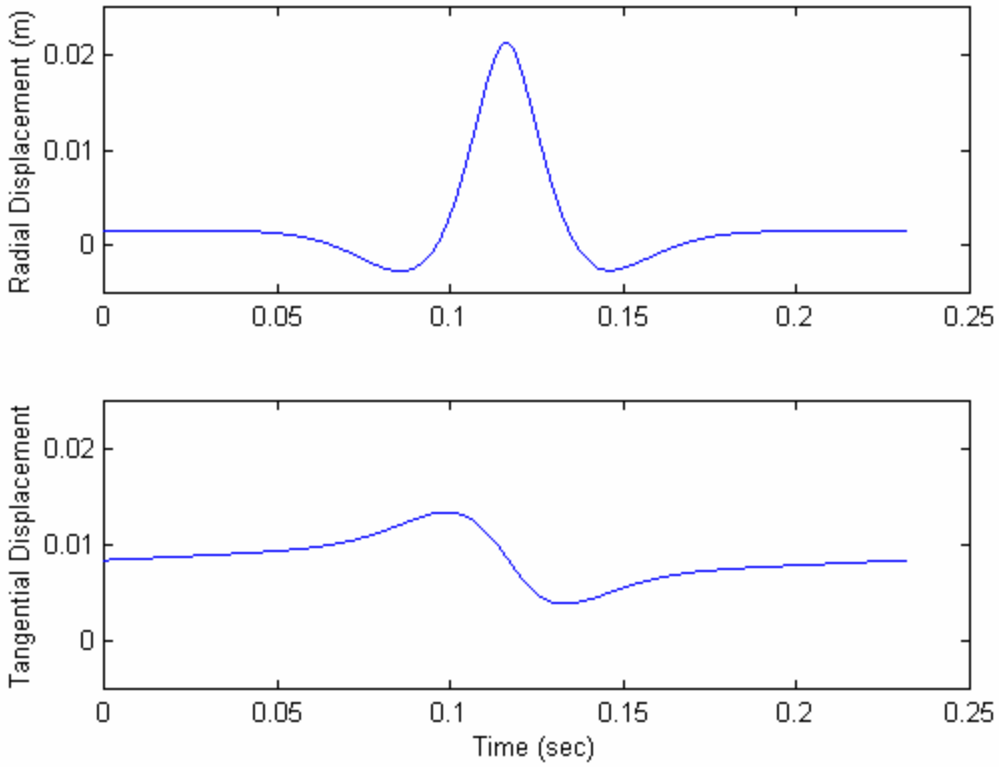

Figure **3-5**: Analytic model of one rotation of tangential and radial displacement.

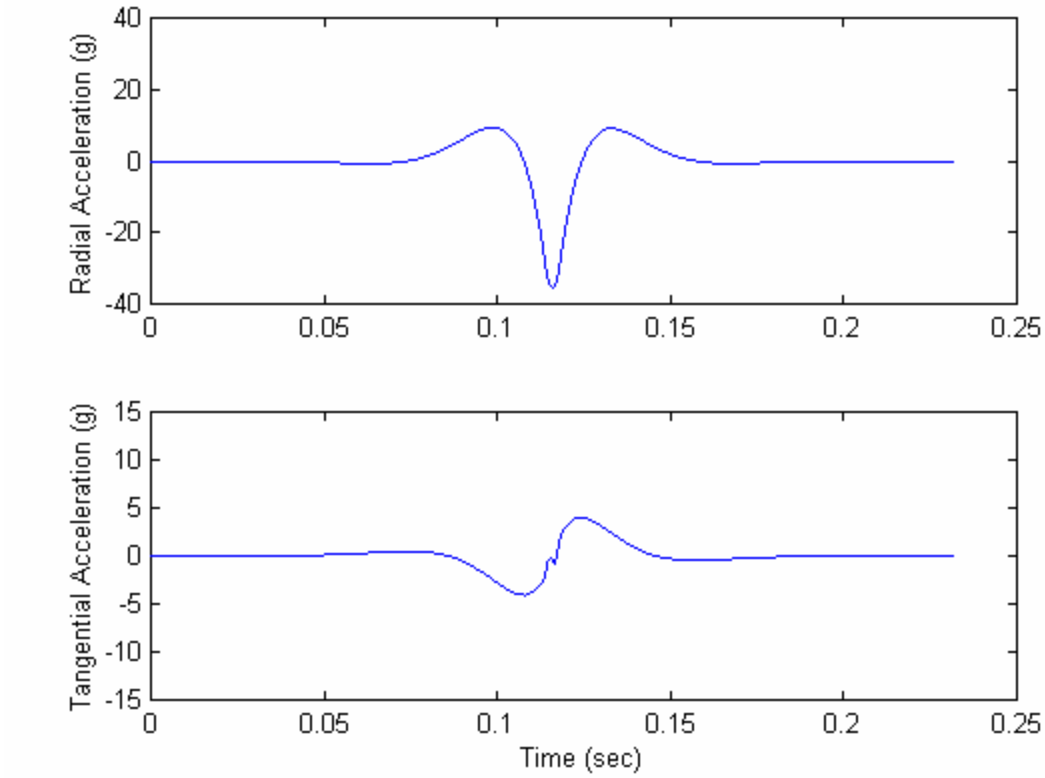

Figure **3-6**: Analytic model of one rotation of tangential and radial acceleration.

Figure 3-7 shows a comparison of one rotation of the measured radial and tangential acceleration with the corresponding analytic models at 20 mph. The radial model follows the shape of the measured signal and can be used to remove the non-radiating component. However, the tangential acceleration model does not match the measured data and will not be used to remove the non-radiating component of the measured tangential acceleration. The analytic model is only 2-dimensional and the predicted tangential acceleration may not be accurately predicting the non-radiating component of the measured tangential acceleration. It is also possible that the measured

tangential acceleration may contain some errors and might need to be verified with measurements made with a different accelerometer.

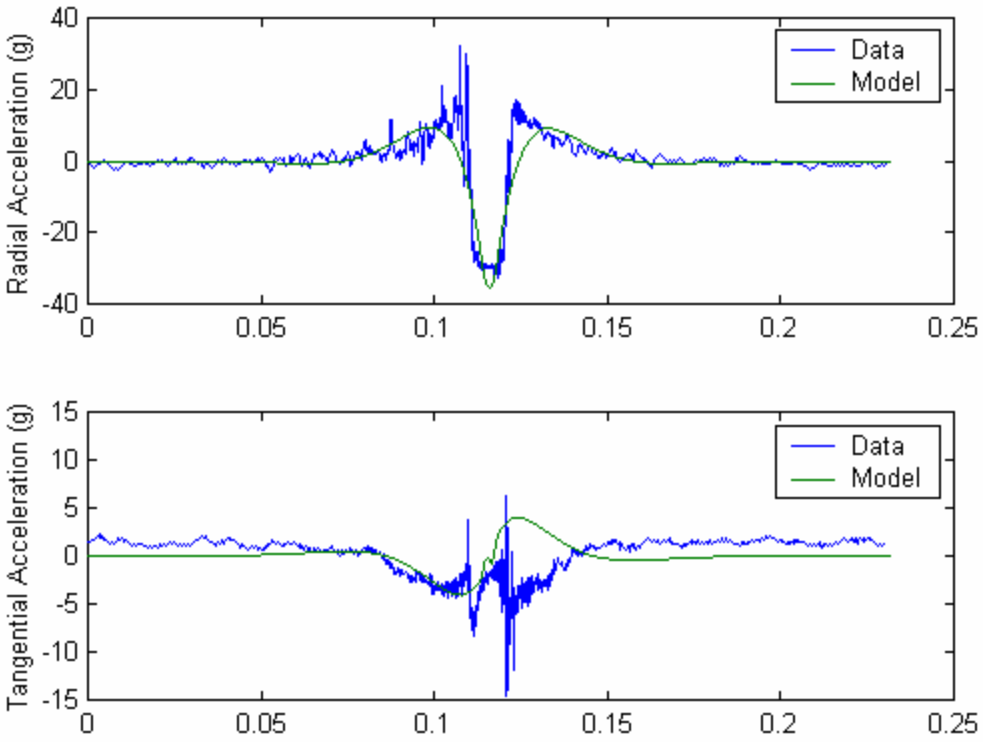

Figure **3-7**: Comparison of theoretical model to measured radial acceleration.

3.2.2 Average of Several Rotations

A second method of removing the non-radiating part of the accelerometer signal is to compute the average of the recorded signal over several periods of rotation to approximate the non-radiating portion of the acceleration. The computed average is then subtracted from the recorded signal. Because the deformation is constant and the

vibrations are random, it is assumed that if the average is subtracted from a signal, the remaining time trace will be the random, and therefore, the radiating component.

Averages of the measured signal were taken over twenty rotations of a signal at a constant speed. The averaged signal was then subtracted from the signal recorded during one rotation so that only the radiating component remained. Fourier transforms were then taken of the resulting signal to determine the frequency spectrum.

3.2.3 Segmenting a Rotation

Another approach to the analysis of the radiating component of the recorded signal without finding the non-radiating component is to segment the time trace. The entrance and exit of the contact patch were each divided into six segments, as shown for radial acceleration in Figure 3-8. Each segment was windowed using a Hanning window and a Fourier transform was performed to determine the frequency spectrum within each segment.

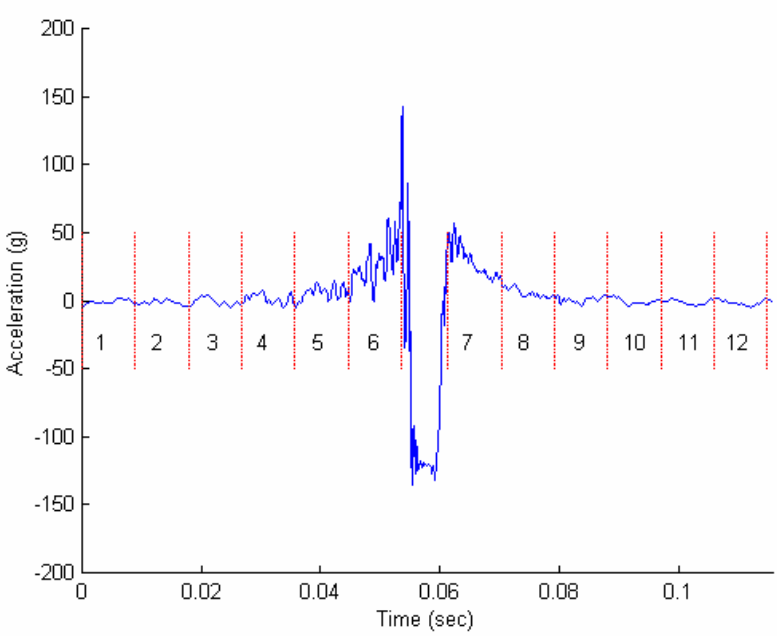

Figure **3-8**: One rotation of radial acceleration with segmented entrance and exit to contact patch

Chapter 4

RESULTS

Accelerometers were mounted on blank tires in three orientations: radial, tangential, and axial. The measurements were made on smooth and rough pavements at speeds of 10, 20, 30, 40, and 50 miles per hour. The acceleration-versus-time traces of each data set were examined and invalid data removed before data reduction was performed. From these time traces, the frequency spectra of the radiating components of the vibrations were determined using the methods outlined in Chapter 3. First, the entrance and exit to the contact patch were divided into segments for analysis. Second, the non-radiating component was estimated using two techniques: by calculating the average over several rotations and by predicting the non-radiating component using an analytic model. The estimated non-radiating component was then subtracted from the recorded signal. Several examples of these procedures are presented and discussed in this chapter and the remaining figures are found in Appendix A.

4.1 Single Rotation Time-Traces

4.1.1 Various Speeds

Plots of the radial acceleration versus time measured over one rotation of the blank tire on smooth pavement are given in Figure 4-1 at speeds varying from 10 mph to 50 mph. As the speed increases, the amplitudes of the measured acceleration also

increase. A plot of the average minimum acceleration levels recorded versus speed is shown in Figure 4-2 and demonstrates that the acceleration is proportional to the speed squared. The distinct shape of each of the acceleration curves is due to the movement of the accelerometer through the contact patch when it hits the pavement where a sudden change in acceleration is produced. Because this shape is consistent through each rotation, it is not considered a source of radiated noise. Radiation is produced by the random vibrations seen near the entrance and exit to the contact patch or where the acceleration initially slopes upward and finally slopes downward. These vibrations will be analyzed later in this chapter.

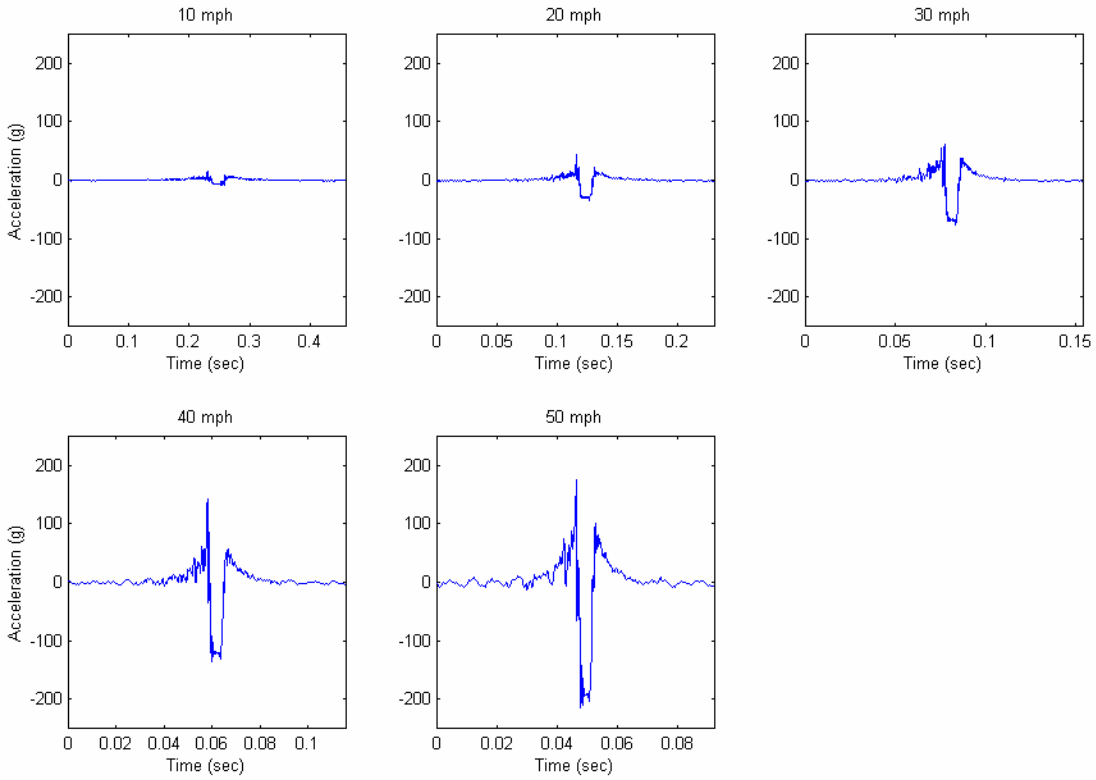

Figure **4-1**: One rotation of radial acceleration on smooth pavement at various speeds.

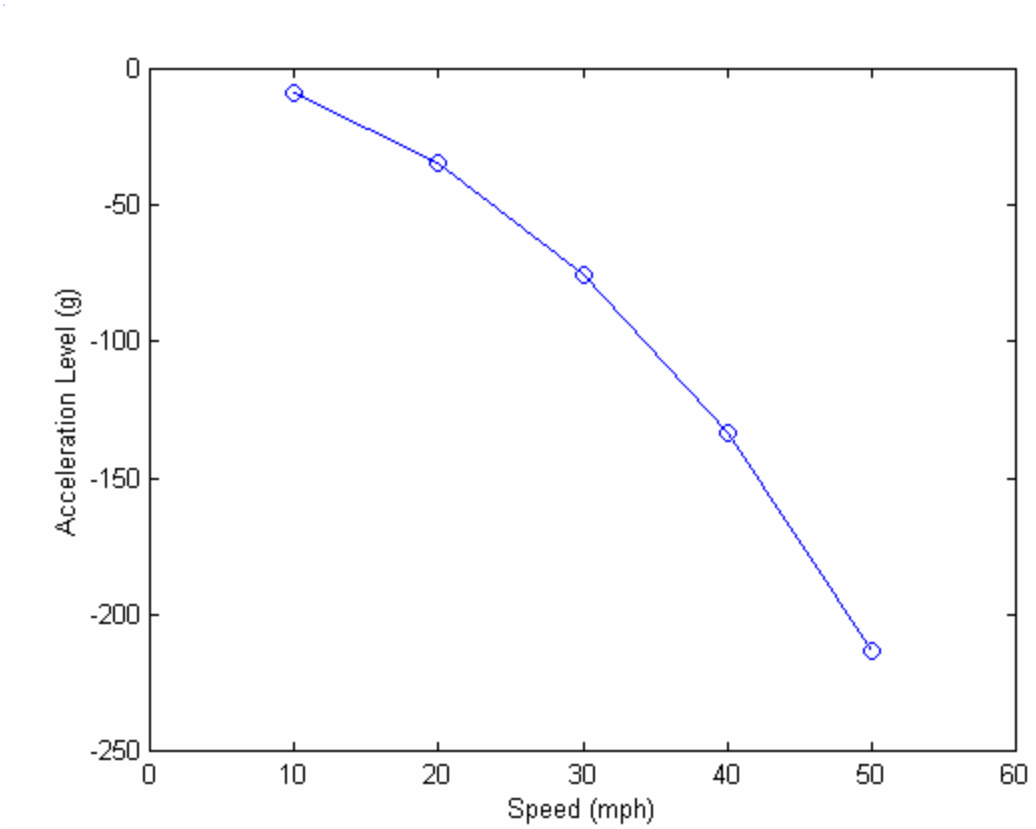

Figure **4-2**: Average minimum acceleration levels versus speed.

4.1.2 Smooth and Rough Pavements

The acceleration the surface of a tire experienced during rotation was measured on two pavement types. Figure 4-3 compares the radial acceleration on smooth and rough pavement at 20 mph. From this, it can be observed that the acceleration levels increase significantly in all locations with the tire rolling on the rough pavement.

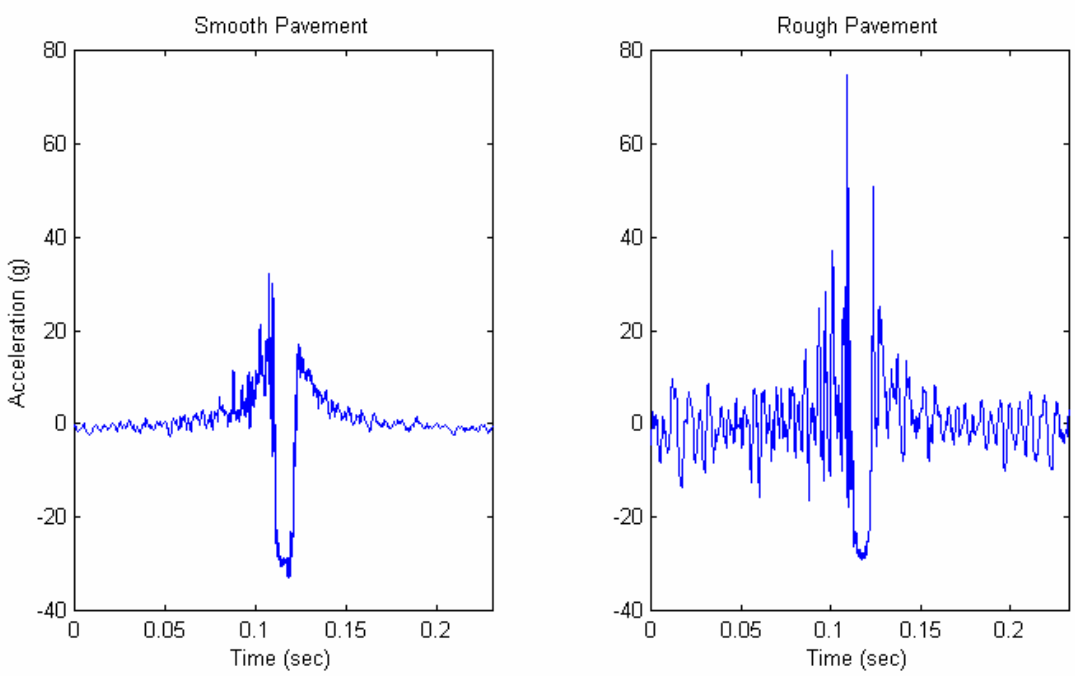

Figure **4-3**: One rotation of radial acceleration at 20 mph on smooth and rough pavement.

4.1.3 Radial, Tangential, and Axial Acceleration

The acceleration was also measured with the accelerometer placed in three different orientations. The radial, tangential, and axial acceleration on smooth pavement at 40 mph is shown in Figure 4-4. From this it is clear that the radial acceleration has the highest levels of acceleration and is therefore the direction of acceleration that will be studied most.

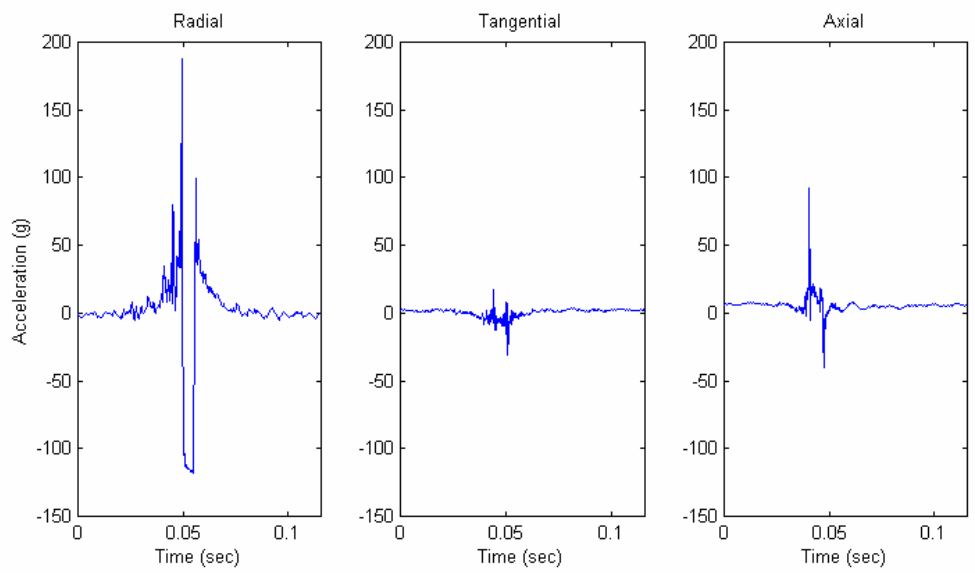

Figure **4-4**: Radial, tangential, and axial acceleration on smooth pavement at 40 mph.

4.2 Analysis of Results

To better understand the vibrations measured with the embedded accelerometers, it is important to analyze the frequency spectra using the data processing methods outlined in Chapter 3. First, the measurements are analyzed in segments around the contact patch. Then, the whole rotation is analyzed after the non-radiating component is subtracted using two different techniques.

4.2.1 Segment One Rotation

The entrance and exit to the contact patch of one rotation of the measured acceleration was divided into twelve segments that were analyzed separately The portion

of the signal measured through the contact patch was omitted for this analysis. This was done to avoid the need to estimate and subtract the non-radiating component from the measured signal as well as to analyze the vibrations in several discrete locations leading up to and away from the contact patch.

4.2.1.1 Smooth Pavement, Radial Acceleration

The entrance and exit to the contact patch of the time trace of the radial acceleration on smooth pavement at 40 mph were each divided into six segments, as shown in Figure 4-5.

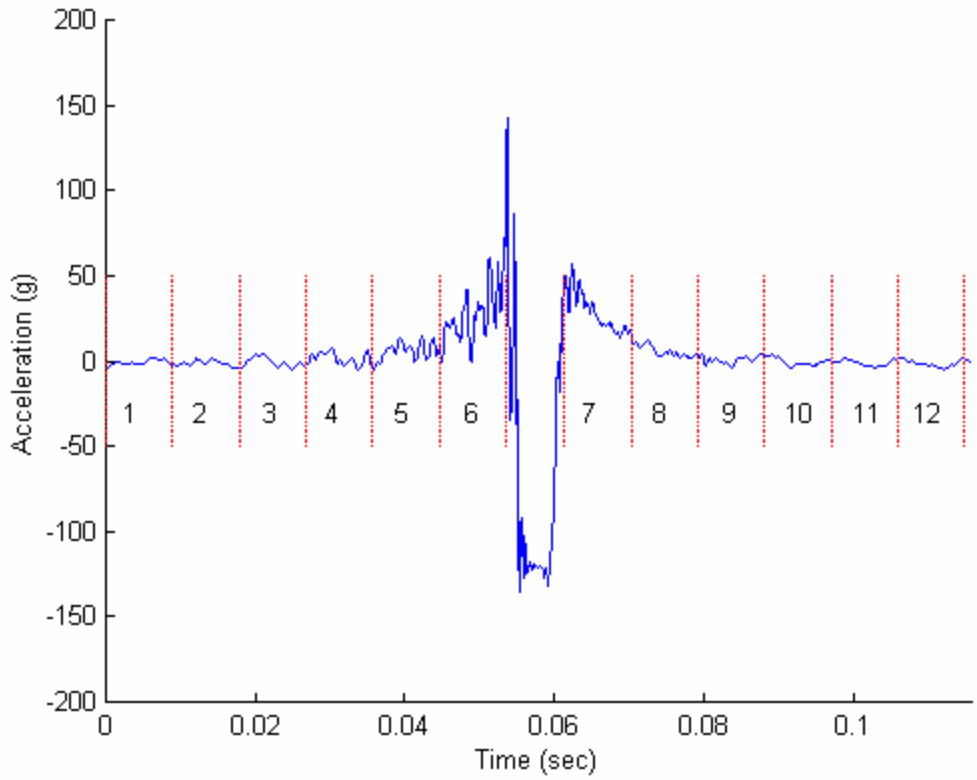

Figure **4-5**: Segmented entrance and exit to contact patch of one rotation of radial acceleration measured on smooth pavement at 40 mph.

Each segment in Figure 4-5 was windowed and the frequency spectrum was computed over a single segment. The spectra of the six segments in the entrance of the contact patch are shown in Figure 4-6. Similarly, the spectra of the segments in the exit of the contact patch are pictured in Figure 4-7. It is evident that the vibrations increase in level as the accelerometer approaches the contact patch and decrease as it leaves the contact patch.

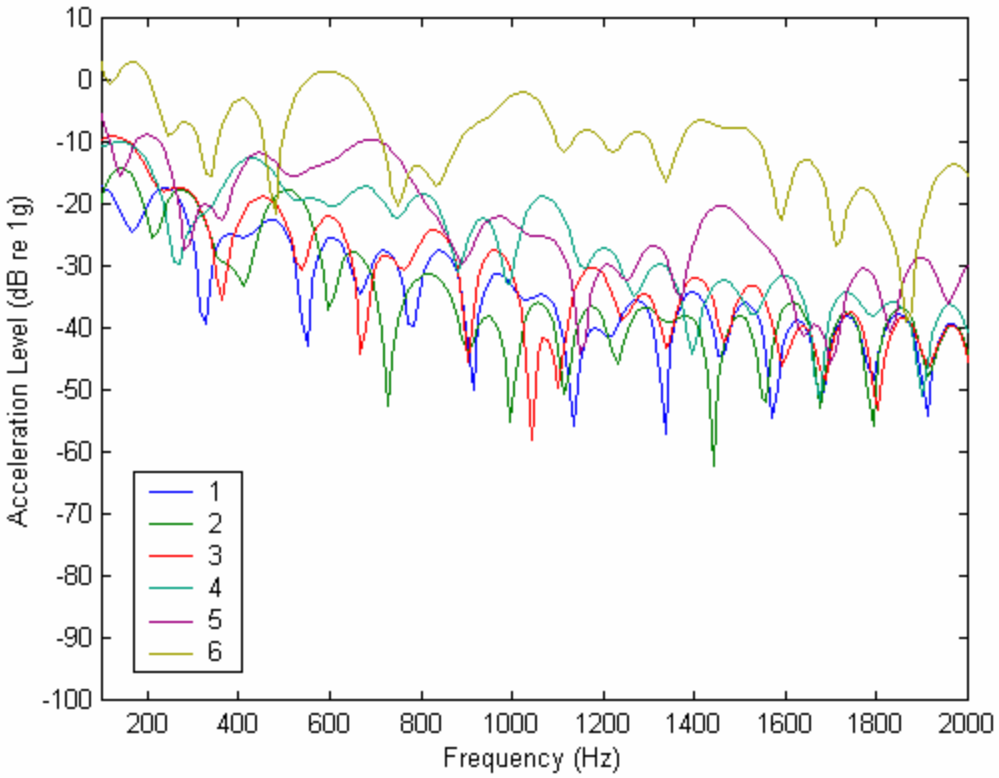

Figure **4-6**: Vibration spectra of segments in entrance to contact patch measured in the radial direction on smooth pavement at 40 mph. The frequency resolution is 6 Hz.

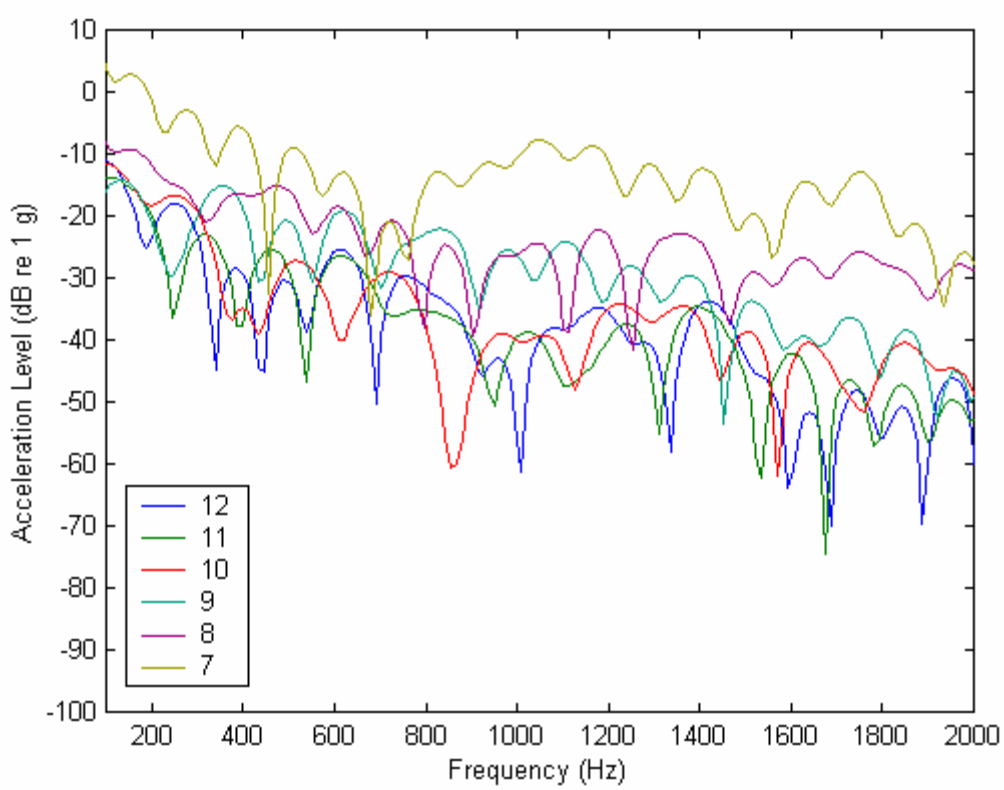

Figure **4-7**: Vibration spectra of segments in exit to contact patch measured in the radial direction on smooth pavement at 40 mph. The frequency resolution is 6 Hz.

The resulting vibration spectra calculated over each of the segments in the rotation may be improved by averaging the spectra calculated over the same segments taken from several rotations. This may improve the accuracy of the acceleration levels measured in each segment by taking a larger statistical sampling.

A comparison of the entrance and exit to the contact patch, segments 6 and 7, is shown in Figure 4-8. This shows that the vibration levels are higher at the entrance to the contact patch than the levels at the exit to the contact patch. This confirms the nearfield acoustic holography research localizing much of the radiation from a blank tire on

smooth pavement to the leading edge, although analysis of the radiation at the sidewall is neglected in this research.

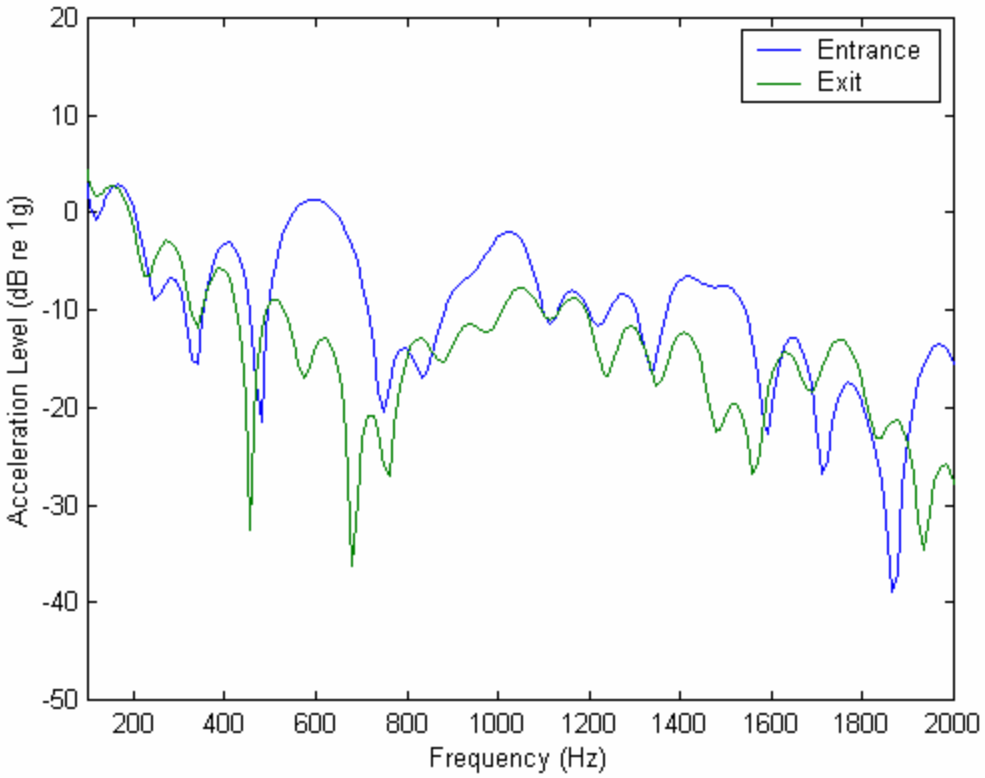

Figure **4-8**: Vibration levels at entrance and exit to the contact patch measured in the radial direction on smooth pavement at 40 mph. The frequency resolution is 6 Hz.

4.2.1.2 Rough Pavement, Radial Acceleration

One period of rotation of the radial acceleration on rough pavement at 40 mph was also divided into segments and is shown in Figure 4-9. The frequency spectra for the entrance and exit to the contact patch are given in Figures 4-10 and 4-11. Similar to the measurements made on smooth pavement, the vibration levels increase as the accelerometer moves closer to the contact patch. However, the exit to the contact patch

exhibits higher vibration levels in segment 7, but segments 8 - 12 all exhibit lower levels of vibration.

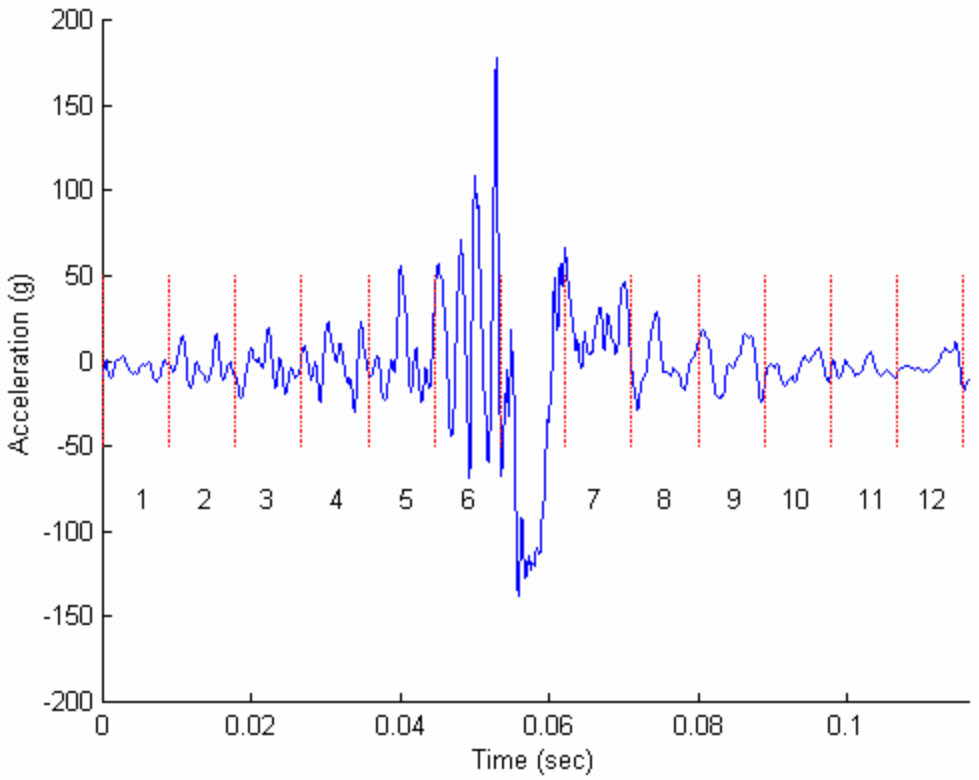

Figure **4-9**: Segmented entrance and exit to contact patch of one rotation of radial acceleration measured on rough pavement at 40 mph.

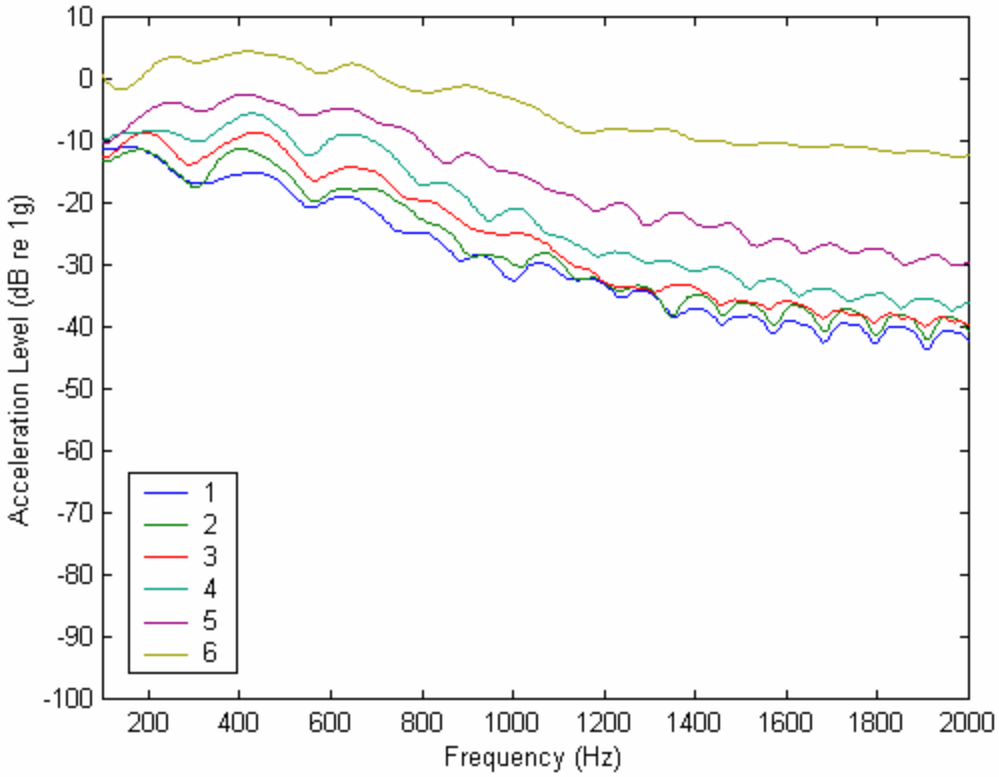

Figure **4-10**: Vibration spectra of segments in entrance to contact patch measured in the radial direction on rough pavement at 40 mph. The frequency resolution is 6 Hz.

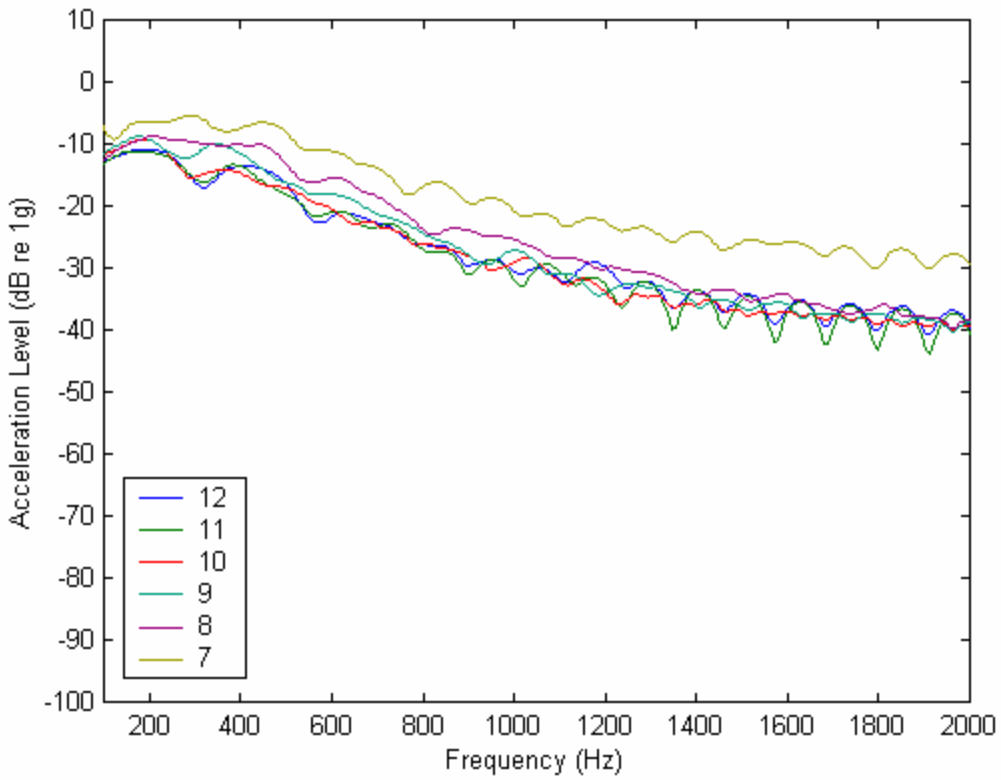

Figure **4-11**: Vibration spectra of segments in exit to contact patch measured in the radial direction on rough pavement at 40 mph. The frequency resolution is 6 Hz.

The frequency spectra measured in segments 6 and 7, the entrance and exit to the contact patch, of the radial acceleration measured on rough pavement at 40 mph is shown in Figure 4-12. As was seen for smooth pavement, the vibration levels are higher in the entrance to the contact patch than the levels in the exit to the contact patch.

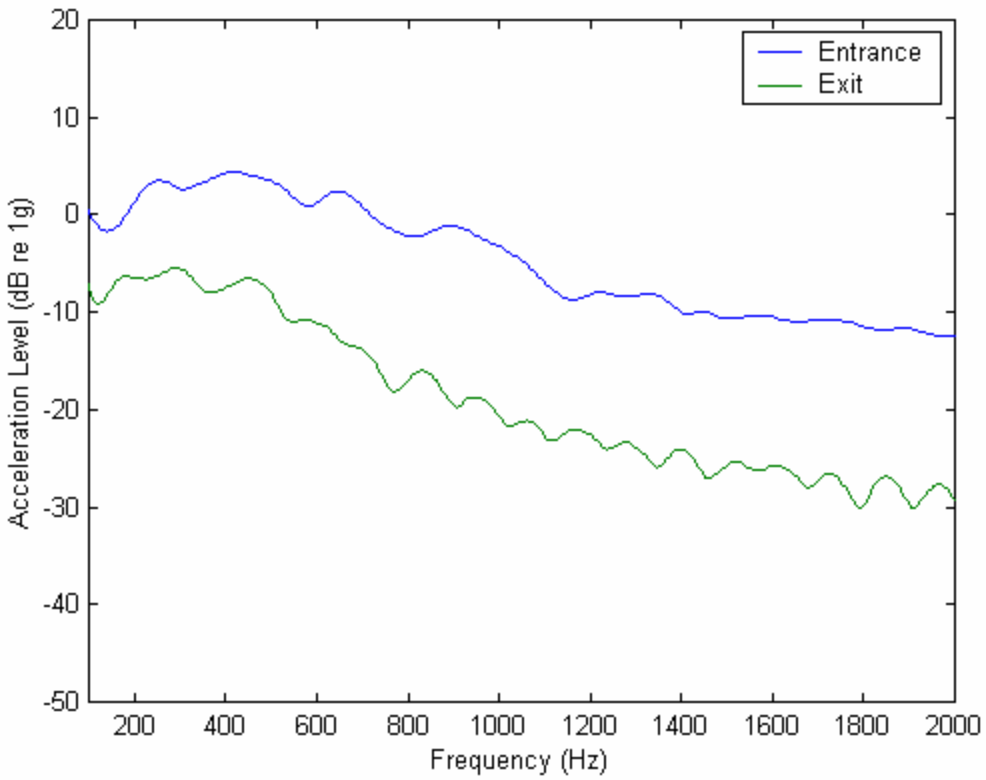

Figure **4-12**: Vibration levels at entrance and exit to the contact patch measured in the radial direction on rough pavement at 40 mph. The frequency resolution is 6 Hz.

4.2.1.3 Smooth Pavement, Tangential Acceleration

One period of the tangential acceleration measured on smooth pavement at 40 mph was segmented as shown in Figure 4-13. The frequency spectra for the entrance and exit to the contact patch are shown in Figures 4-14 and 4-15. From these plots it can be seen that the vibration levels are only increased significantly in the sixth and seventh segments, which are the segments nearest to the contact patch. In the frequency spectra of the segments that are further from the contact patch, noticeable 'bumps' appear and are due to the windowing of the segments where the levels are low.

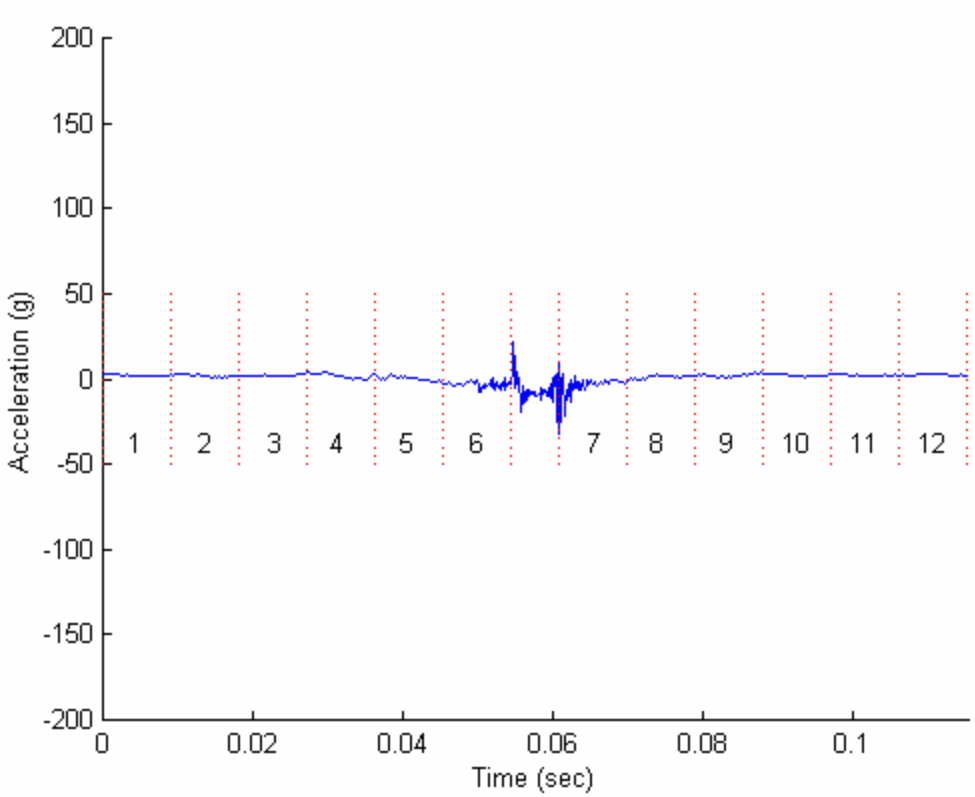

Figure **4-13**: Segmented entrance and exit to contact patch of one rotation of tangential acceleration measured on smooth pavement at 40 mph

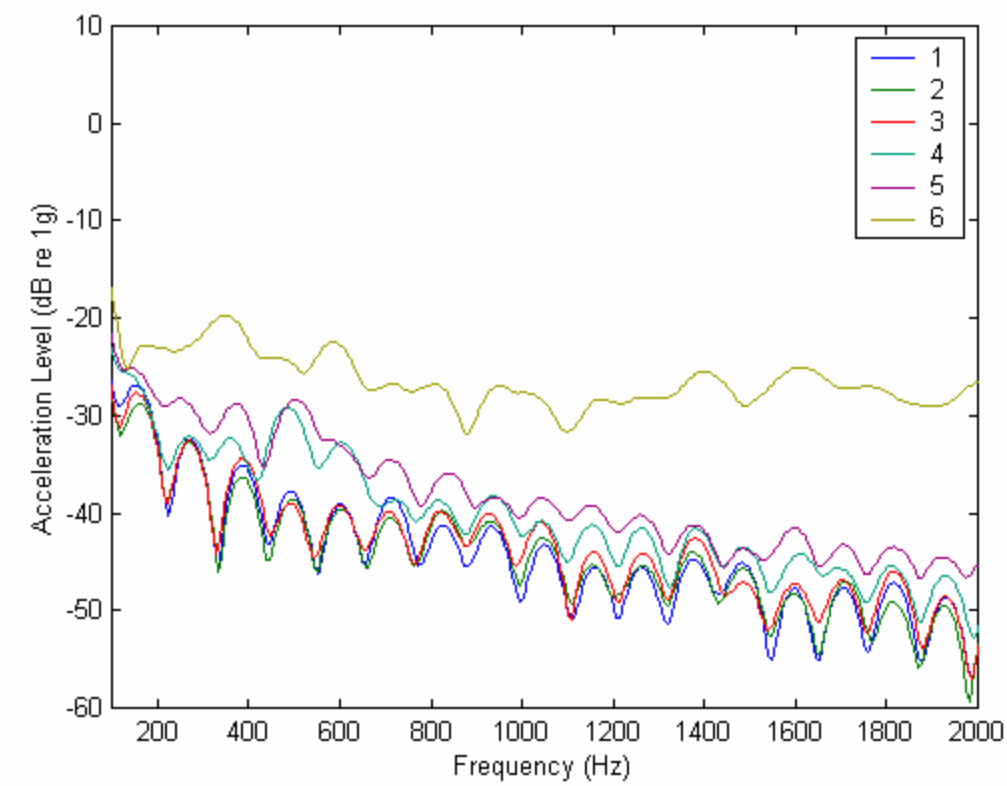

Figure **4-14**: Vibration spectra of segments in entrance to contact patch measured in the tangential direction on smooth pavement at 40 mph. The frequency resolution is 6 Hz.

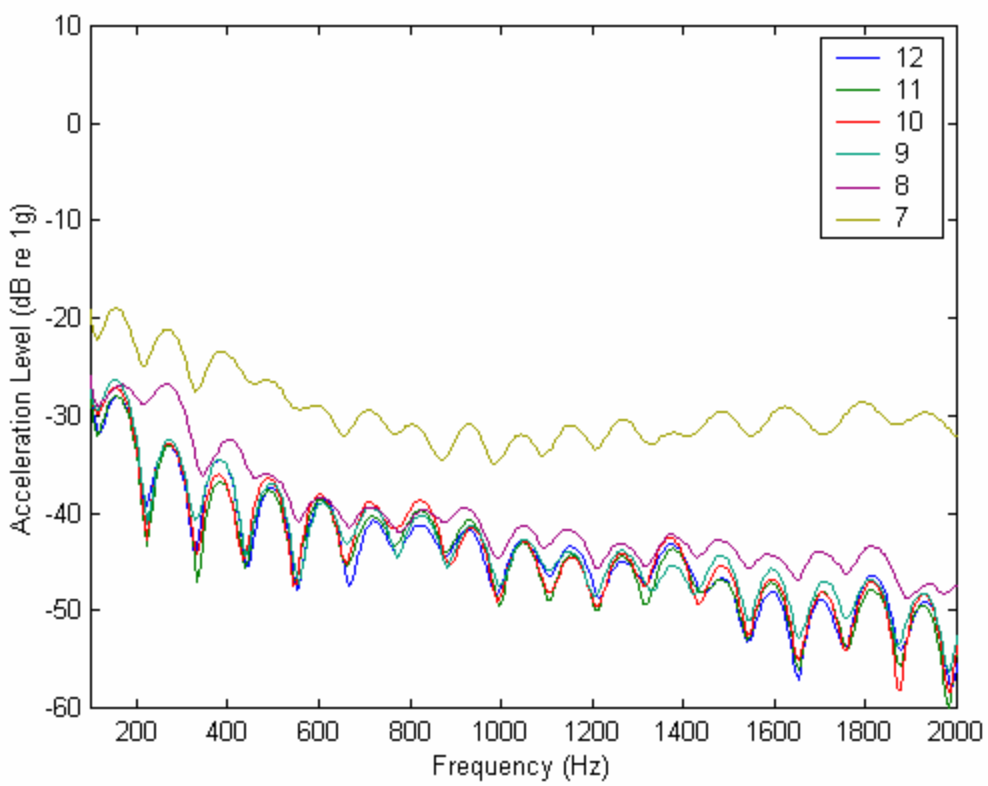

Figure **4-15**: Vibration spectra of segments in exit to contact patch measured in the tangential direction on smooth pavement at 40 mph. The frequency resolution is 6 Hz.

4.2.1.4 Smooth Pavement, Axial Acceleration

Figure 4-16 shows the divided entrance and exit to the contact patch for the axial acceleration on smooth pavement at 40 mph. The spectra for the entrance and exit segments are given in Figure 4-17 and Figure 4-18. In Figure 4-17, the vibrations are significantly higher only in segment six. Segments one through five all have similar low levels of acceleration when compared to the levels of segment six. In segment seven of Figure 4-18**,** the levels of vibration are higher only at the frequencies above 1000 Hz. levels seen in the other five segments that are farther from the contact patch.

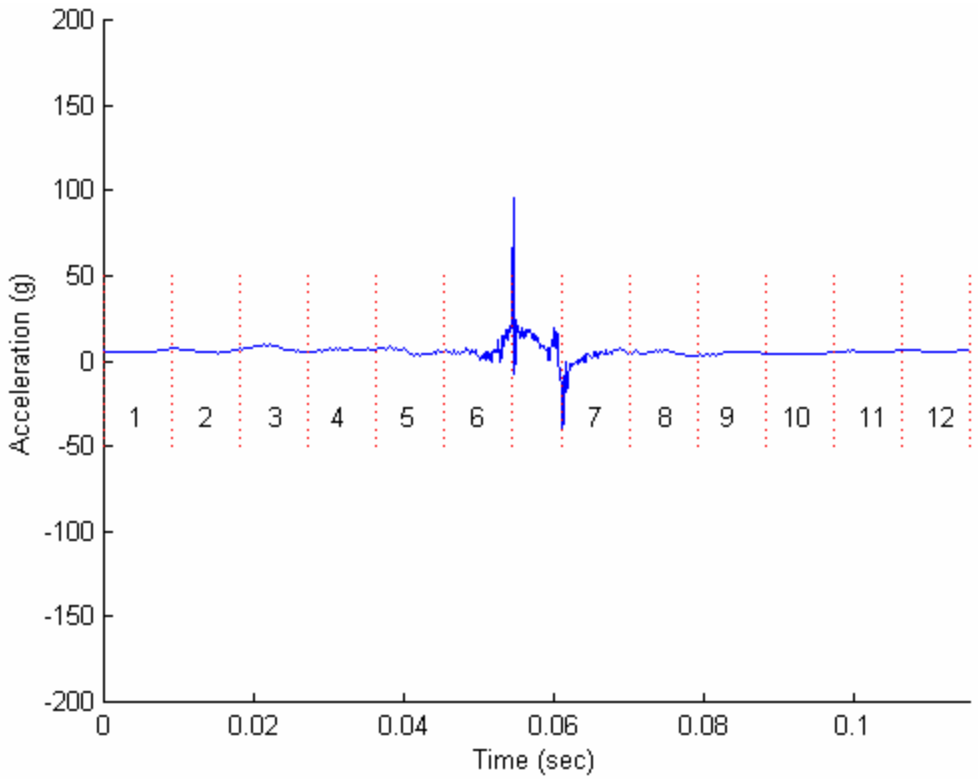

Figure **4-16**: Segmented entrance and exit to contact patch of one rotation of axial acceleration measured on smooth pavement at 40 mph.

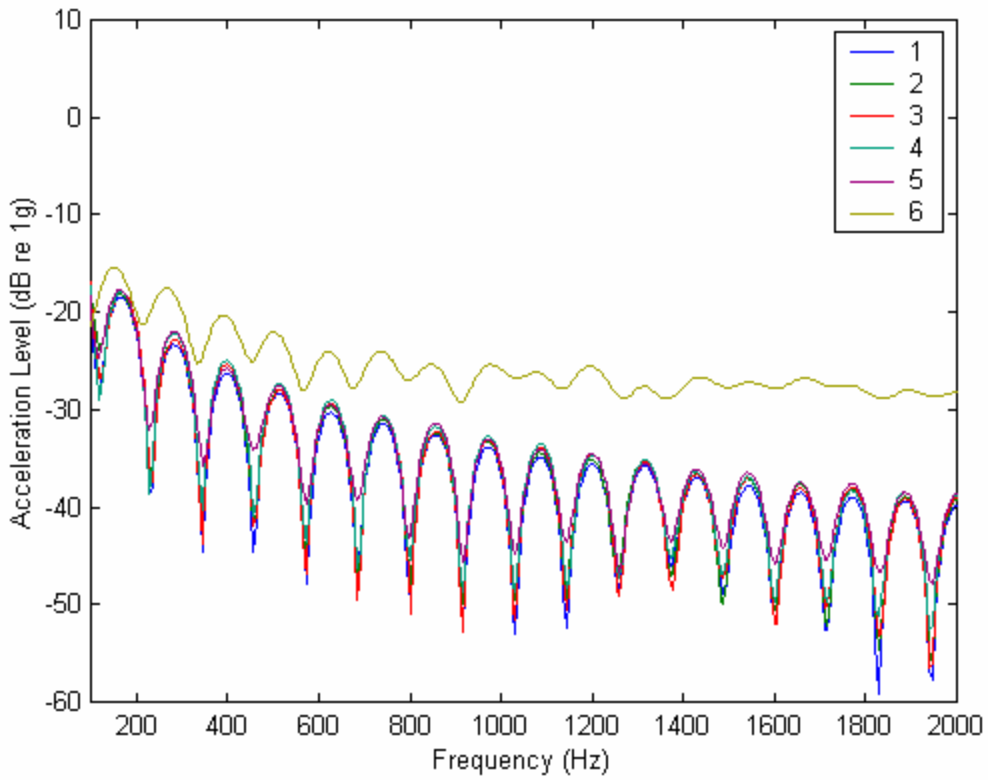

Figure **4-17**: Vibration spectra of segments in entrance to contact patch measured in the axial direction on smooth pavement at 40 mph The frequency resolution is 6 Hz.

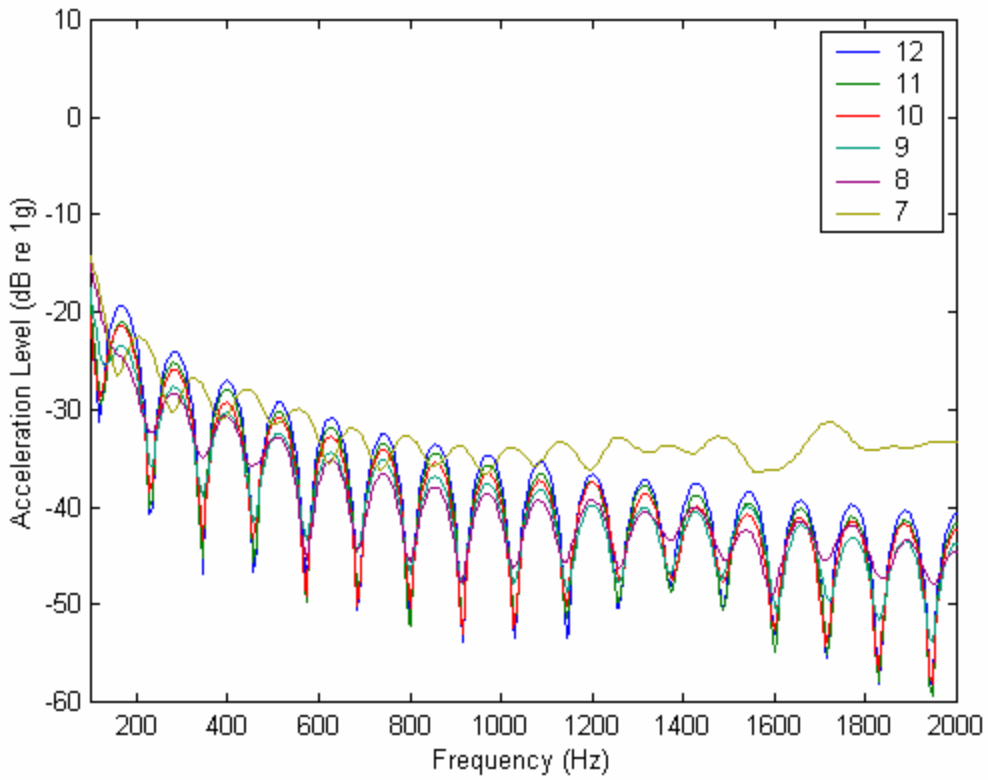

Figure **4-18**: Vibration spectra of segments in exit to contact patch measured in the axial direction on smooth pavement at 40 mph. The frequency resolution is 6 Hz.

4.2.1.5 Vibration Spectra for Three Accelerometer Orientations

The vibration levels measured at 40 mph by the three accelerometer orientations in segment 6 of the entrance to the contact patch are shown in Figure 4-19. Similarly, the vibration levels measured in segment 7 of the contact patch are given in Figure 4-20. From these figures, it is apparent that the radial acceleration levels are dominant among the three orientations. In segment 6, the radial acceleration levels are 15-20 dB higher than the levels measured by the accelerometers in the axial and tangential directions. In

comparison, the exit segment 7 has radial acceleration levels about 10 dB higher than the axial and tangential acceleration levels, as shown in Figure 4-20.

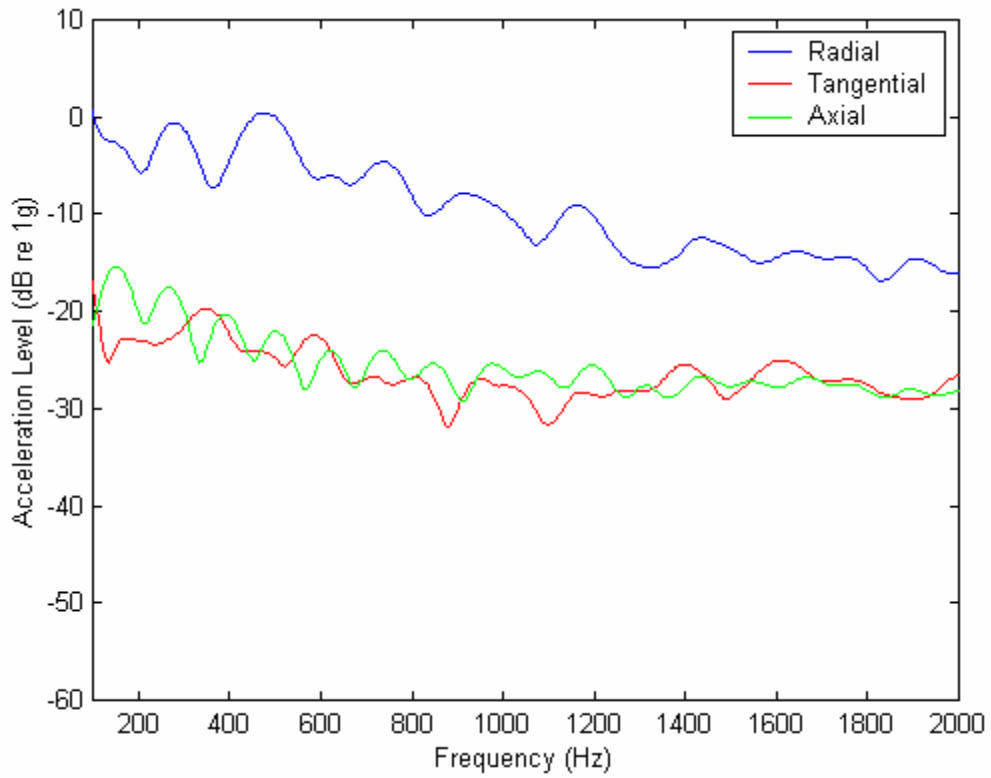

Figure **4-19**: Comparison of radial, tangential, and axial acceleration over smooth pavement at 40 mph in segment 6 of the entrance to the contact patch. The frequency resolution is 6 Hz.

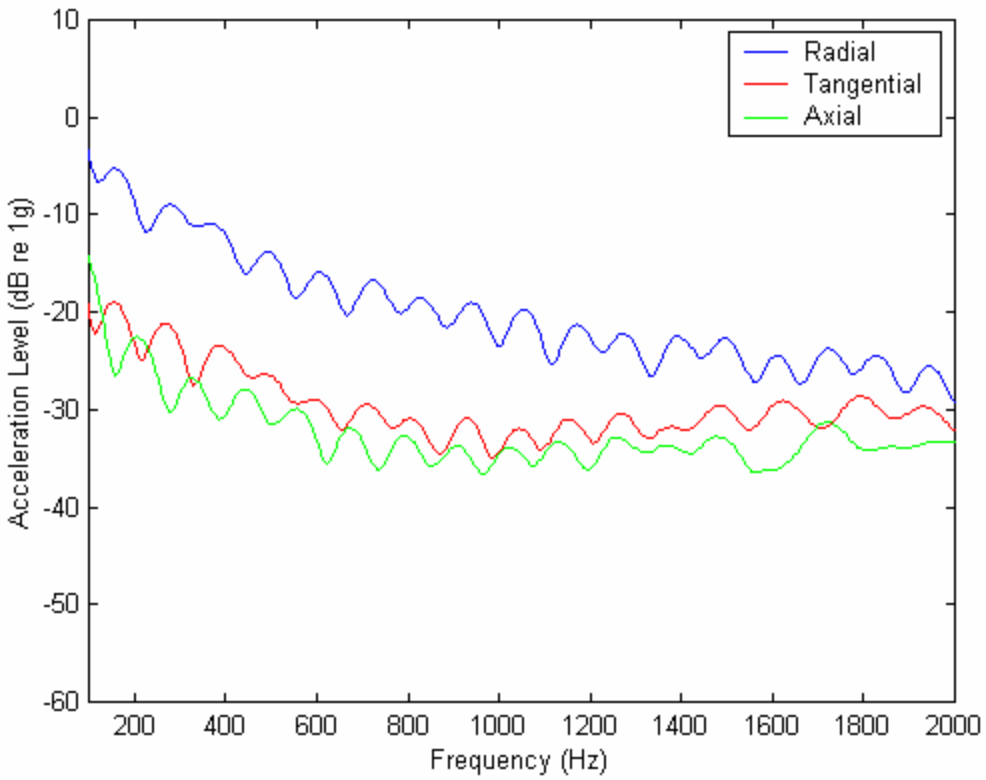

Figure **4-20**: Comparison of radial, tangential, and axial acceleration over smooth pavement at 40 mph in segment 7 of the exit to the contact patch. The frequency resolution is 6 Hz.

The comparison of the radial, tangential, and axial acceleration at 20 mph in segments 6 and 7 are shown in Figures 4-21 and 4-22. At this lower speed, the relative levels for the three orientations differ from the relative levels at 40 mph. At 20 mph, the levels of the axial vibrations fall in between the levels for the radial and tangential vibrations.

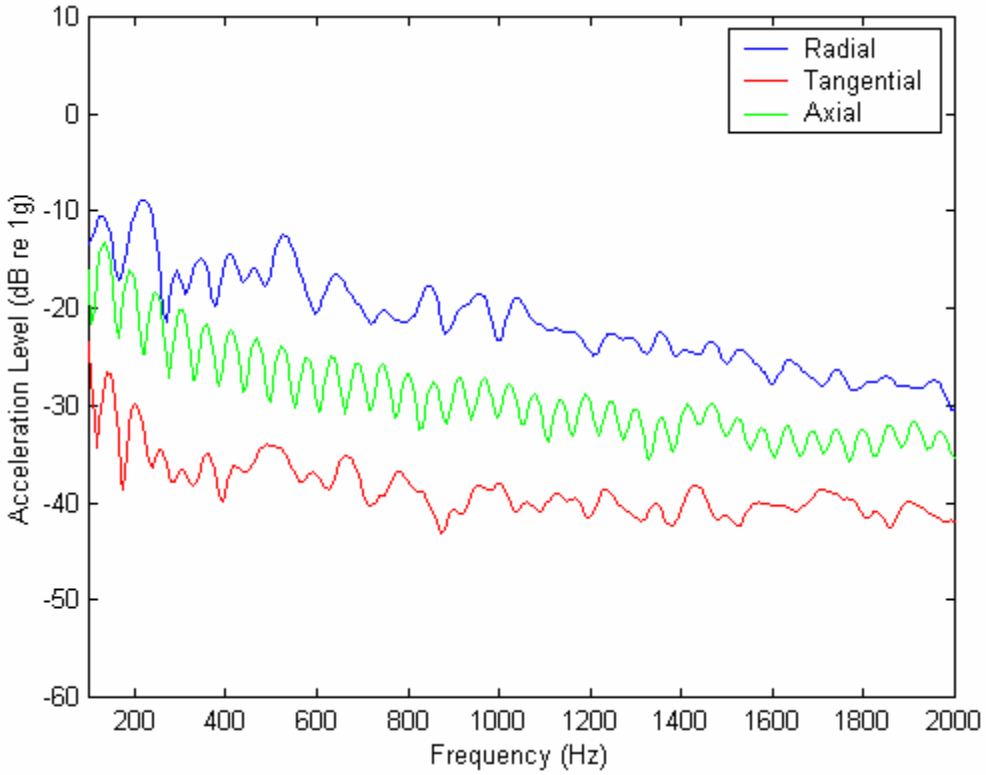

Figure **4-21**: Comparison of radial, tangential, and axial acceleration over smooth pavement at 20 mph in segment 6 of the exit to the contact patch. The frequency resolution is 6 Hz.

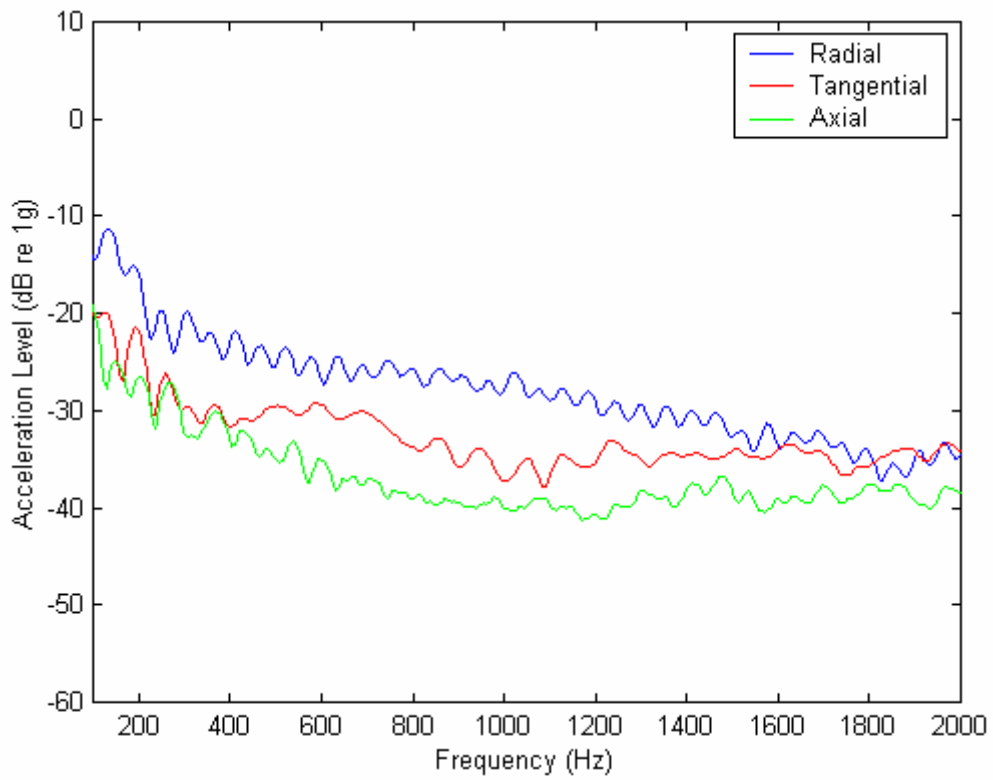

Figure **4-22**: Comparison of radial, tangential, and axial acceleration over smooth pavement at 20 mph in segment 7 of the exit to the contact patch. The frequency resolution is 6 Hz.

4.2.2 Removing Non-Radiating Component

Two methods were considered to remove the non-radiating acceleration component from the time traces prior to determining the frequency spectra. The simplest method was to determine the average of the recorded signal over several tire rotations and subtract this from the signal recorded over one rotation. The other method involves developing an analytic model that would predict the non-radiating component.

4.2.2.1 Average Several Periods of Rotation

To approximate the non-radiating component of the acceleration measured by the embedded accelerometer, an average of twenty rotations was calculated. The average was then subtracted from a single rotation so that the remaining vibrations were essentially the radiating portion of the measured signal.

4.2.2.1.1 Various Speeds

Averages were taken of twenty rotations of the radial acceleration on smooth pavement at various speeds. The average signals are pictured in Figure 4-23. These were then subtracted from the original signals recorded over one rotation shown earlier in Figure 4-1. The resulting vibrations, considered the radiating component of the acceleration, are pictured in Figure 4-24.

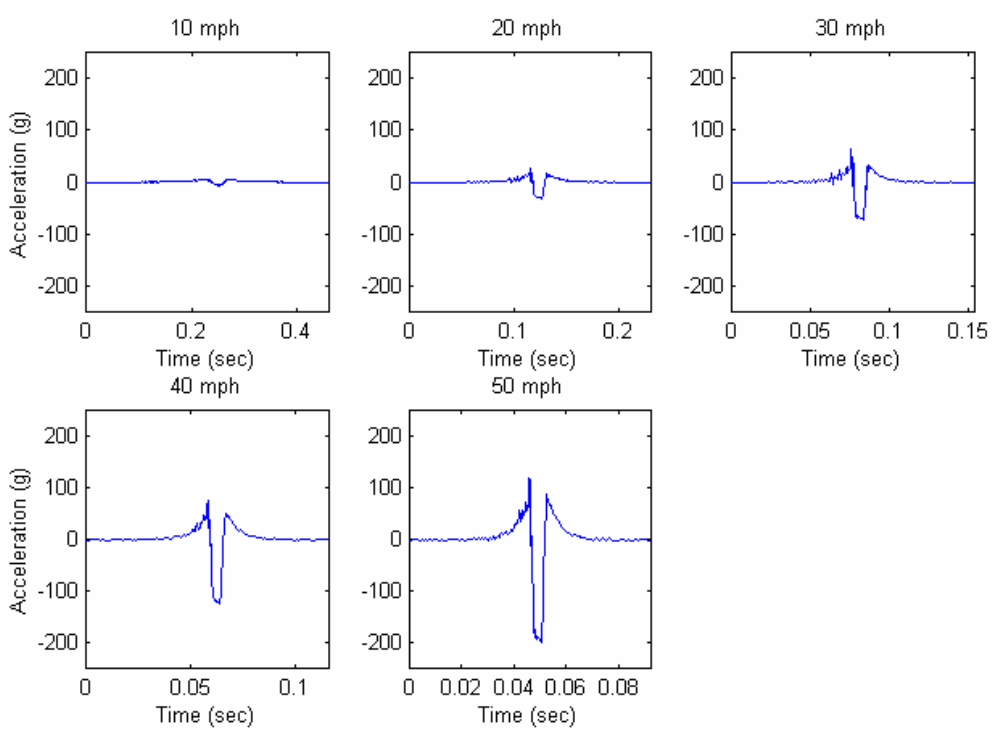

Figure **4-23**: Averages of twenty rotations of radial acceleration on smooth pavement at various speeds.

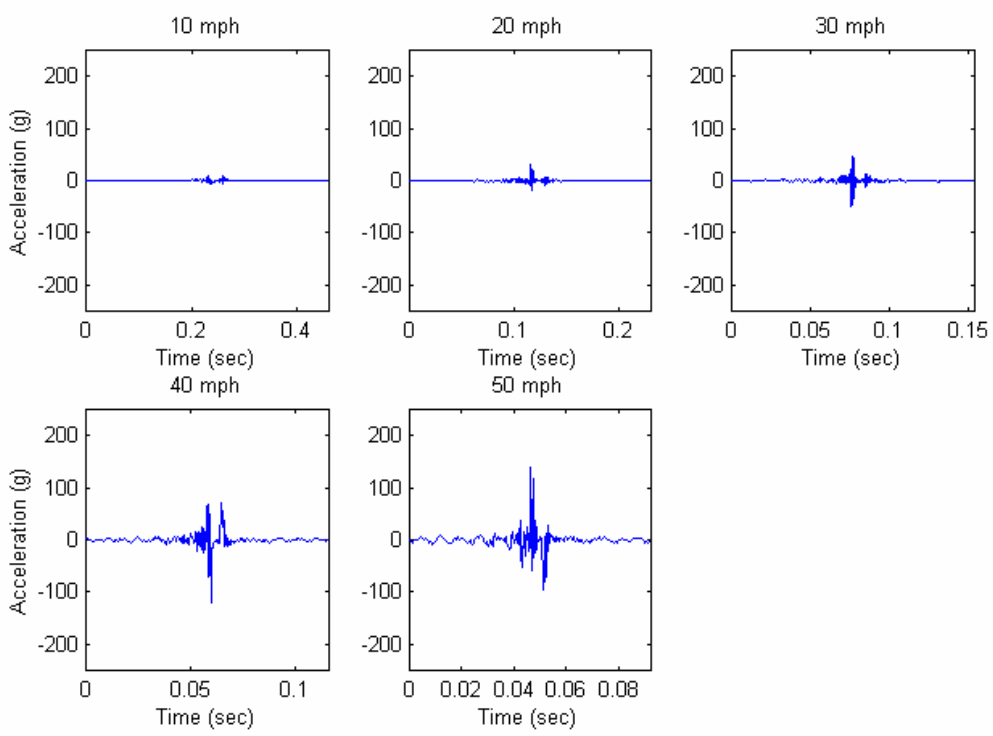

Figure **4-24**: Radiating component of radial acceleration on smooth pavement.

The frequency spectra computed over a full rotation of the accelerations with the averages subtracted at various speeds are shown in Figure 4-25 for the tire on the smooth surface. From this graph, it is clear that the random vibration levels increase with speed, although, at speeds of 30, 40, and 50 mph, the vibration levels in the frequencies over 1200 Hz are similar. The radiated noise was also measured by a microphone located 10 feet from the sidewall of the tire. The frequency spectra of the radiated noise measured over a single rotation of each of the five speeds are given in Figure 4-26. These noise levels correspondingly increase with speed.

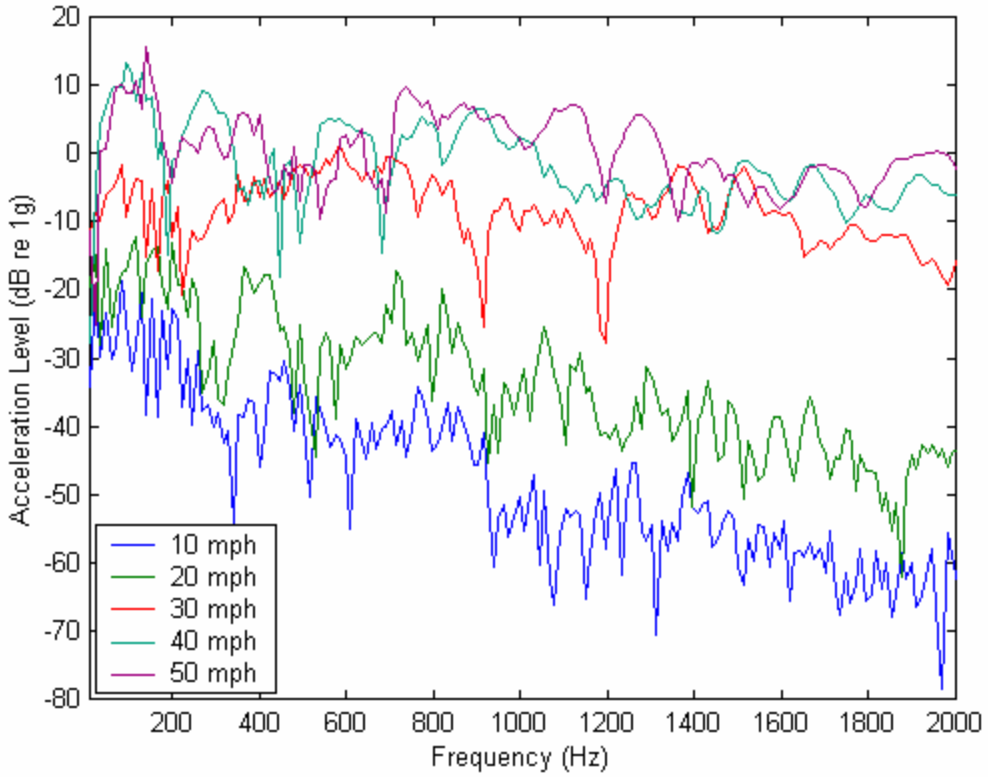

Figure **4-25**: Frequency spectra of radial acceleration at various speeds on smooth pavement. The frequency resolution is 12 Hz.

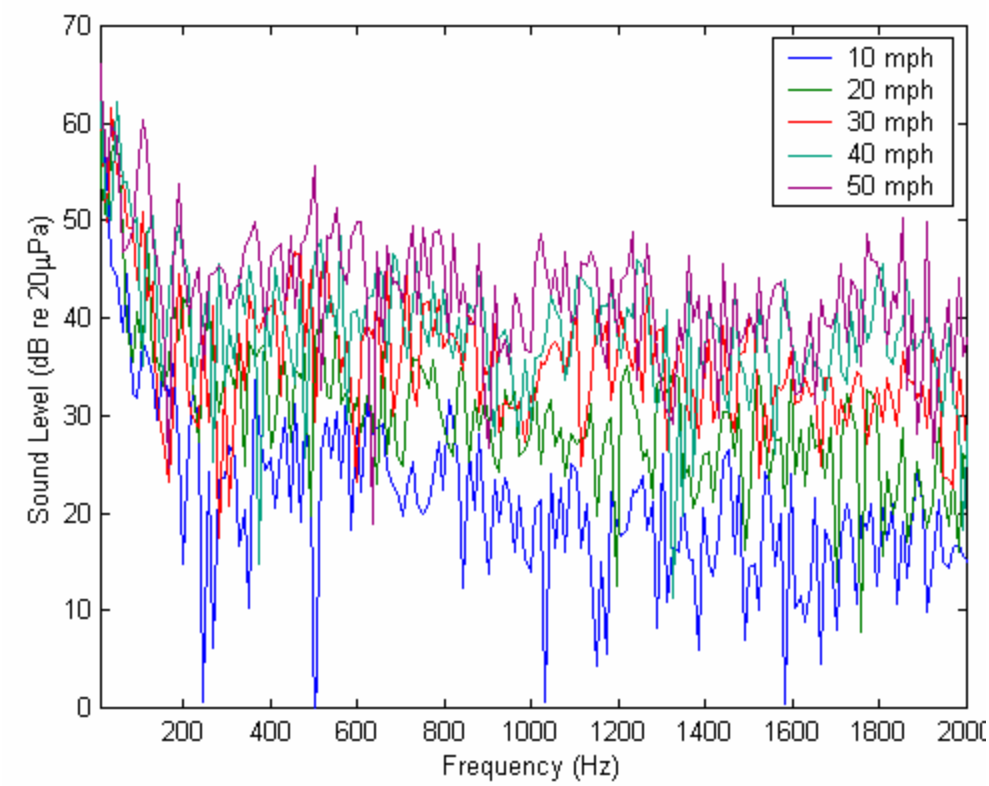

Figure **4-26**: Frequency spectra of radiated noise measured at various speeds on smooth pavement. The frequency resolution is 12 Hz.

For the spectra shown in Figure 4-25, the Fourier transform was performed over a single rotation with the average removed. To improve the statistical sampling, the spectra could also be computed from the radiating component found by subtracting the averaged signal from the signal recorded over individual tire rotations and averaging these results. However, time did not permit the development of the software required to compute these averages.

4.2.2.1.2 Smooth and Rough Pavements

The averages of twenty rotations of radial acceleration on smooth and rough pavements at 20 mph are shown in Figure 4-27. The time traces of one period of rotation with the averages subtracted from the single rotations of acceleration shown in Figure 4-3 are given in Figure 4-28.

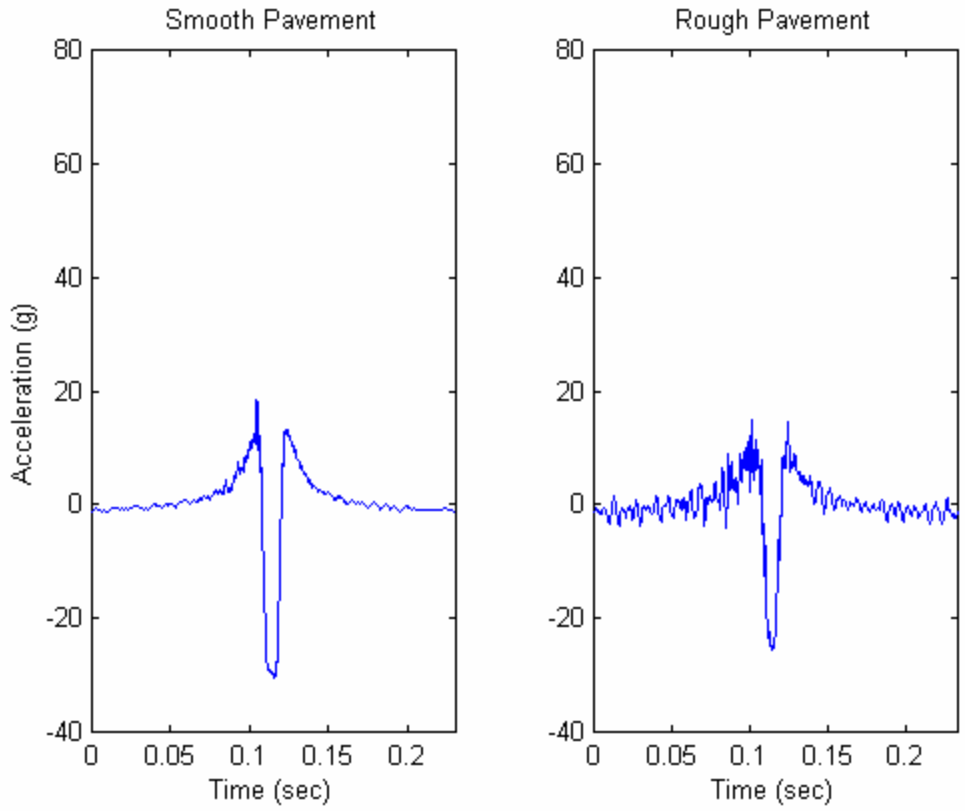

Figure **4-27**: Averages of radial acceleration on smooth and rough pavements at 20 mph.

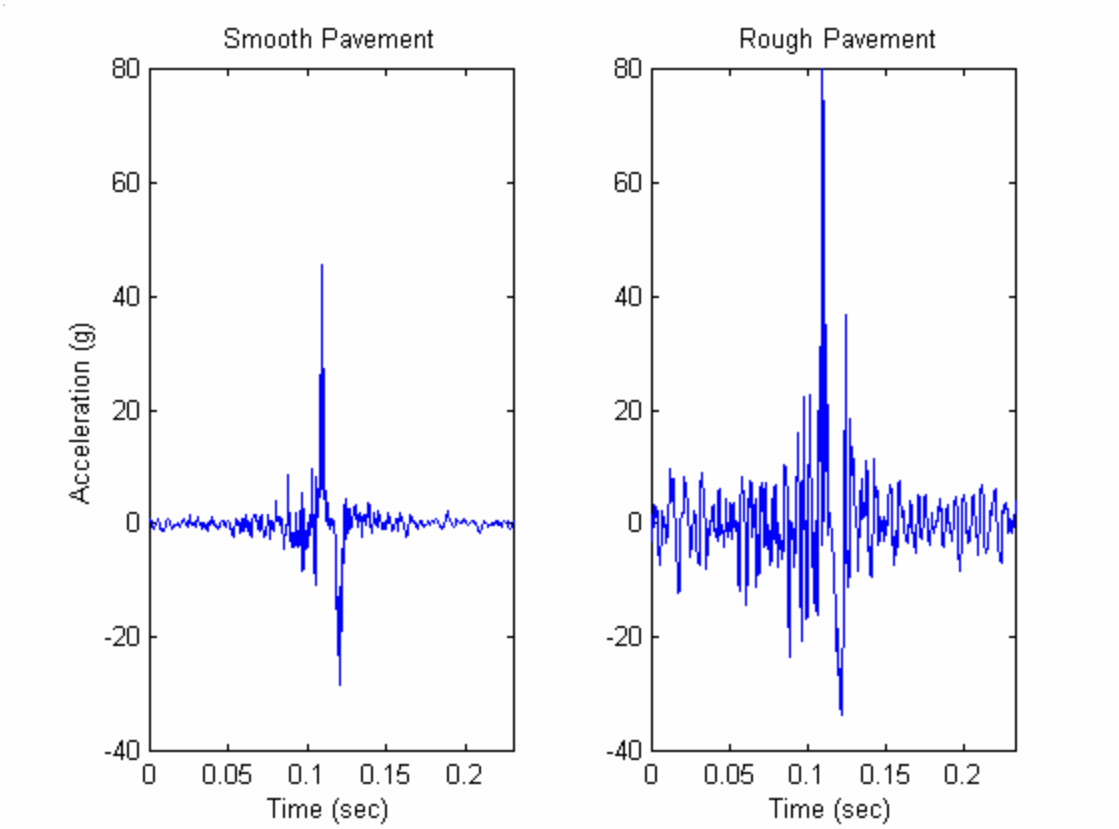

Figure **4-28**: Radiating component of radial acceleration on smooth and rough pavements at 20 mph.

The frequency spectra of the signals with the averages subtracted are shown in Figure 4-29 comparing vibrations measured on the smooth and rough pavements. The spectrum with the tire on the rough surface exhibits vibration levels higher than the levels measured with the tire on the smooth surface by approximately 10 to 15 dB, especially in the lower frequencies. The radiated noise levels measured during this test, shown in Figure 4-30 also show a difference of 10 to 15 dB in the lower frequencies.

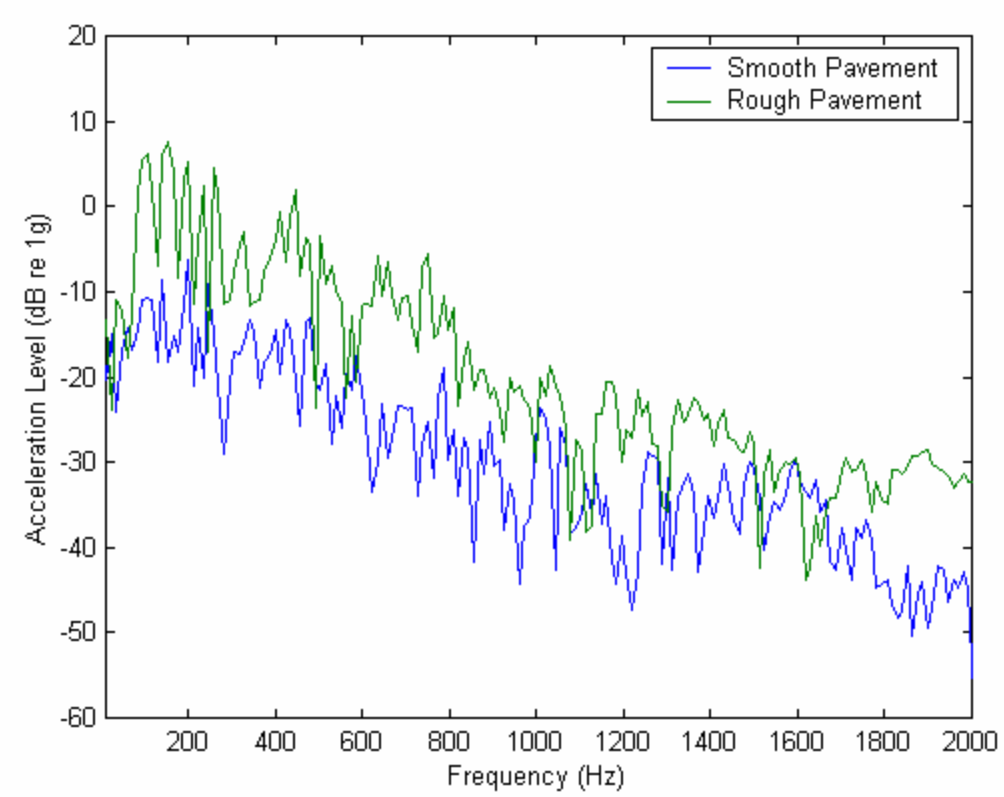

Figure **4-29**: Frequency spectra of radial acceleration at 20 mph on smooth and rough pavements. The frequency resolution is 12 Hz.

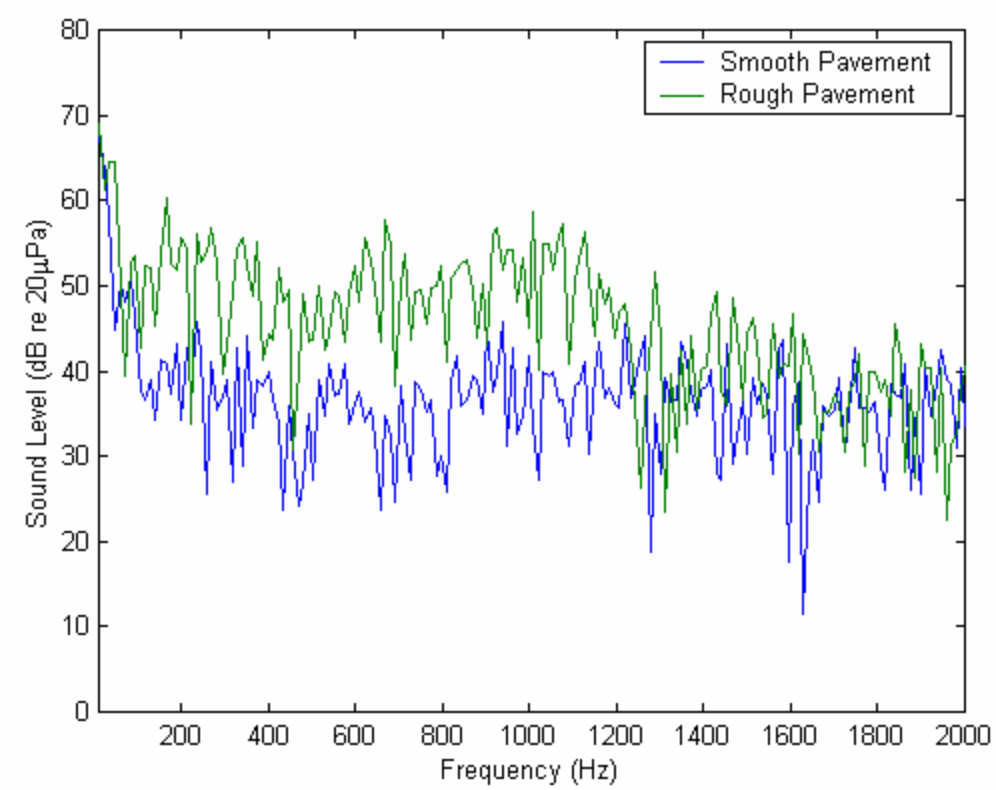

Figure **4-30**: Radiated noise measured at 20 mph on smooth and rough pavements. The frequency resolution is 12 Hz.

To discern which tire/pavement noise mechanism is responsible for the increased noise levels on the rough pavement, a transfer function is determined between the noise and vibration levels. The transfer functions, L_n-L_v, between the radiated noise levels, L_n, and measured vibration levels, L_v, are shown for all speeds on smooth pavement in Figure 4-31 and on rough pavement in Figure 4-32.

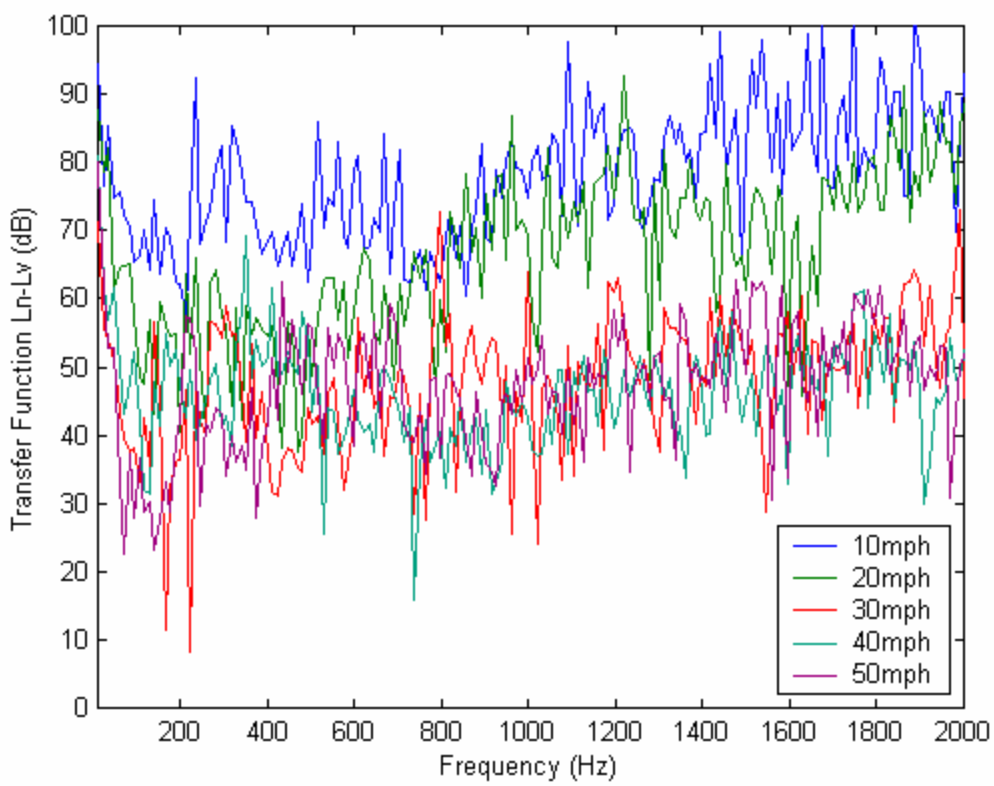

Figure **4-31**: Transfer functions between radiated noise and measured radial acceleration vibration levels for all speeds on smooth pavement. The frequency resolution is 12 Hz.

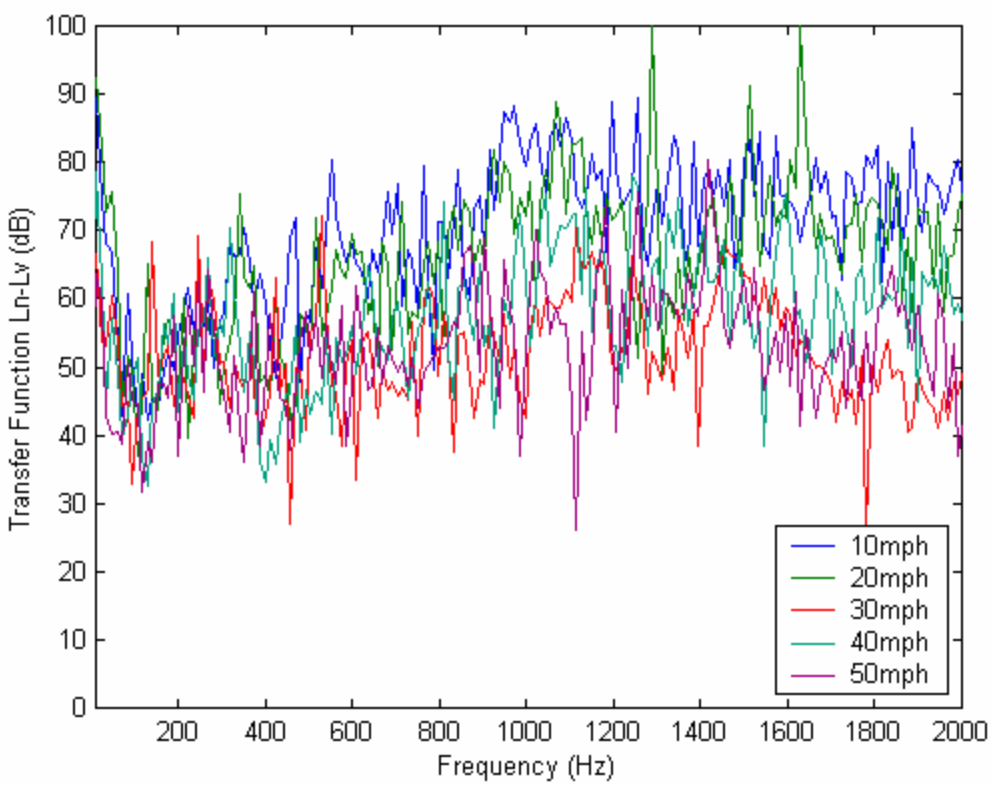

Figure **4-32**: Transfer functions between radiated noise and measured radial acceleration vibration levels for all speeds on rough pavement. The frequency resolution is 12 Hz.

In Figures 4-31 and 4-32, it is hard to distinguish between all of the lines and the levels for the speeds 30, 40, and 50 mph, so the average of the transfer functions at these three speeds are plotted with the transfer functions at 10 and 20 mph in Figure 4-33 and Figure 4-34, where averages were taken over frequency bands. These two figures show that the transfer functions at the two lower speeds on the smooth pavement are higher than for those on the rough pavement. It is difficult to tell what the cause of this might be. The averaged transfer functions for speeds 30, 40, and 50 mph on smooth and rough pavement are shown in Figure 4-35. This figure shows the transfer function for the rough pavement to be higher than the smooth pavement transfer function, which can be

attributed to the pumping of air between the voids in the pavement and the blank tire tread.

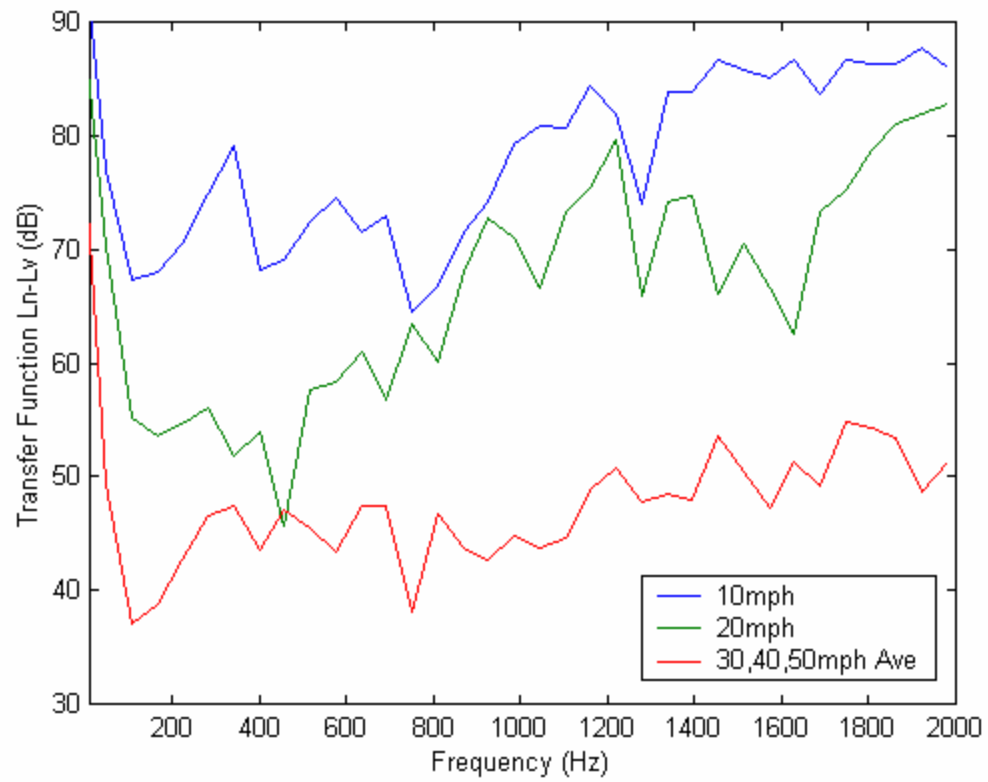

Figure **4-33**: Transfer functions between radiated noise and measured radial acceleration vibration levels for all speeds on smooth pavement with speeds 30-50 mph averaged.

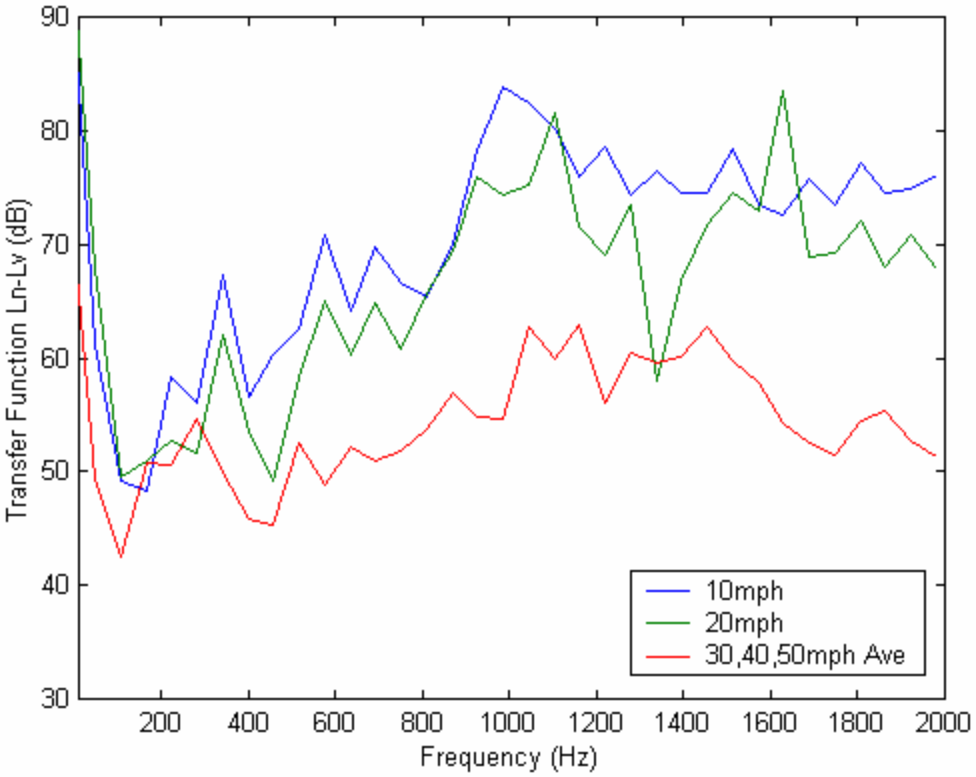

Figure **4-34**: Transfer functions between radiated noise and measured radial acceleration vibration levels for all speeds on rough pavement with speeds 30-50 mph averaged.

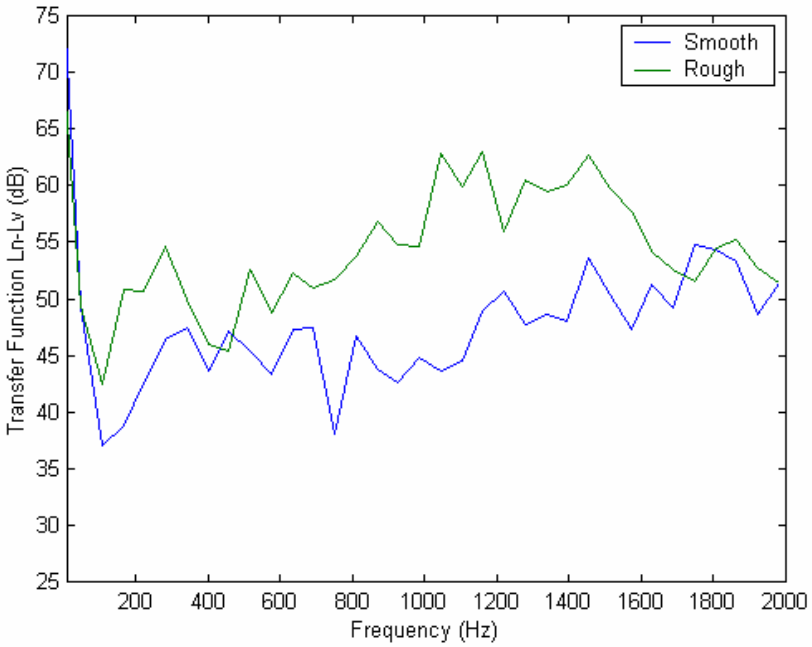

Figure **4-35**: Transfer functions between radiated noise and measured radial acceleration vibration levels on smooth and rough pavements at speeds 30-50 mph averaged.

4.2.2.1.3 Radial, Axial, and Tangential Acceleration

Twenty rotations of radial, axial, and tangential acceleration on smooth pavement measured at 40 mph were averaged to produce the time traces shown in Figure 4-36. The time traces of one rotation with the averages subtracted to estimate the radiating component of the acceleration are shown in Figure 4-37.

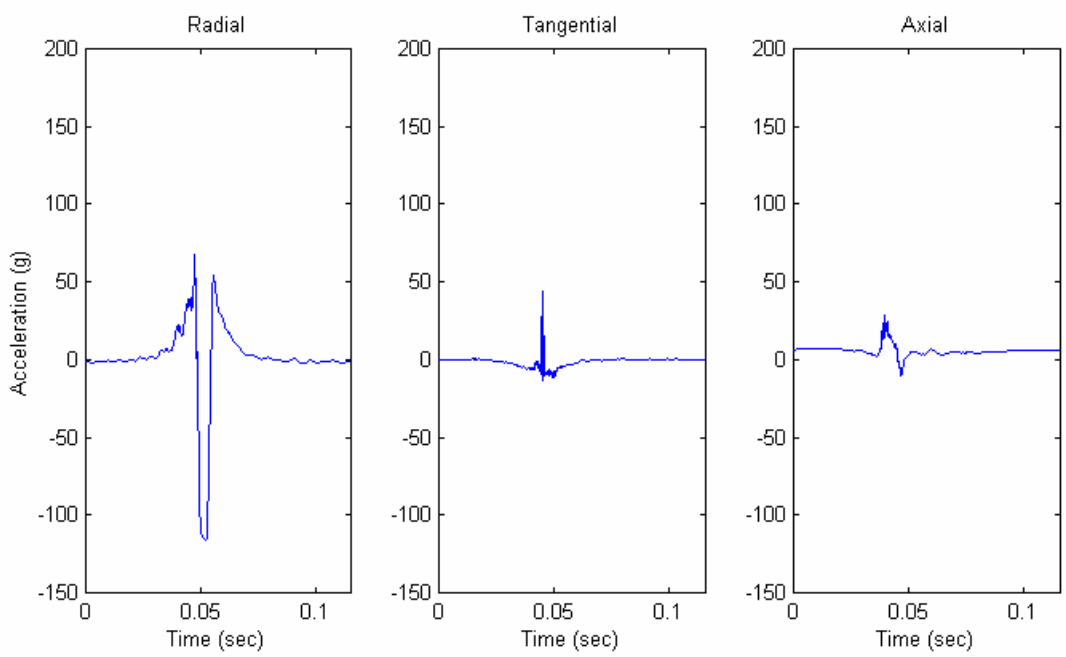

Figure **4-36**: Average of twenty rotations of radial, axial, and tangential acceleration on smooth pavement at 40 mph.

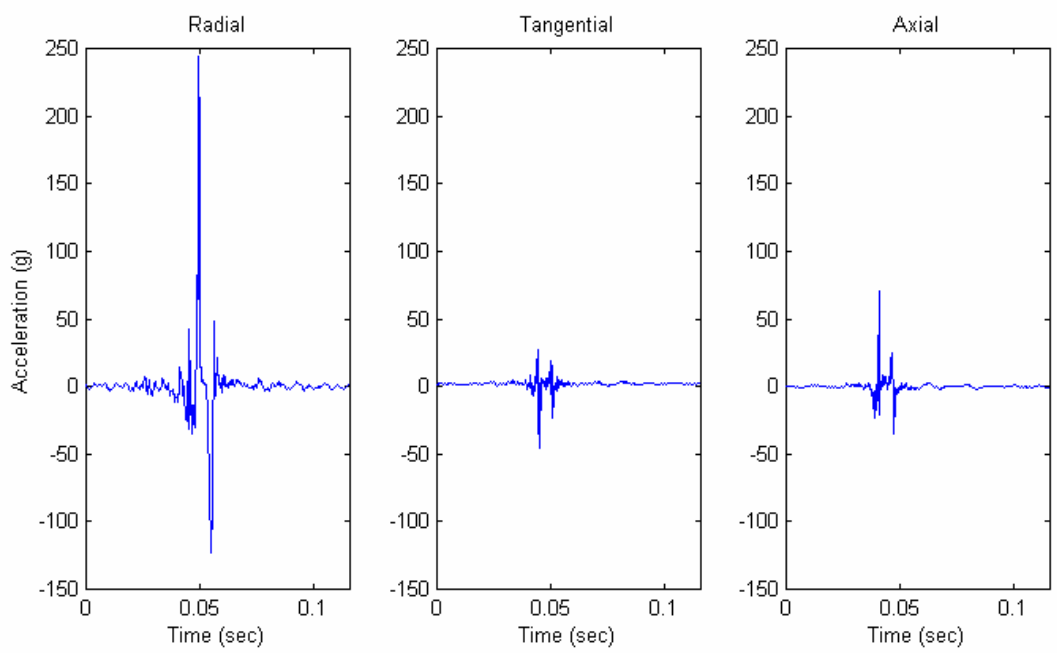

Figure **4-37**: Radiating component of radial, axial, and tangential acceleration on smooth pavement at 40 mph.

The frequency spectra of the radiating component of the measured radial, tangential, and axial acceleration signals are given in Figure 4-38. The levels of radial acceleration are almost 20 dB higher than the tangential and axial acceleration levels for frequencies below 1200 Hz; however at frequencies above 1200 Hz, all three of the orientations tend to have similar vibration levels.

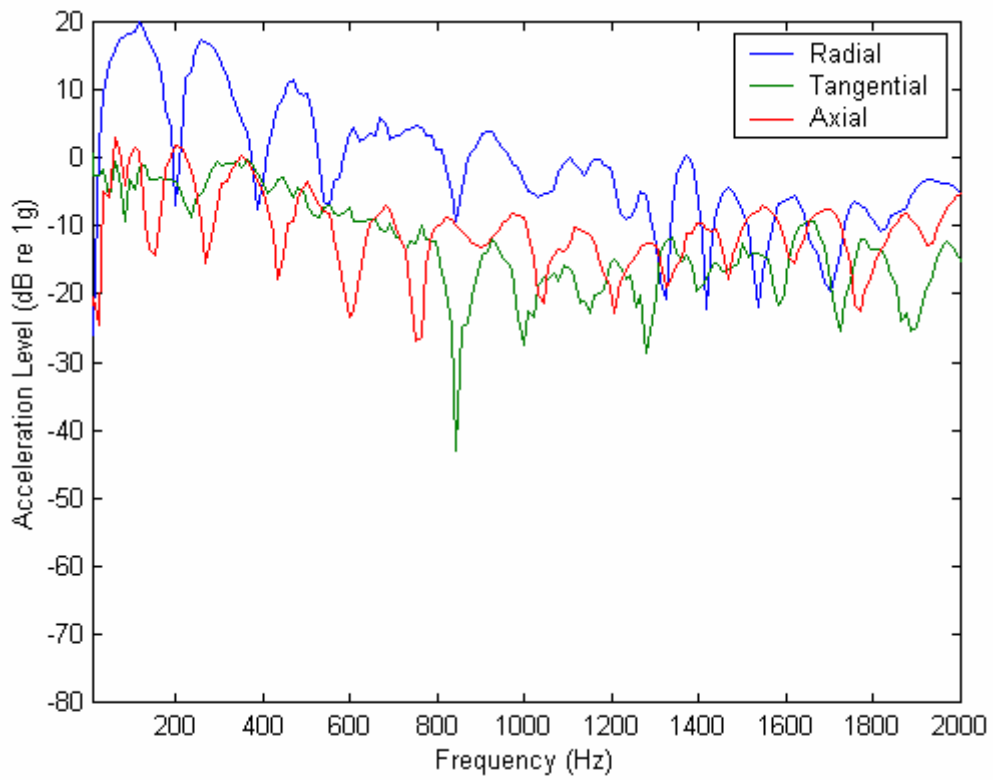

Figure **4-38**: Frequency spectra of radial, tangential, and axial acceleration on smooth pavement at 40 mph. The frequency resolution is 12 Hz.

In comparison, Figure 4-39 shows the averaged time traces of radial, axial, and tangential acceleration on smooth pavement measured at 20 mph and the radiating component is given in Figure 4-40. The frequency spectra for the three orientations at 20 mph are shown in Figure 4-41. The spread of the acceleration levels between the three orientations is less than in the spectra measured at 20 mph and is nearly equal at frequencies above 800 Hz.

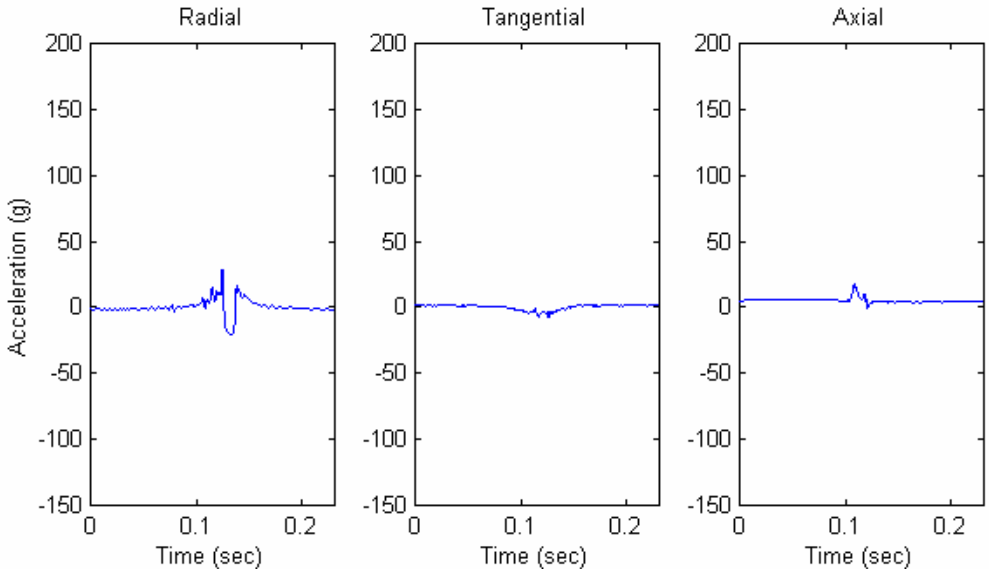

Figure **4-39**: Average of twenty rotations of radial, axial, and tangential acceleration on smooth pavement at 20 mph.

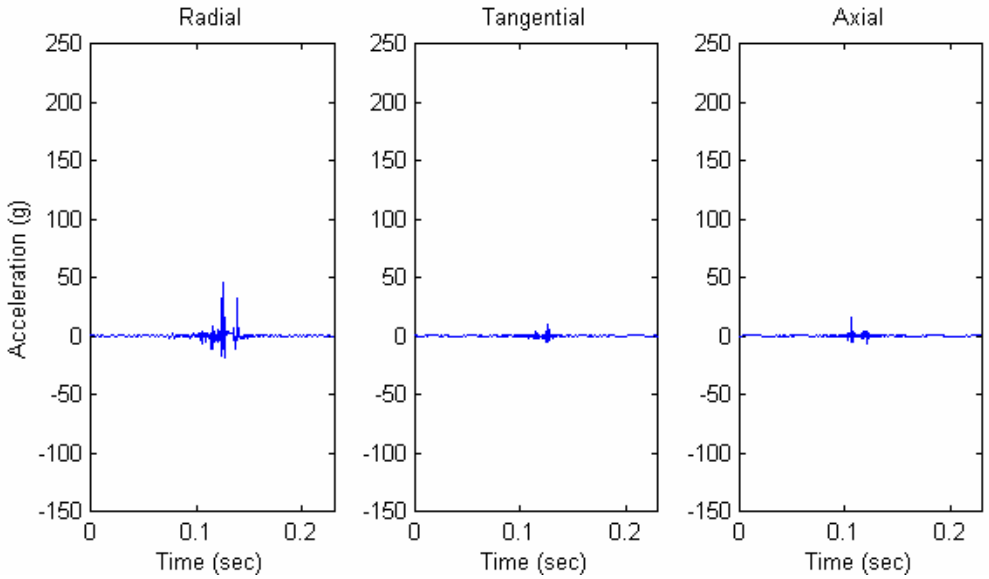

Figure **4-40**: Radiating component of radial, axial, and tangential acceleration on smooth pavement at 20 mph.

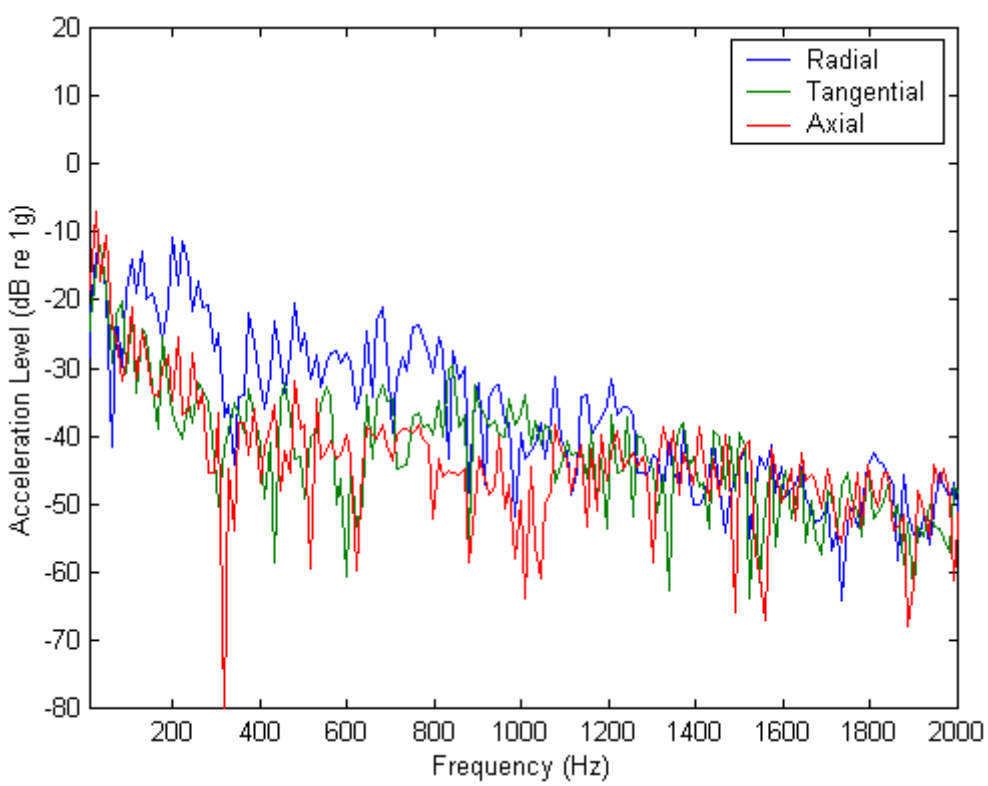

Figure **4-41**: Frequency spectra of radial, tangential, and axial acceleration on smooth pavement at 20 mph. The frequency resolution is 12 Hz.

4.2.2.2 Analytic Model

Another method for estimating the non-radiating component of the measured acceleration is to develop an analytic model to predict the vibration of a tire surface as it rotates through the contact patch. The derivation of the analytic model is discussed in Section 3.2.1 and is used to predict the radial and tangential acceleration experienced by a point on the tire as it rotates through the contact patch.

The models used to predict the non-radiating portion of the radial and tangential acceleration generally match the shape of the measured acceleration signals, however the

tangential model still had deviations from the measured signals. Therefore only the radial model will be used in this analysis. The time trace of one rotation of the analytic model superimposed upon the measured radial acceleration signal at 20 mph on smooth pavement is shown in Figure 4-42.

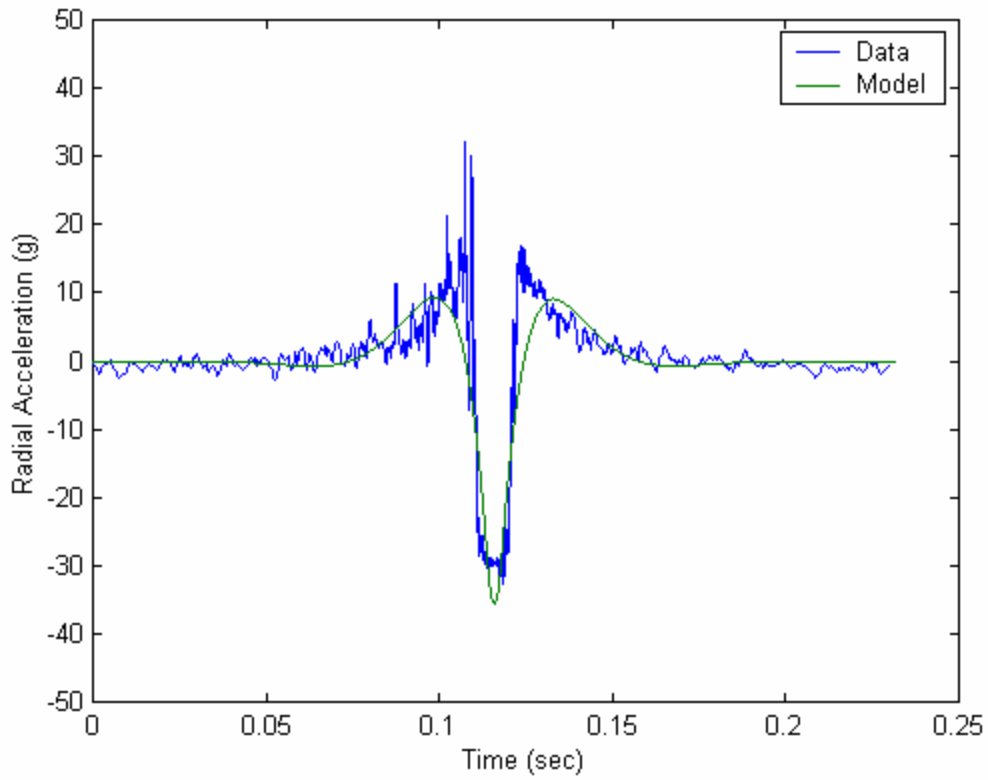

Figure **4-42**: Analytic model compared with measured radial acceleration at 20 mph on smooth pavement.

In a procedure similar to that used to remove the averaged signal from the measured signal, predictions from the analytic model were subtracted from the signal recorded during a single rotation of the tire. The radiated portion of the radial acceleration at 20 mph on smooth pavement is shown in Figure 4-43.

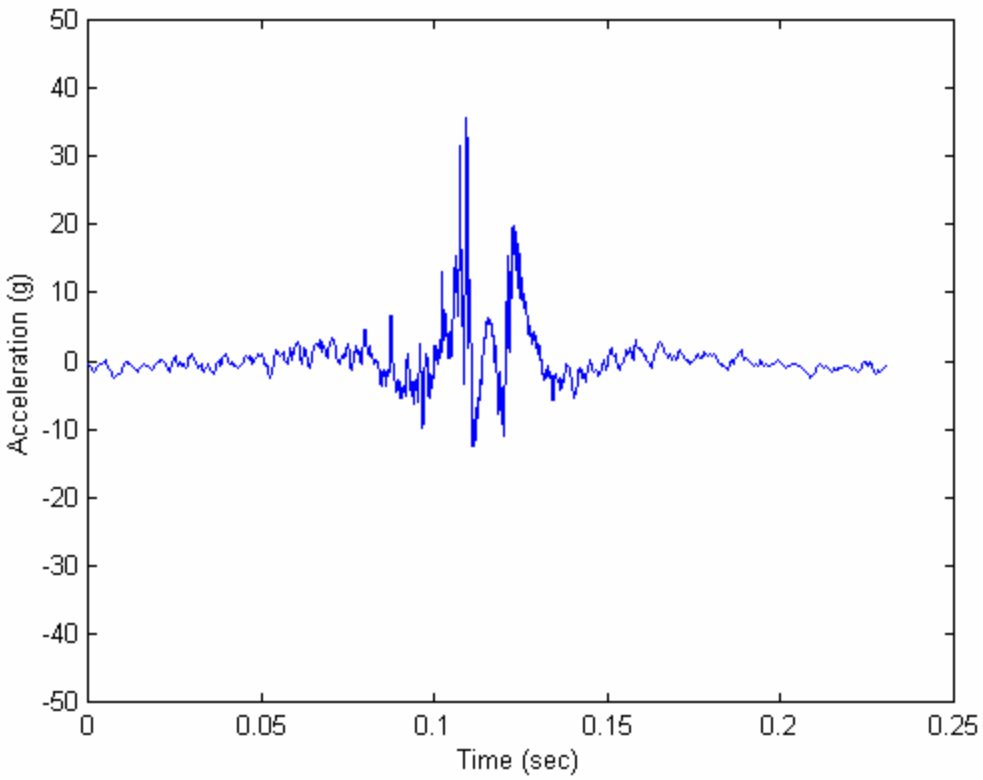

Figure **4-43**: Radiated portion of the radial acceleration at 20 mph on smooth pavement determined by subtracting analytic model.

The radiating components of the radial acceleration at all five speeds determined by subtracting the analytic model are shown in Figure 4-44. The frequency spectra of these radiating components are shown in Figure 4-45. This is very similar to the frequency spectra pictured in Figure 4-25, which was found by subtracting the average of 20 rotations, and shows that the vibration levels increase as the speed is increased. These results also indicate that the averaging produces results which are representative of the time-invariant, non-radiating component of the acceleration measured by the embedded accelerometer.

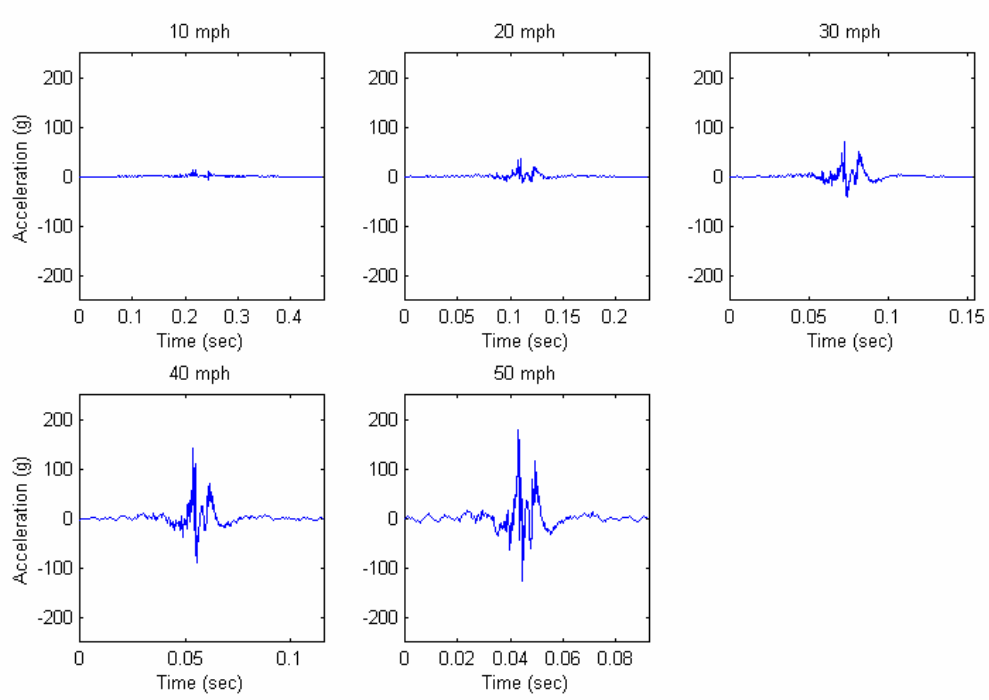

Figure **4-44**: Radiating component of radial acceleration measured on smooth pavement at speeds of 10-50 mph, computed by subtracting analytic model.

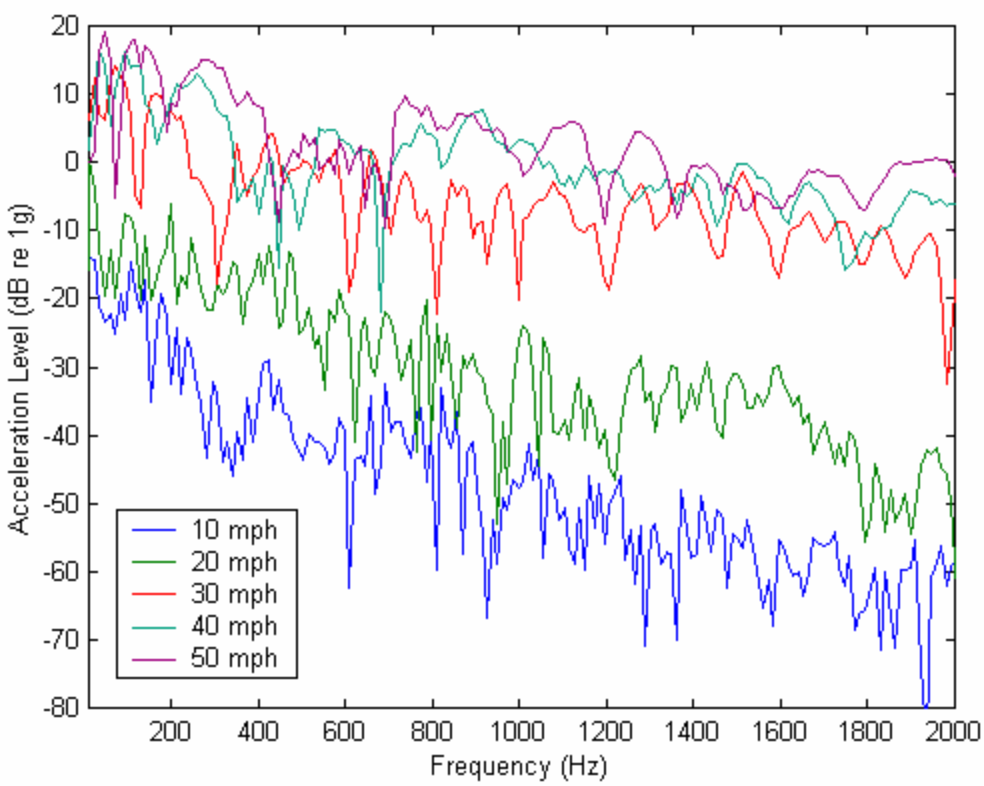

Figure **4-45**: Frequency spectra of radial acceleration measured at various speeds on smooth pavement determined by subtracting analytic model. The frequency resolution is 12 Hz.

A comparison of the analytic model with the averaged version of the non-radiating portion of the acceleration signal is shown in Figure 4-46 for the radial acceleration at 20 mph. The areas around the contact patch are not matched exactly and the average is not as smooth as the model. Improvements could be made with both methods. The average could be found over a longer period of time, greater than 20 rotations. Also, using more precise material property values in the model may create a better fit.

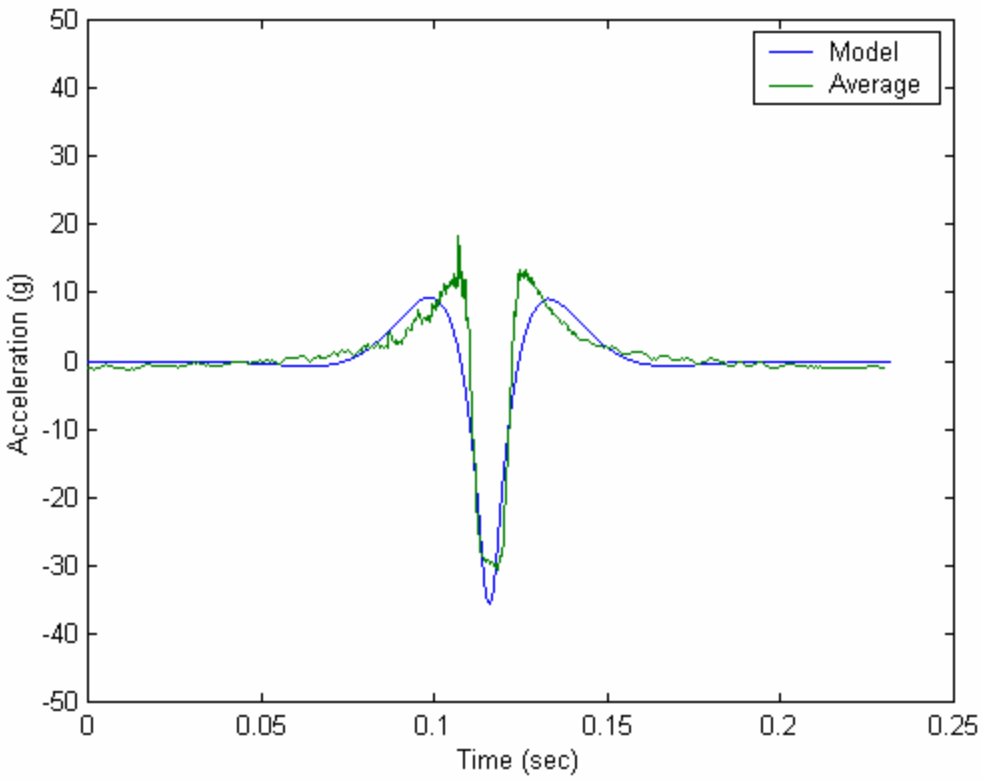

Figure **4-46**: Comparison of the analytic model with the averaged radial acceleration for 20 mph on smooth pavement..

Chapter 5

CONCLUSION

5.1 Summary

To better understand tire/pavement interaction noise, a method was developed to measure the vibration at a single location in the tire tread band as it rolled through the contact patch. Small accelerometers were successfully embedded into the surface of the tire tread band and were used to measure vibration in the tire tread. The accelerometers were oriented to measure acceleration in three directions: radial, tangential, and axial. The measurements were made on a road wheel with two pavement types, smooth and rough, at five different speeds ranging from 10 to 50 mph. Although the accelerometers were subjected to the harsh test conditions and many failed during testing, signals recorded before failure looked reasonable.

The recorded signals were processed using several methods. A single rotation was divided into several segments and their frequency spectra were compared to localize the vibrations. Also, the non-radiating components of the signals were removed so the radiating component was analyzed. The non-radiating component was approximated by averaging several rotations. The non-radiating component was also predicted using an analytic model.

5.2 Conclusions

In addition to the developing a method of mounting an accelerometer into the surface of a tire that was successful in measuring tire vibration, several other conclusions were made in this research. The research done by Ruhala was verified when it was observed that the time traces of the measured data showed that the levels of the vibrations were highest in regions close to the entrance and exit to the contact patch. In comparisons of the vibration spectra at different speeds, the vibration levels increase with speed. Also, vibration levels on rough pavement are higher than those on smooth pavement, which, in turn, were accompanied by higher radiated noise levels. Transfer functions between the measured vibration and radiated noise conducted with the blank tire on rough and smooth surfaces indicated significant contributions to the radiated noise by the pumping of air in and out of the voids in the rough surface.

Vibrations were compared for the different accelerometer configurations. It was observed that the radial acceleration levels were higher at the lower frequencies than the tangential and axial vibration levels. In addition, when the recorded signals of each orientation were segmented and analyzed, another difference was seen. The radial acceleration levels decreased as the accelerometer rotated away from the contact patch. However, in the tangential and axial measurements, the vibration appeared to be strongly localized to regions close to the contact patch.

Finally, it was concluded that there are several methods to successfully analyze the radiating portion of the measured acceleration signals. The non-radiating component

can be approximated either by averaging several rotations or using the analytic model developed by Kropp and Heckl.

5.3 Recommendations

Although it was possible to obtain useful measurements of tire tread vibration with accelerometers embedded into the surface of the tires, the accelerometers did not survive for long periods of time. These accelerometers were subjected to large amounts of stress as the tire rolled through the contact patch and across different types of pavement at high speeds. A better method to keep the rubber seals attached to the tire, possibly using another sealant, needs to be developed so the accelerometers will survive longer, especially on rough pavement. The accelerometers were very small and light, but may also need to be tested for mass-loading effects.

The spectra computed over the different segments of the measured acceleration signal may be improved by averaging the spectra calculated over the same segments taken from several rotations.

Averaging the recorded signal over twenty rotations to approximate the non-radiating component of the acceleration appeared to work fairly well. More rotations could have been averaged to create a more accurate representation of the non-radiating component. Also, the statistical sampling could have been improved by averaging the spectra over several cycles of the radiating component instead of over just one rotation, as was done in this research.

More work can also be done with the analytic model developed for the non-radiating portion of the acceleration. It appeared that the predicted radial acceleration matches the general shape of the recorded signals, but a close fit to the measured data was not obtained in the tangential direction. A possibility for the deviation of the tangential acceleration model may have been due to errors in the measured data and not the predictions. Some adjustments may need to be made to the tire constants used in the analytic model to provide a more accurate representation of the tires used in the research because the values used for the Young's modulus and the tension were determined simply by adjusting them until they fit the frequencies of resonance and the shape of the measured acceleration. Also, because the analytic model only predicts the acceleration in two dimensions, it may not accurately predict the acceleration in the tangential direction.

5.4 Future Work

With the ability to embed accelerometers into the surface of a tire, much more work can be done in the measurements of the tire tread band vibrations through the contact patch.

Using the blank tires, arrays of radial accelerometers can be embedded into the tire surface. The measurements can be analyzed to find the coherence between the vibrations measured by accelerometers in different locations to detect propagating waves and wave speeds. The speed-dependence of transfer functions between the radiated noise and measured acceleration should be investigated further.

The accelerometers can also be embedded into the surfaces of different types of treaded tires to investigate the offset of grooves on the vibrations of tread elements. Pressure sensors can be embedded into the spaces between the tread blocks to measure the pressure experienced as it travels through the contact patch.

Bibliography

1. Garcia, A., ed. *Environmental Urban Noise*, Southampton: WIT Press, 2001.

2. European Commission Green Paper. *Future Noise Policy*, Brussels, 1996.

3. Sandberg, U., "Noise Emissions of Road Vehicles - Effect of Regulations," *Noise/News International* 3 (July 2001) 150-206.

4. U.S. Department of Transportation, Federal Highway Administration, *Highway Traffic Noise*, Online, Internet. 3 July 2002.

5. Sandberg, U. "Road Traffic Noise - The Influence of the Road Surface and its Characterization," *Applied Acoustics* 21 (1987) 97-118.

6. Klos, Jacob, Fei Han, and Robert J. Bernhard, "Response Measurement of Rolling Tires Using Laser Doppler Vibrometry," *Proceedings Inter-noise* 2002.

7. Ruhala, R., "A Study of Tire/Pavement Interaction Noise Using Nearfield Acoustical Holography," PhD. Thesis, The Pennsylvania State University, 1999.

8. Jennewein, M. and M. Bergmann, "Investigations Concerning Tyre/Road noise Sources and Possibilities of Noise Reduction," *Proceedings Institute Mechanical Engineers* 199 D3 (1985) 199-205.

9. Bergmann, M., "Noise Generation by Tyre Vibrations," *Proceedings Inter-noise* (1980) 239-244.

10. Kropp, W., "Structure-borne Sound on a Smooth Tyre," *Applied Acoustics* 26 (1989) 181-192.

11. Heckl, M., "Tyre Noise Generation," *Wear* 113 (1986) 157-170.

12. Dixon, J.C., *Tires, Suspension and Handling*, Society of Automotive Engineers Inc., Warrendale, PA, (1989) 2nd Ed., Chap. 2, 67-92.

13. Davisson, J.A., *Design and Application of Commercial Type Tires*, Society of Automotive Engineers Inc., New York, 1969.

14. Gough, V.E., S. Clark, ed., “Structure of the Pneumatic Tire,” *Mechanics of Pneumatic Tires*, U. S. Department of Transportation, Washington, D.C. (1981) 203-248.

Appendix
ADDITIONAL DATA

Results obtained during data processing not previously presented are shown in this appendix.

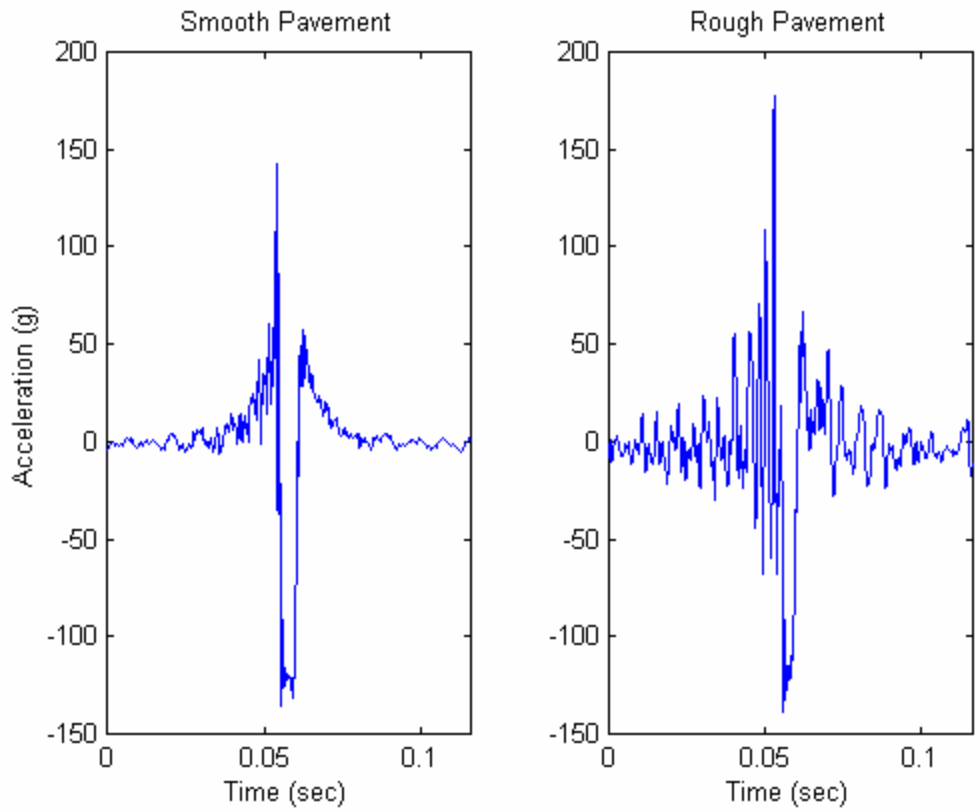

Figure A-1: One rotation of radial acceleration at 40 mph on smooth and rough pavements.

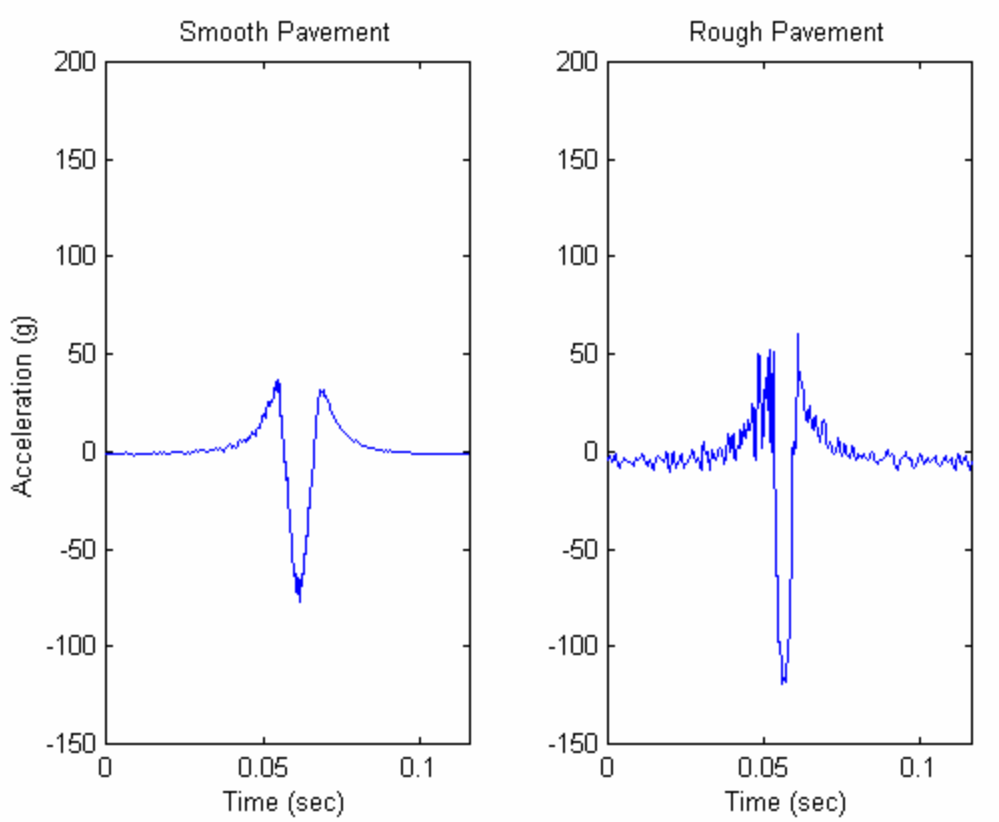

Figure A-2: Radial acceleration on smooth and rough pavement at 40 mph averaged over 20 rotations.

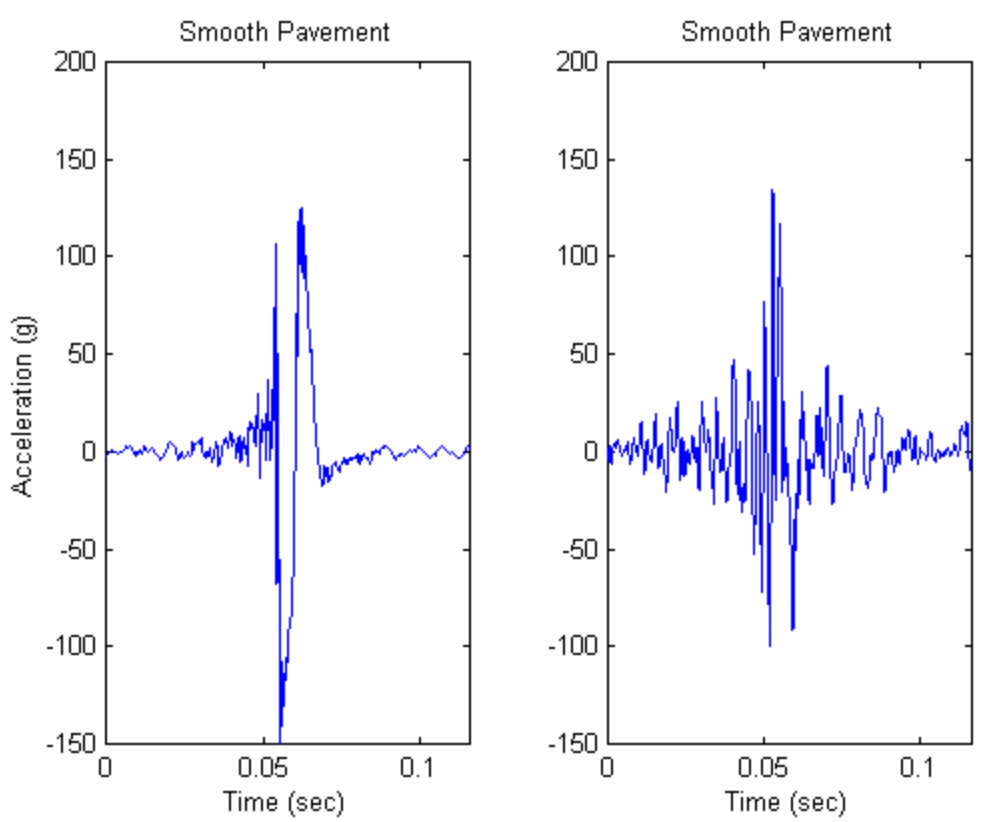

Figure A-3: Radiating component of radial acceleration on smooth and rough pavements at 40 mph, computed by subtracting the average of 20 rotations.

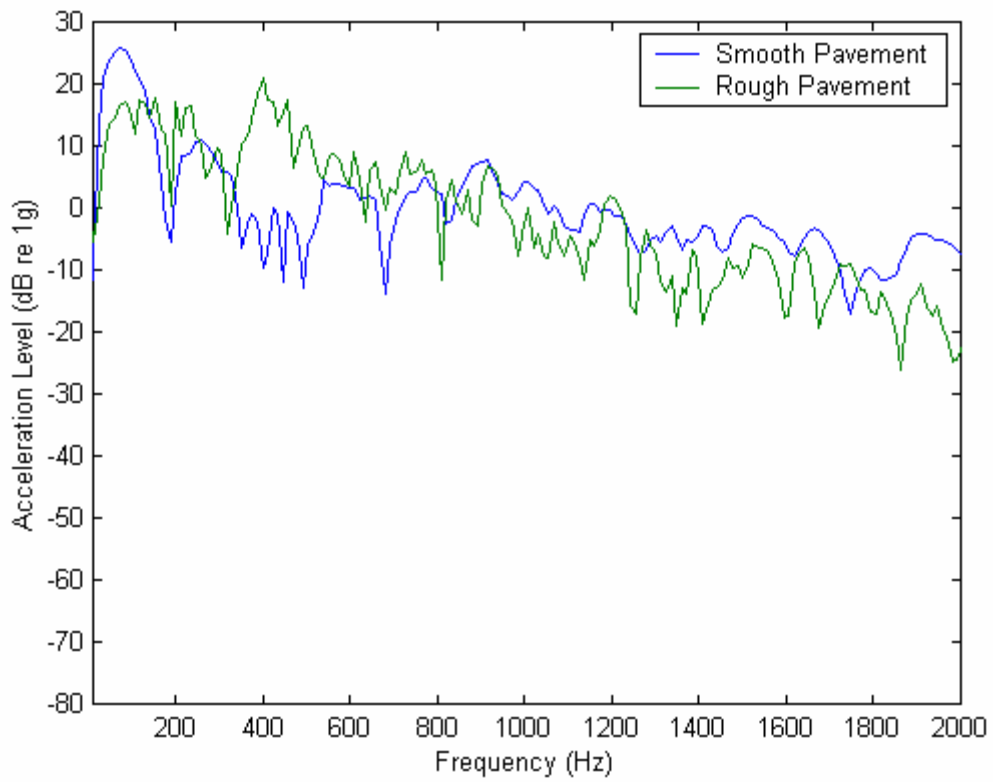

Figure A-4: Frequency spectra of radial acceleration on smooth and rough pavements at 40 mph, computed after subtracting the average of 20 rotations from a single rotation. The frequency resolution is 12 Hz.

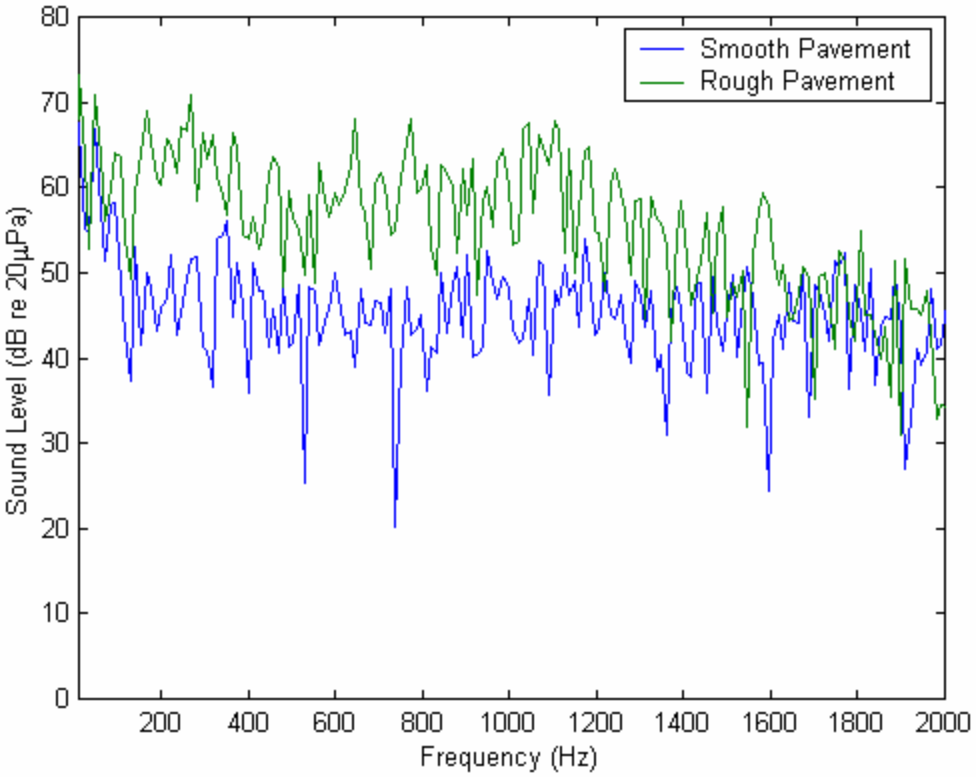

Figure A-5: Frequency spectra of radiated noise measured over one rotation at 40 mph on smooth pavement and rough pavements. The frequency resolution is 12 Hz.

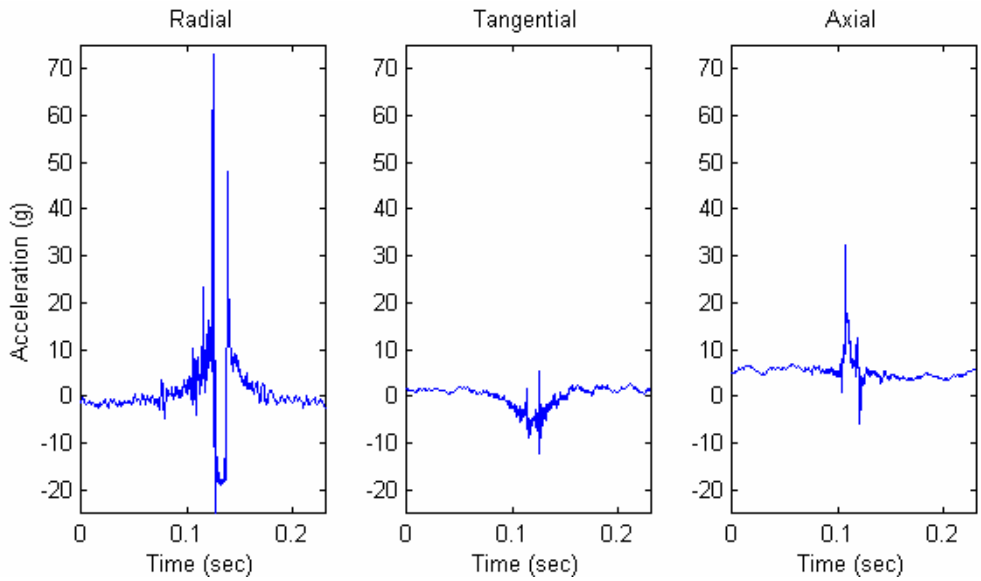

Figure A-6: One rotation of radial, tangential, and axial acceleration on smooth pavement at 20 mph.

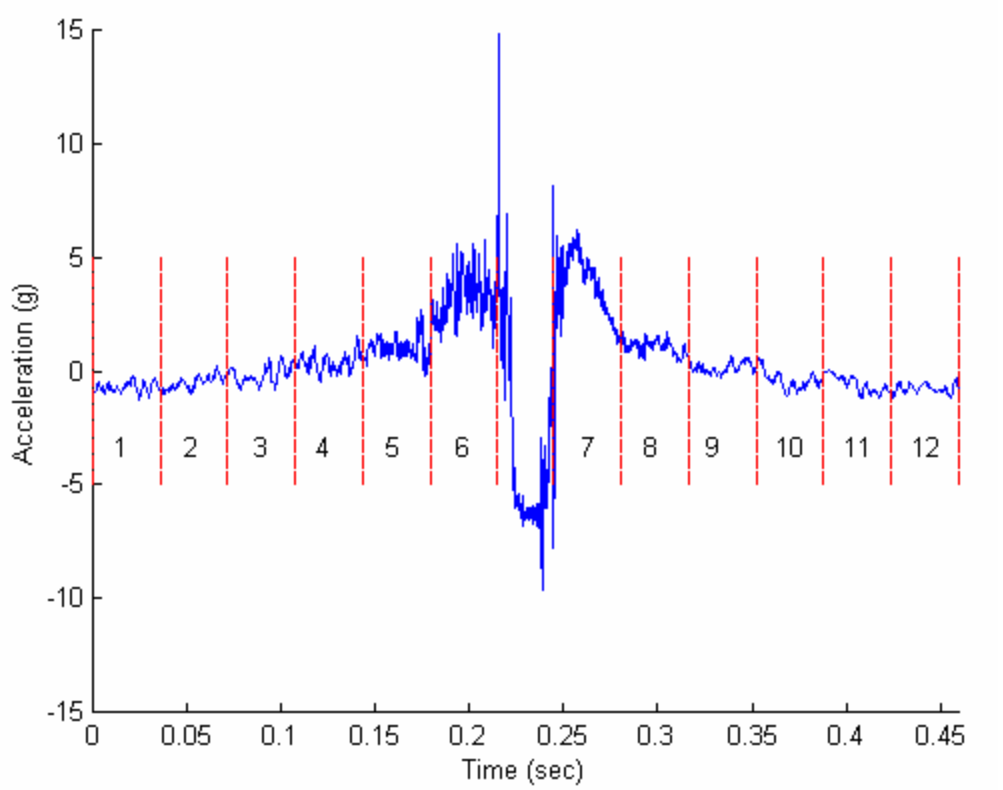

Figure A-7: Segmented time trace of radial acceleration on smooth pavement at 10 mph.

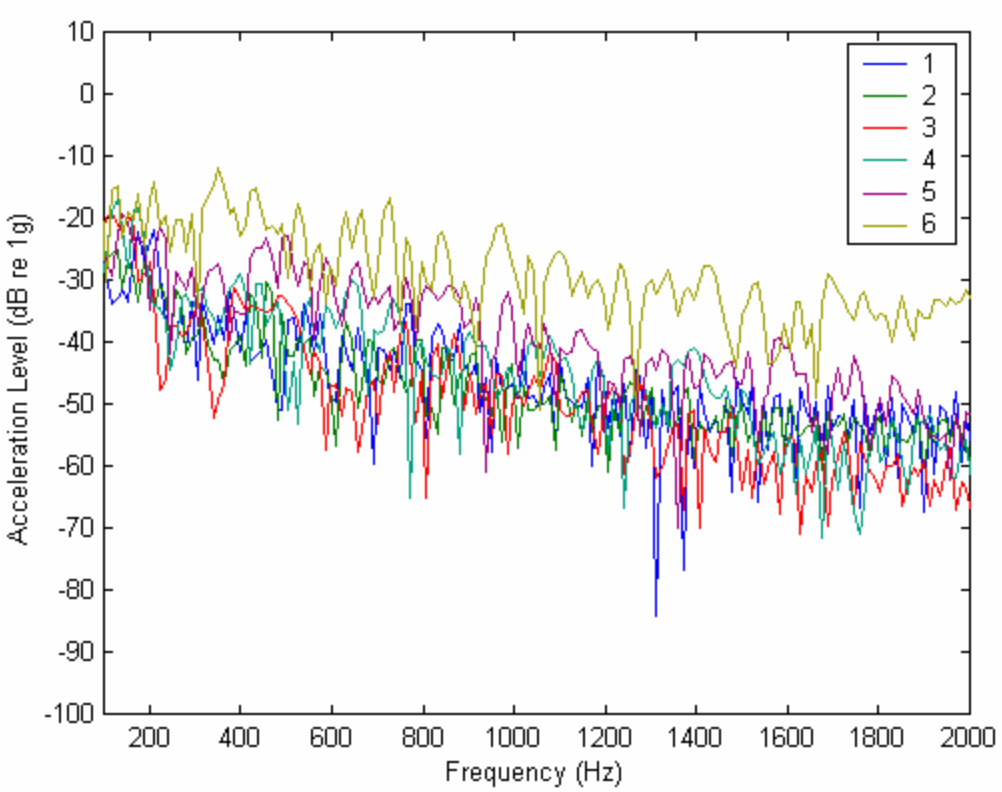

Figure A-8: Vibration spectra of segments in entrance to contact patch measured in the radial direction on smooth pavement at 10 mph. The frequency resolution is 6 Hz.

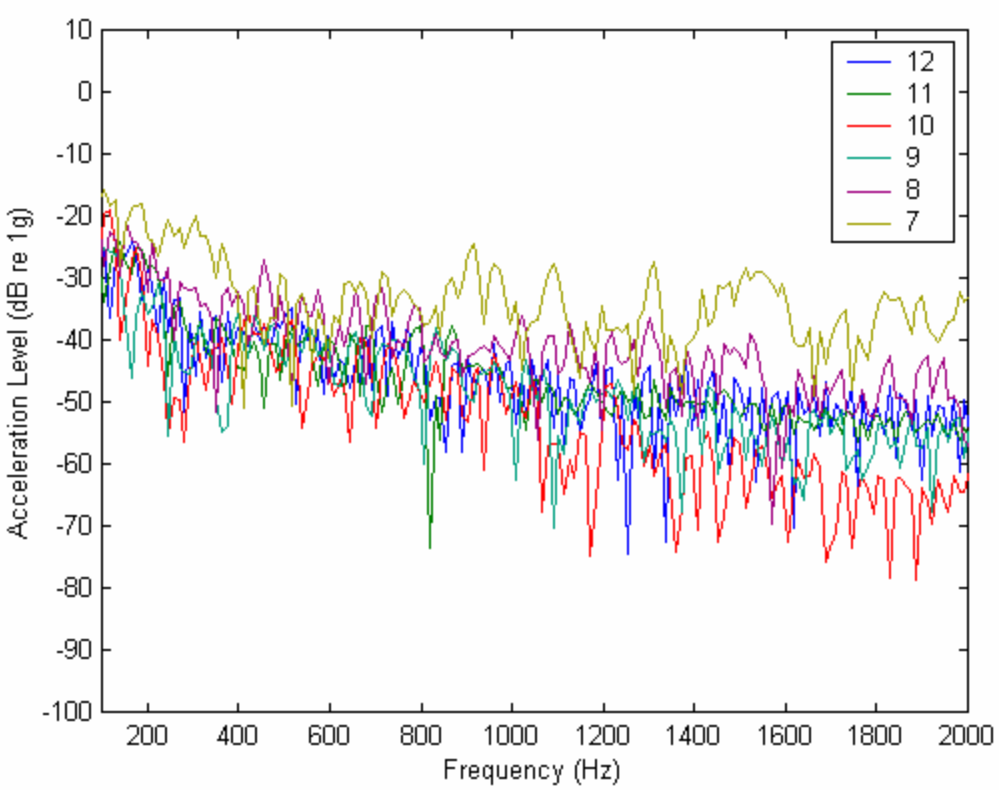

Figure A-9: Vibration spectra of segments in exit to contact patch measured in the radial direction on smooth pavement at 10 mph. The frequency resolution is 6 Hz.

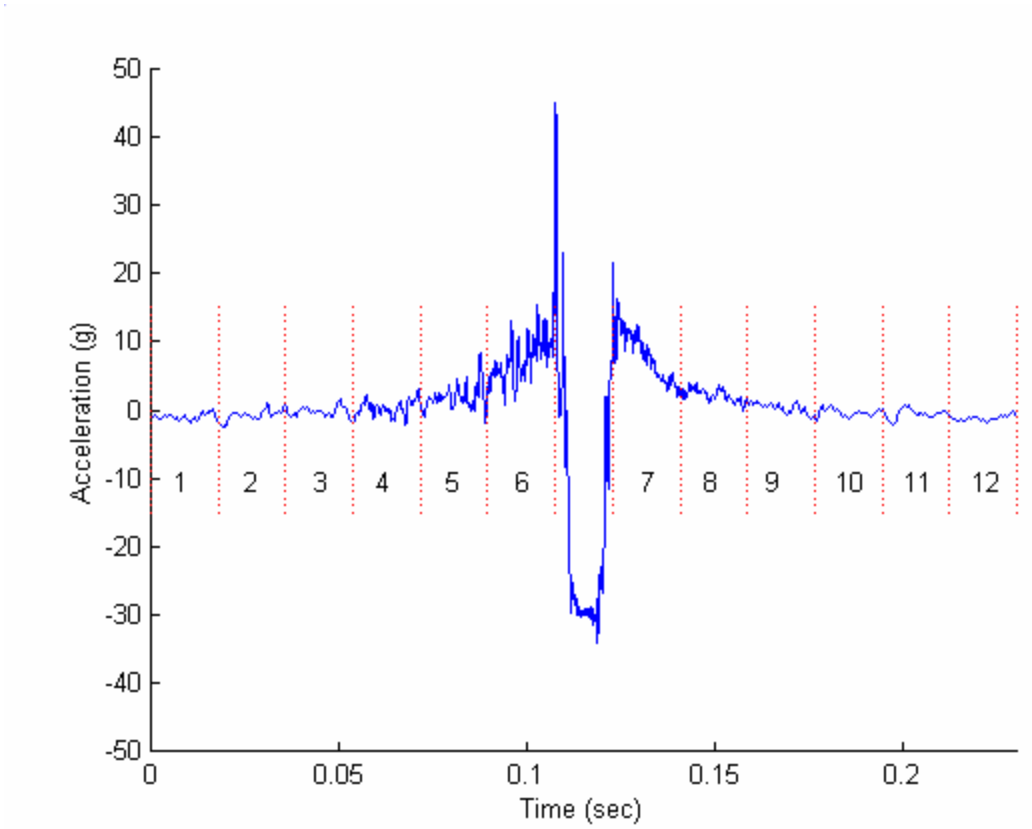

Figure A-10: Segmented time trace of radial acceleration on smooth pavement at 20 mph.

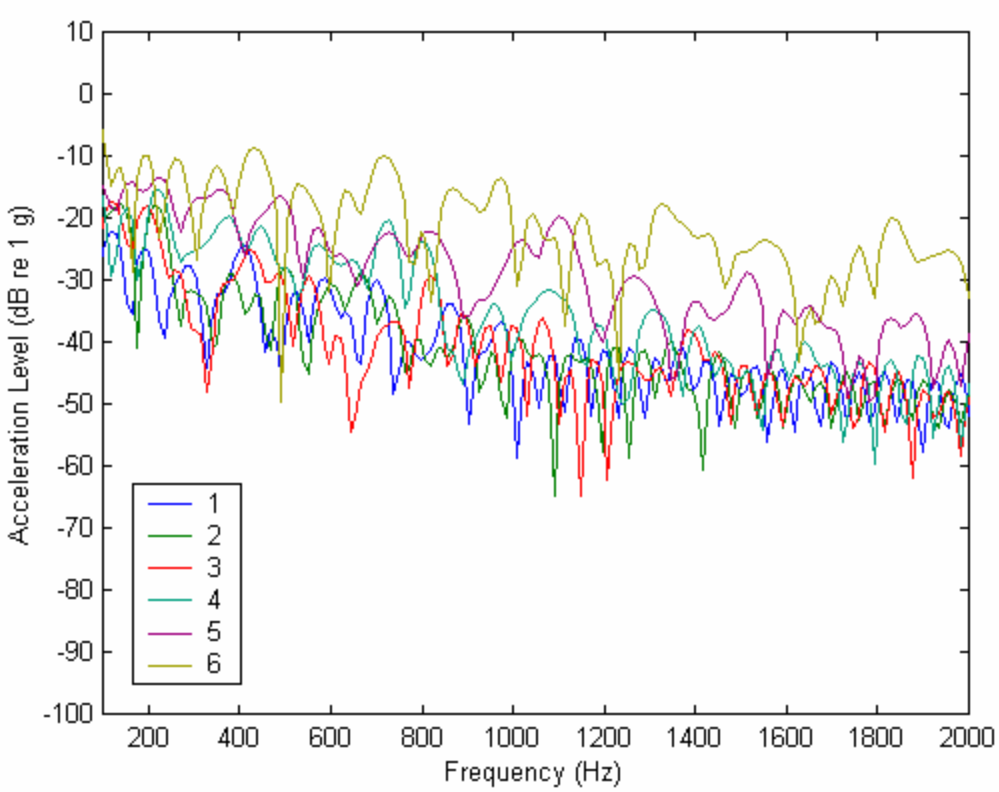

Figure A-11: Vibration spectra of segments in entrance to contact patch measured in the radial direction on smooth pavement at 20 mph. The frequency resolution is 6 Hz.

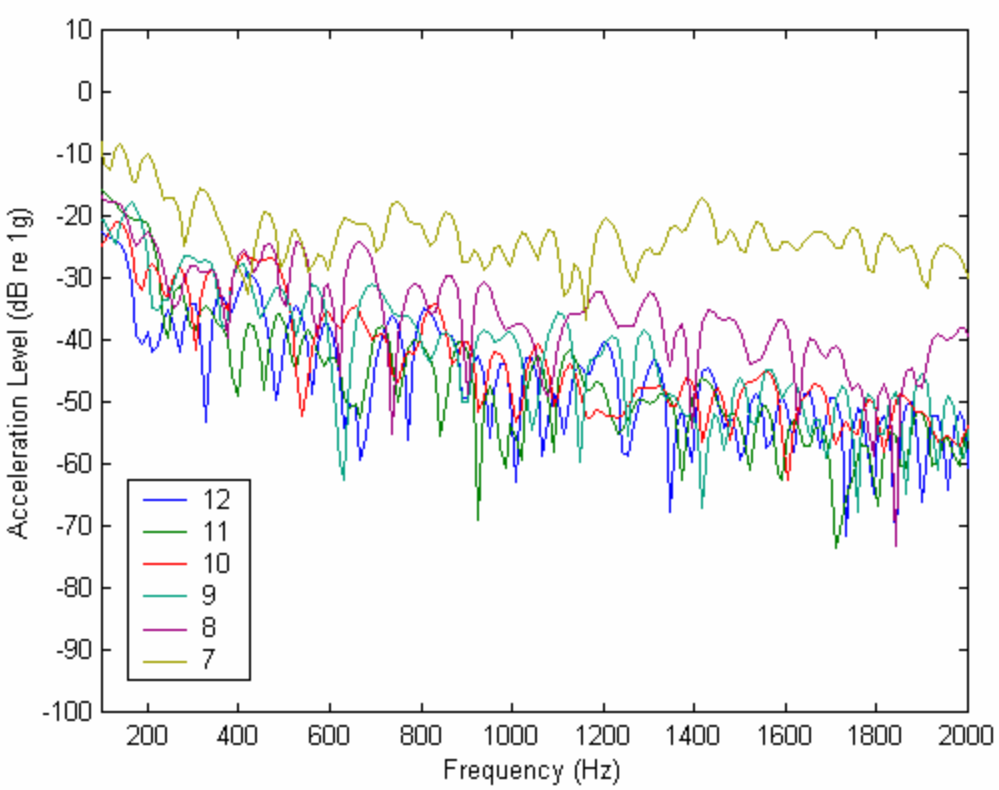

Figure A-12: Vibration spectra of segments in exit to contact patch measured in the radial direction on smooth pavement at 20 mph. The frequency resolution is 6 Hz.

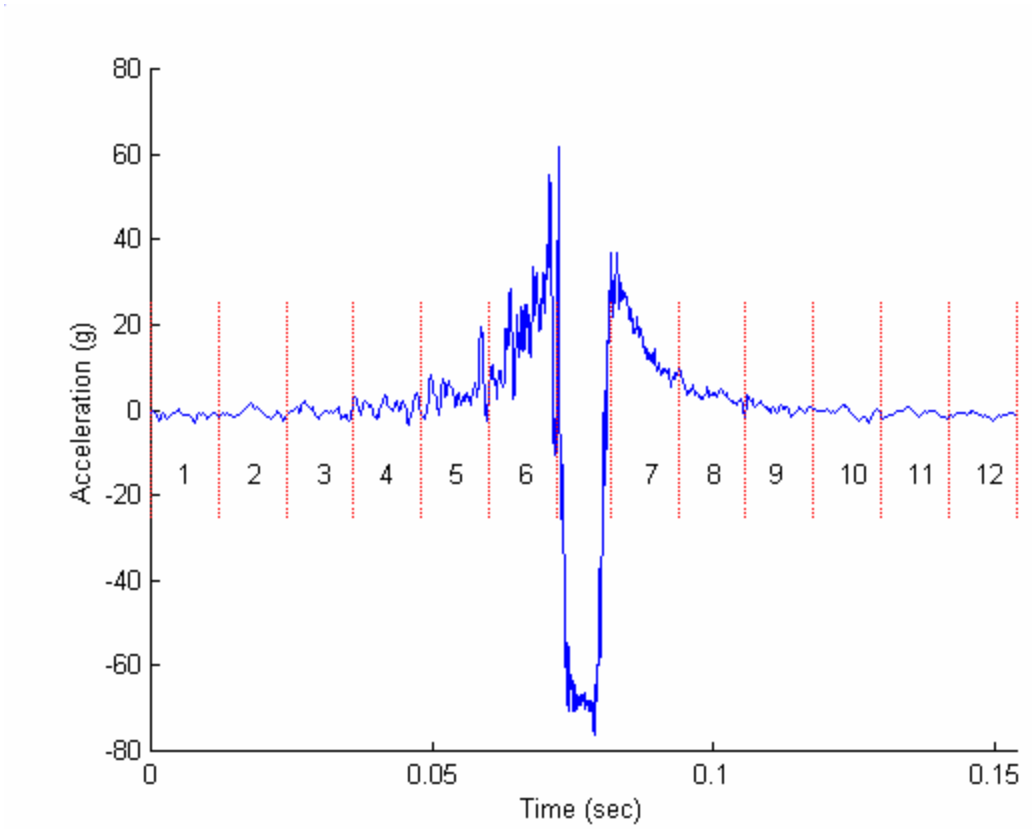

Figure A-13: Segmented time trace of radial acceleration on smooth pavement at 30 mph.

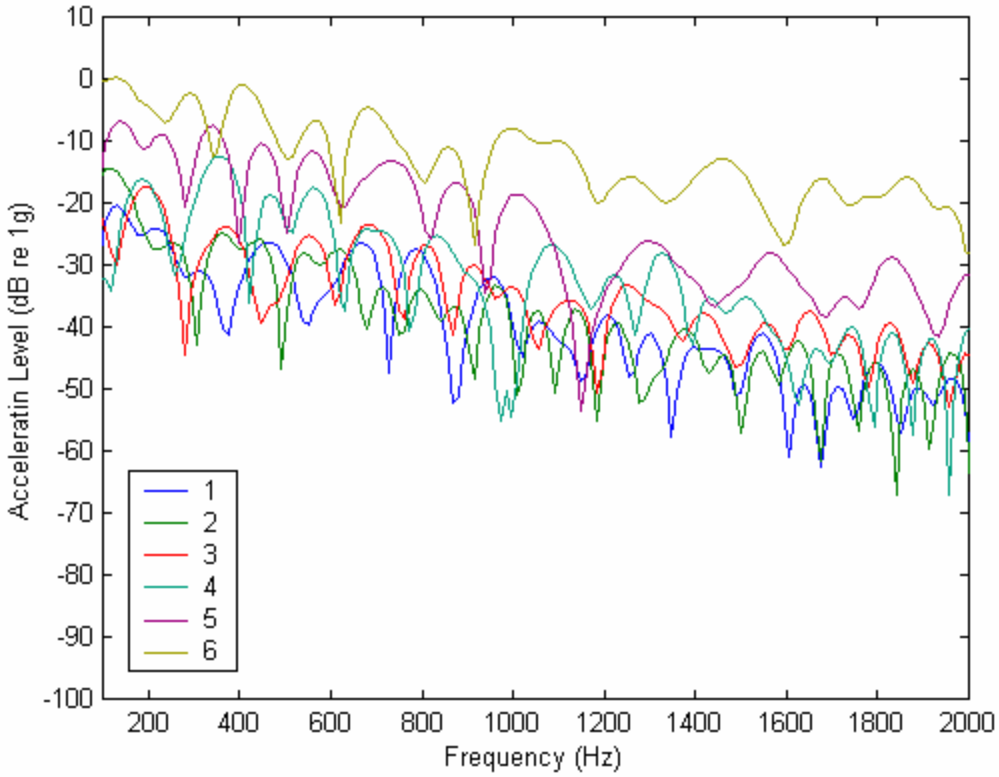

Figure A-14: Vibration spectra of segments in entrance to contact patch measured in the radial direction on smooth pavement at 30 mph. The frequency resolution is 6 Hz.

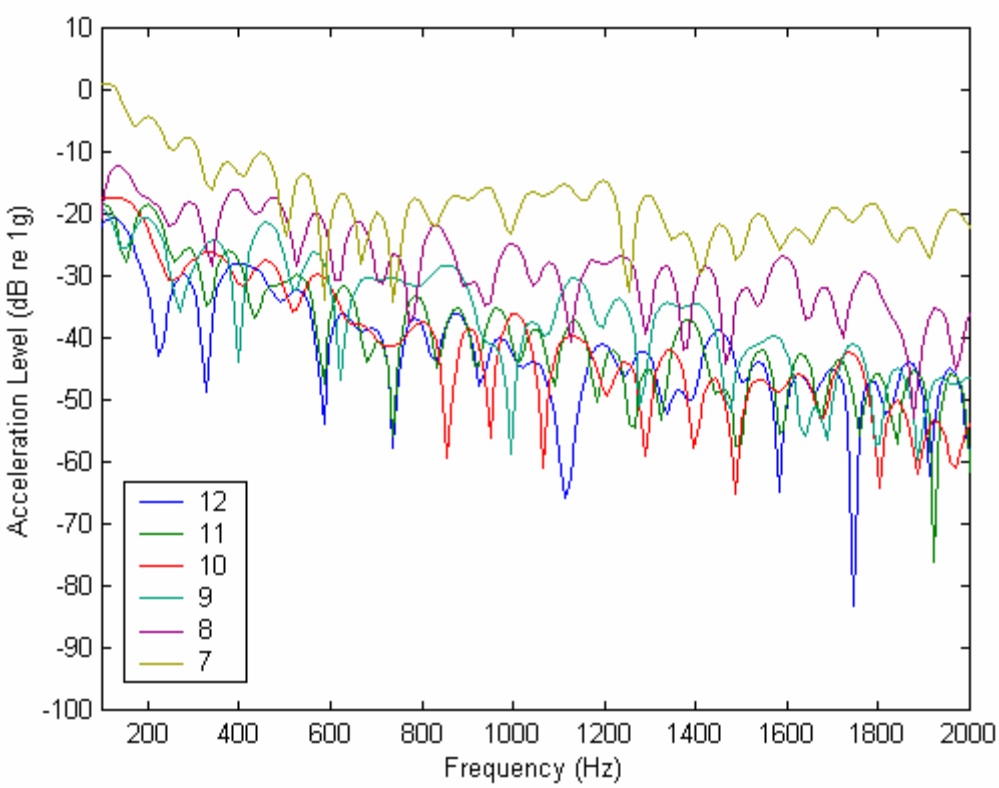

Figure A-15: Vibration spectra of segments in exit to contact patch measured in the radial direction on smooth pavement at 30 mph. The frequency resolution is 6 Hz.

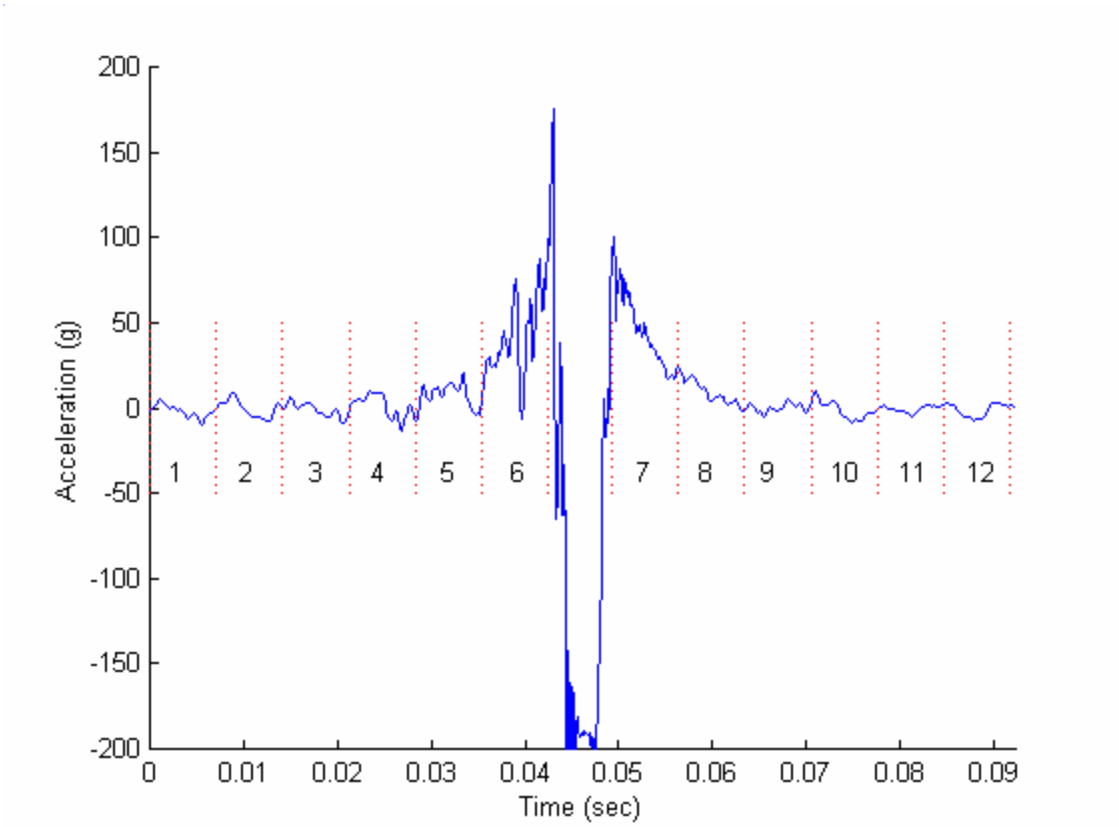

Figure A-16: Segmented time trace of radial acceleration on smooth pavement at 50 mph.

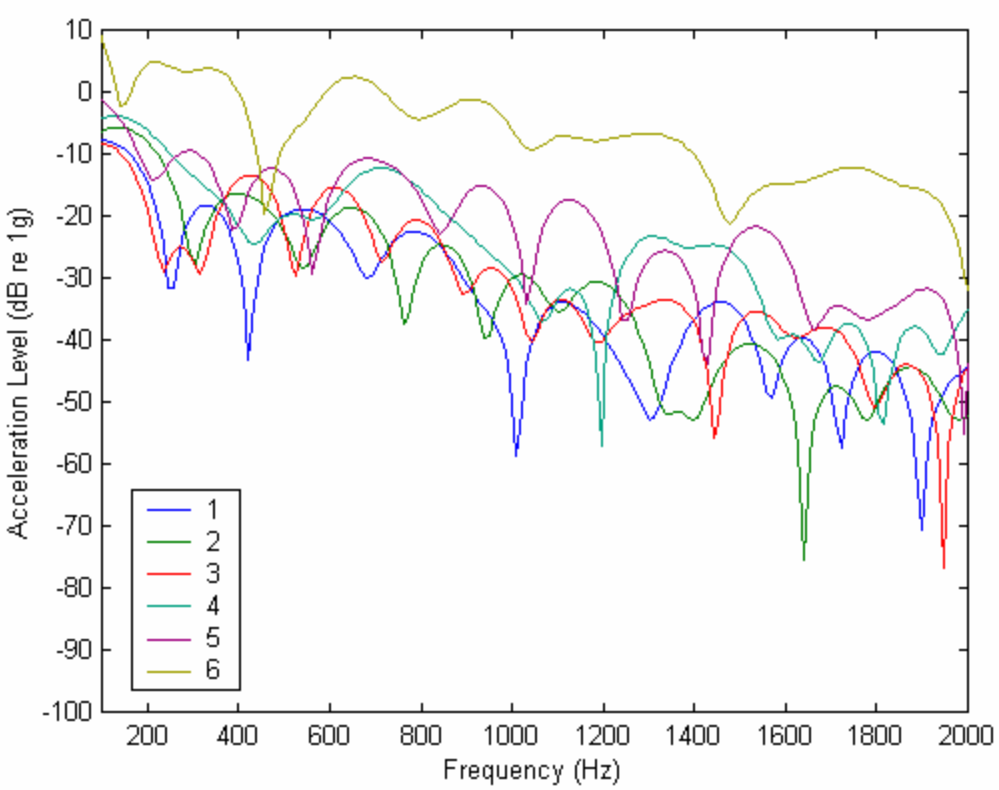

Figure A-17: Vibration spectra of segments in entrance to contact patch measured in the radial direction on smooth pavement at 50 mph. The frequency resolution is 6 Hz.

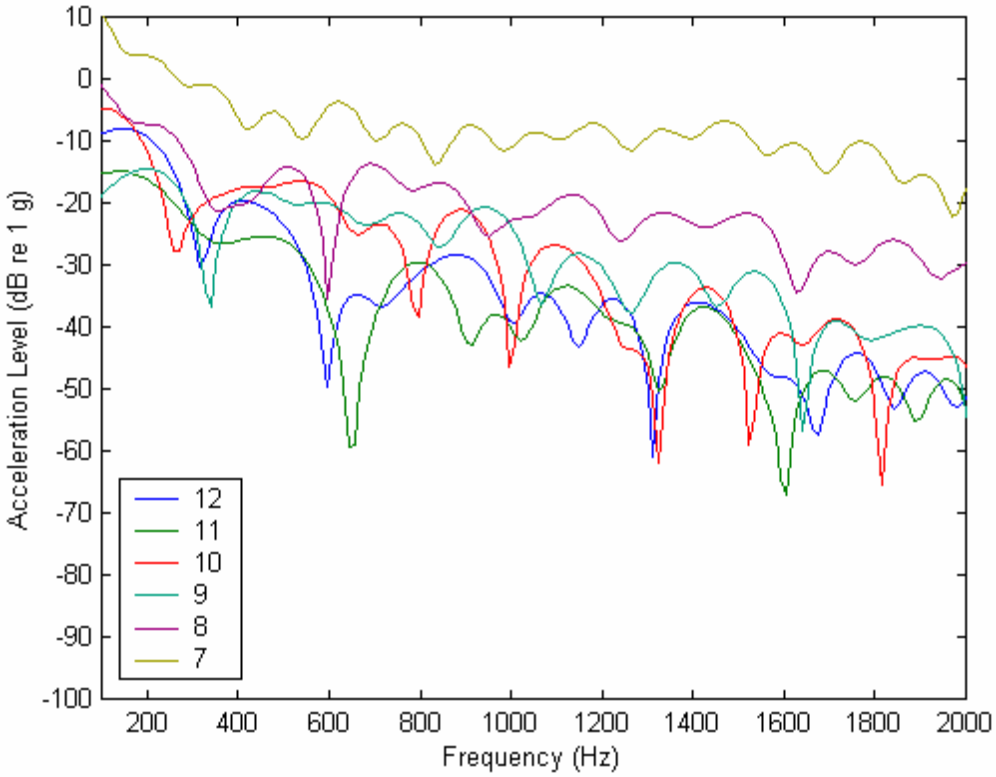

Figure A-18: Vibration spectra of segments in exit to contact patch measured in the radial direction on smooth pavement at 50 mph. The frequency resolution is 6 Hz.

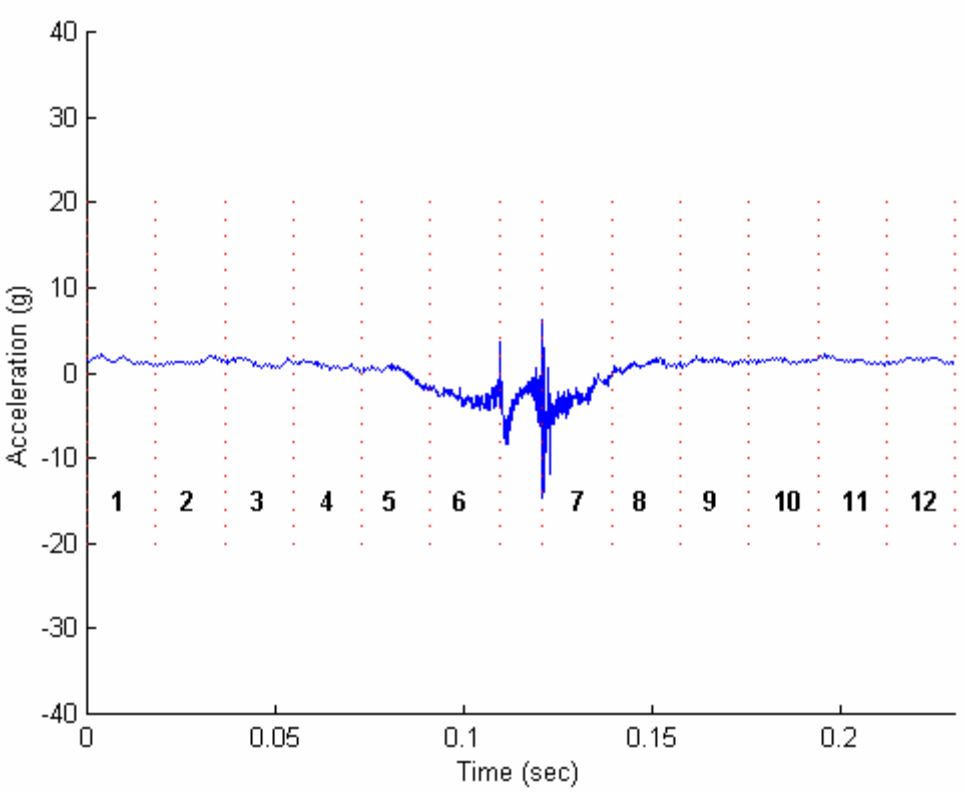

Figure A-19: Segmented time trace of tangential acceleration on smooth pavement at 20 mph.

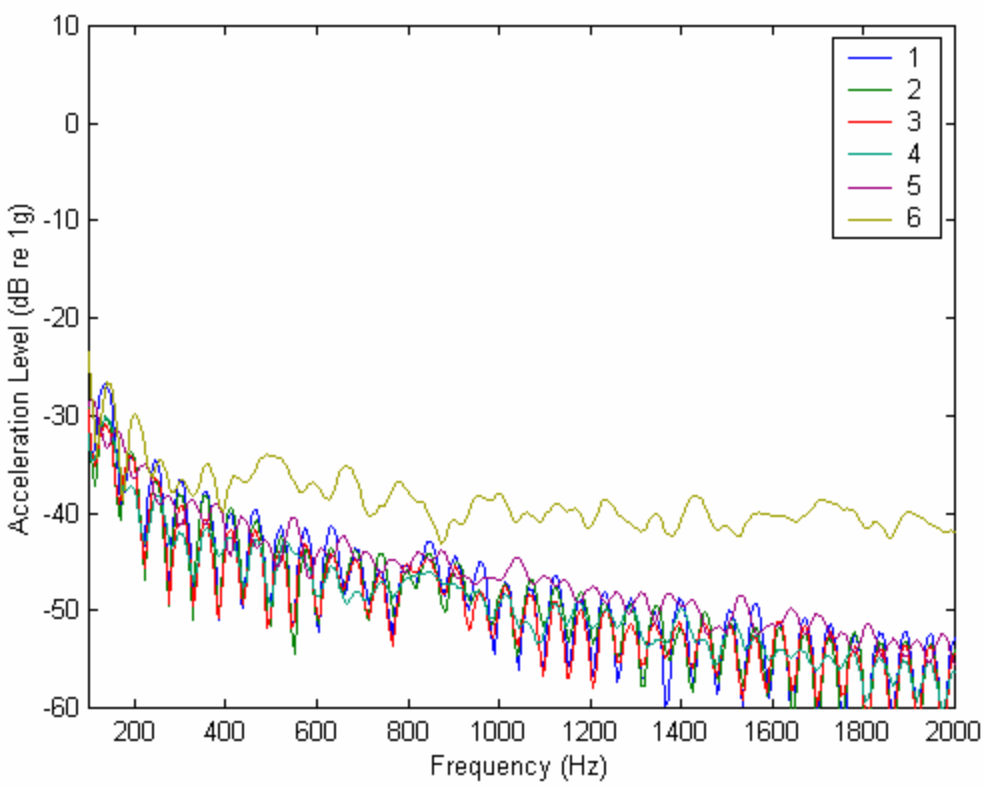

Figure A-20: Vibration spectra of segments in entrance to contact patch measured in the tangential direction on smooth pavement at 20 mph. The frequency resolution is 6 Hz.

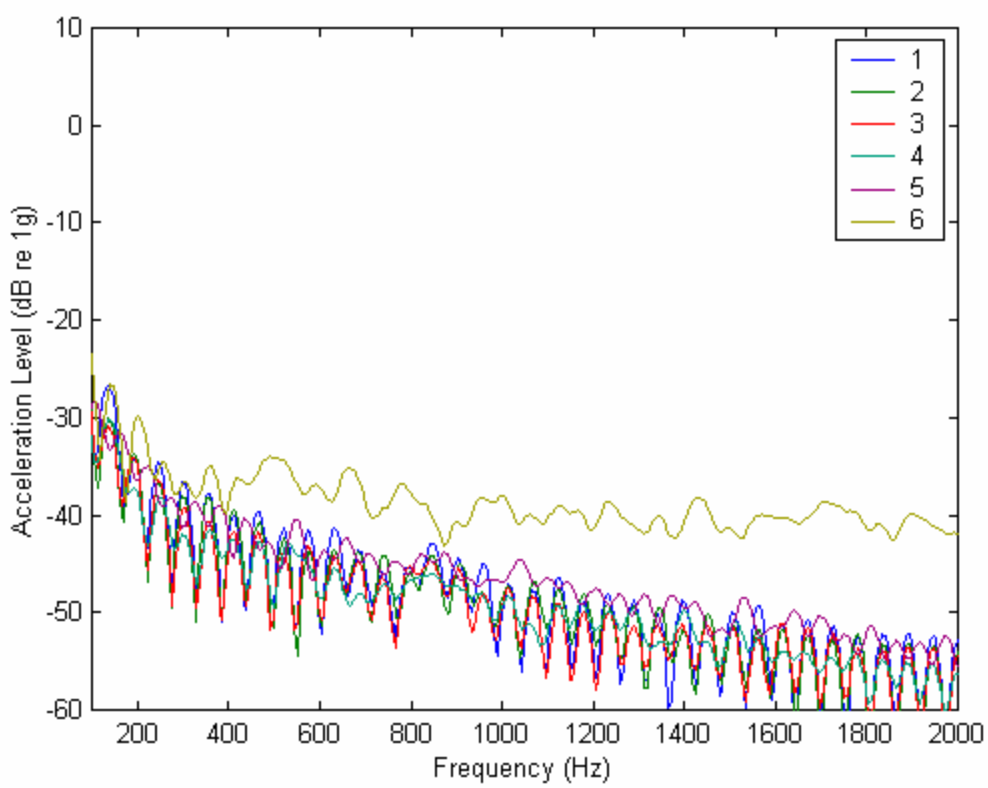

Figure A-21: Vibration spectra of segments in exit to contact patch measured in the tangential direction on smooth pavement at 20 mph. The frequency resolution is 6 Hz.

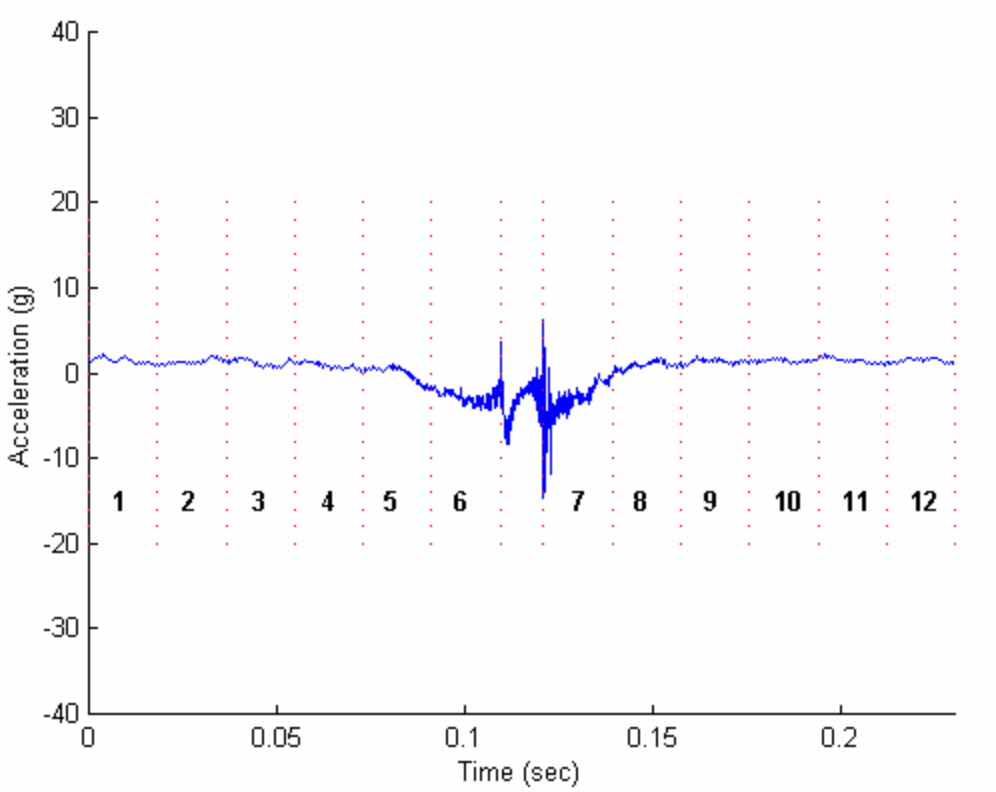

Figure A-22: Segmented time trace of axial acceleration on smooth pavement at 20 mph.

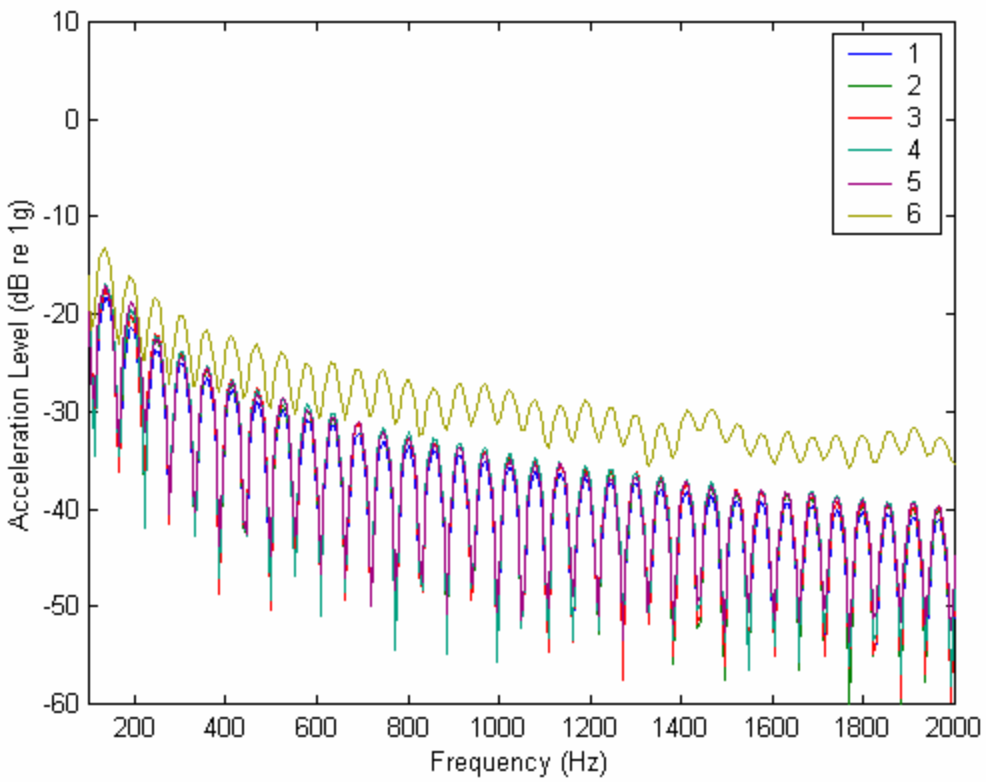

Figure A-23: Vibration spectra of segments in entrance to contact patch measured in the axial direction on smooth pavement at 20 mph. The frequency resolution is 6 Hz.

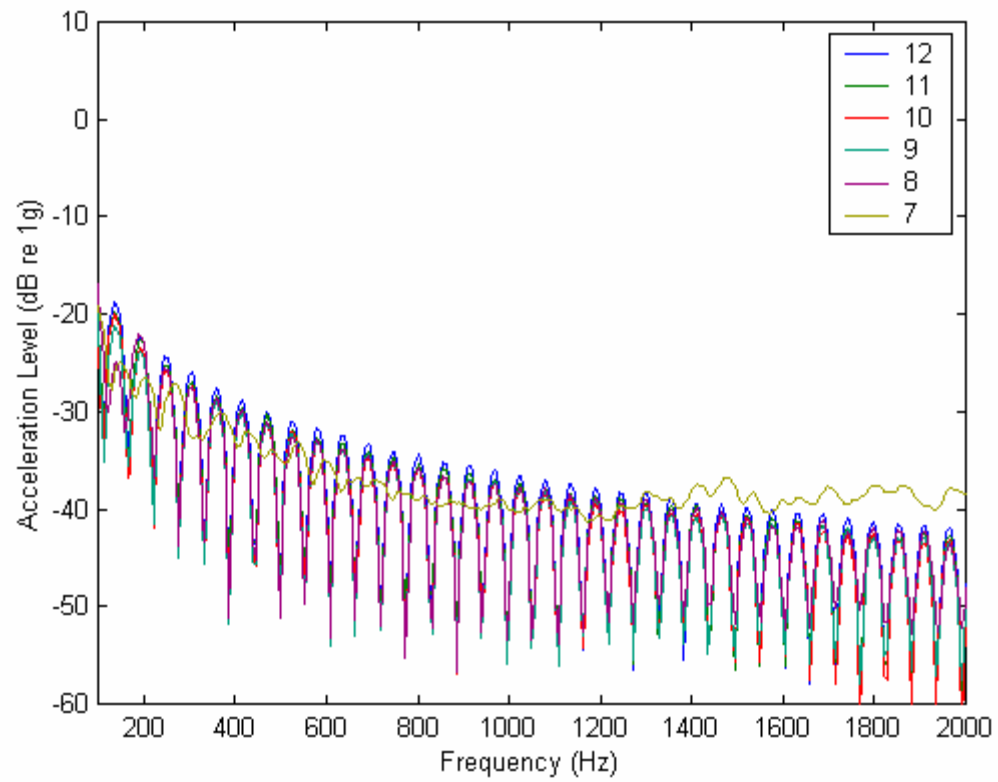

Figure A-24: Vibration spectra of segments in exit to contact patch measured in the axial direction on smooth pavement at 20 mph. The frequency resolution is 6 Hz.

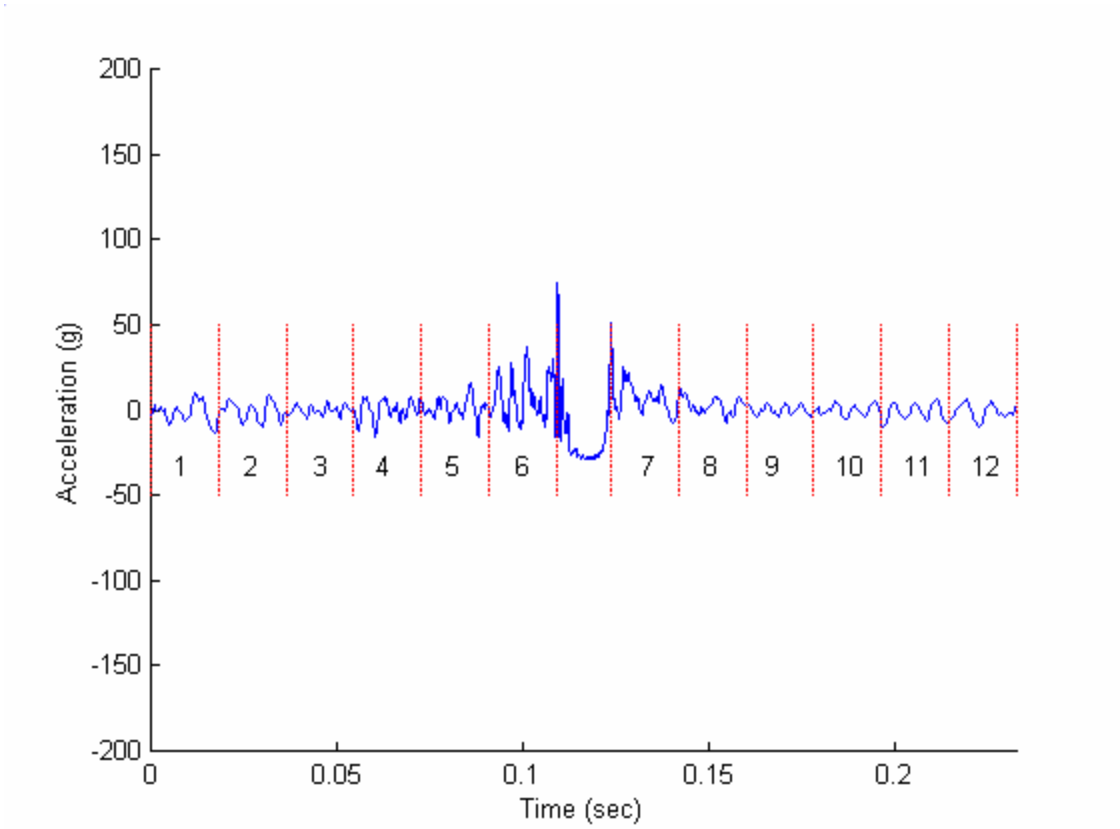

Figure A-25: Segmented time trace of radial acceleration on rough pavement at 20 mph.

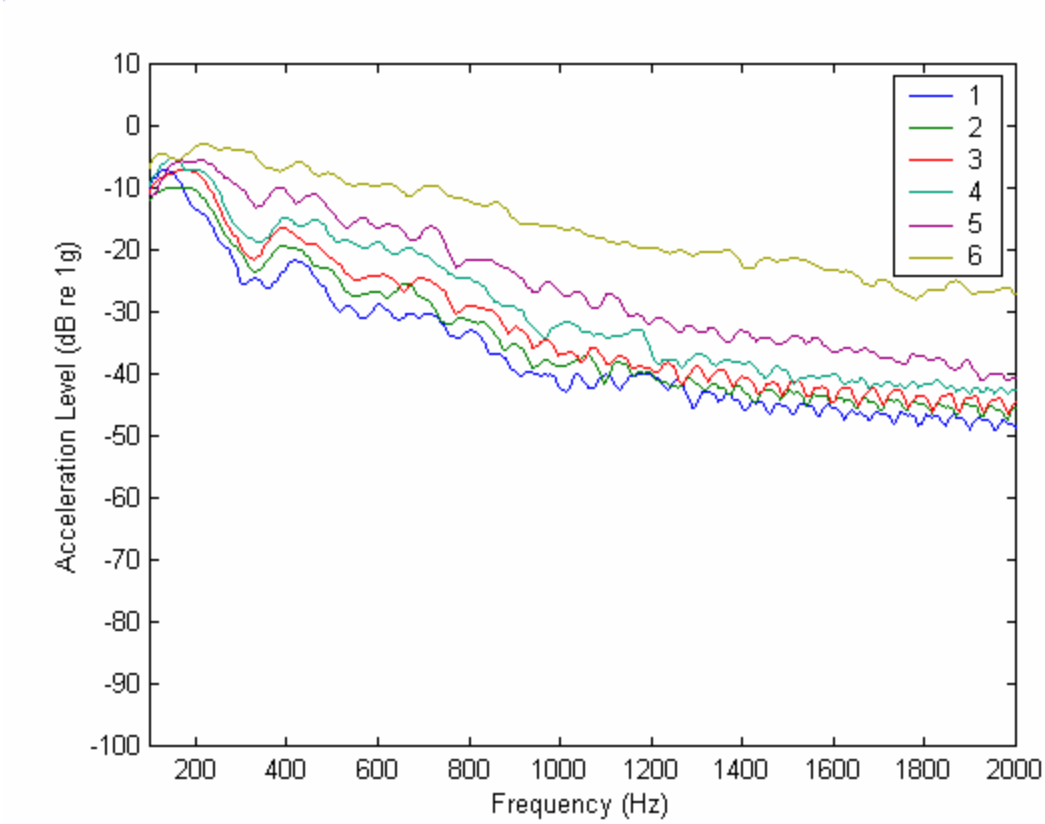

Figure A-26: Vibration spectra of segments in entrance to contact patch measured in the radial direction on rough pavement at 20 mph. The frequency resolution is 6 Hz.

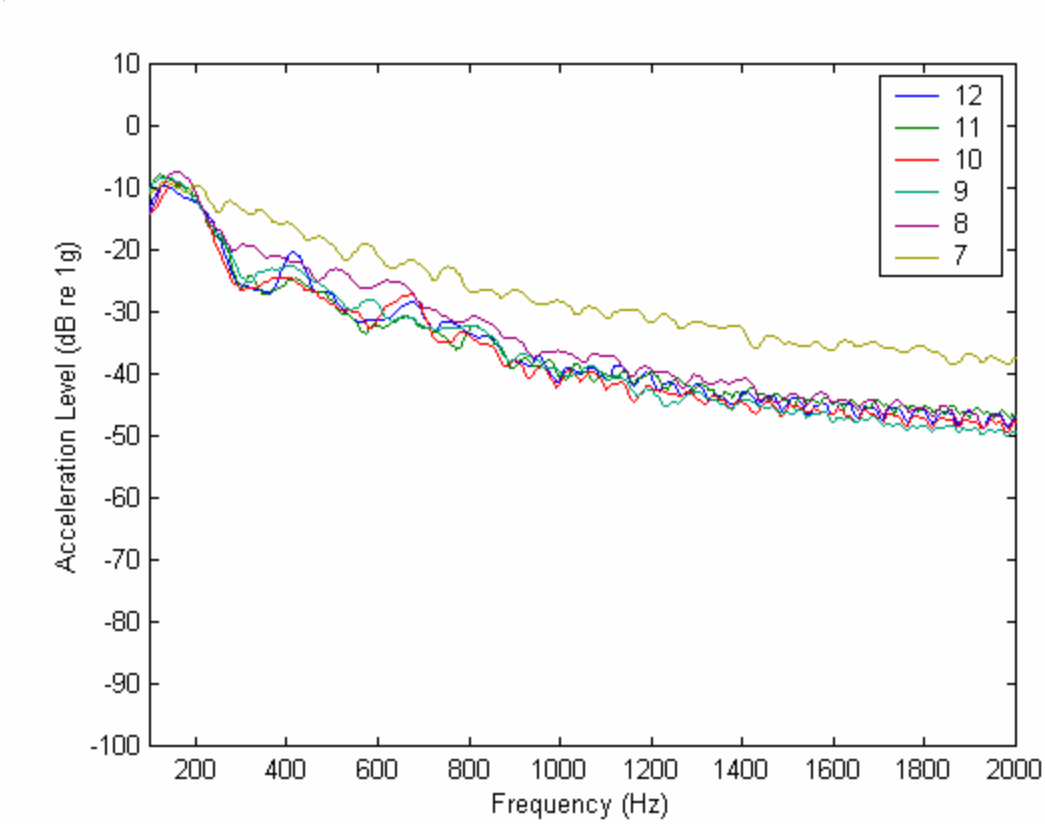

Figure A-27: Vibration spectra of segments in exit to contact patch measured in the radial direction on rough pavement at 20 mph. The frequency resolution is 6 Hz.

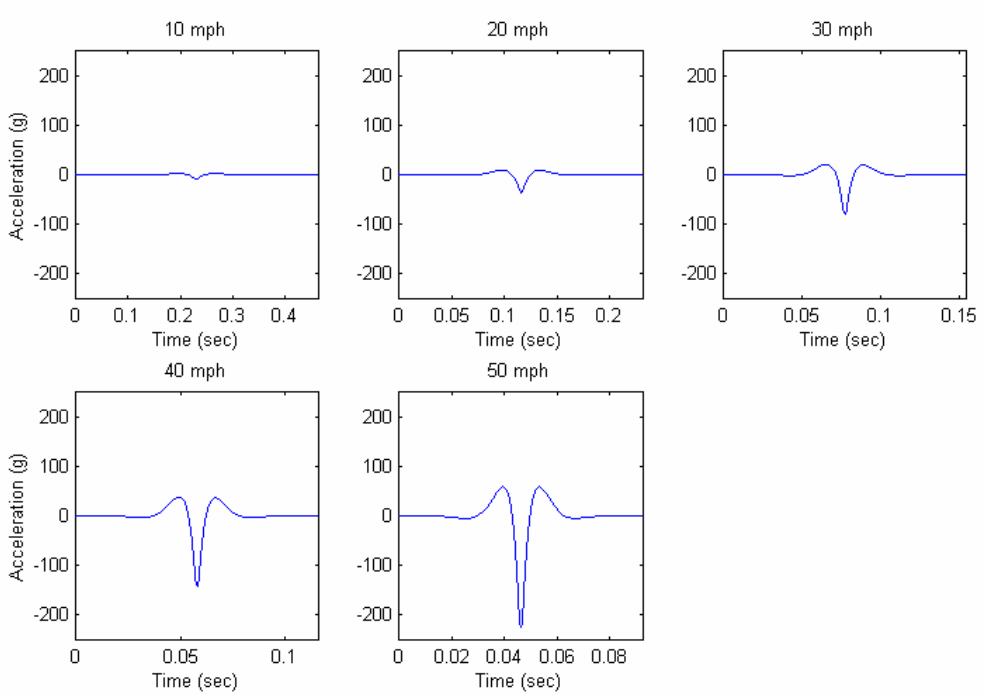

Figure A-28: Analytic model of non-radiating component of radial acceleration for speeds of 10-20 mph.

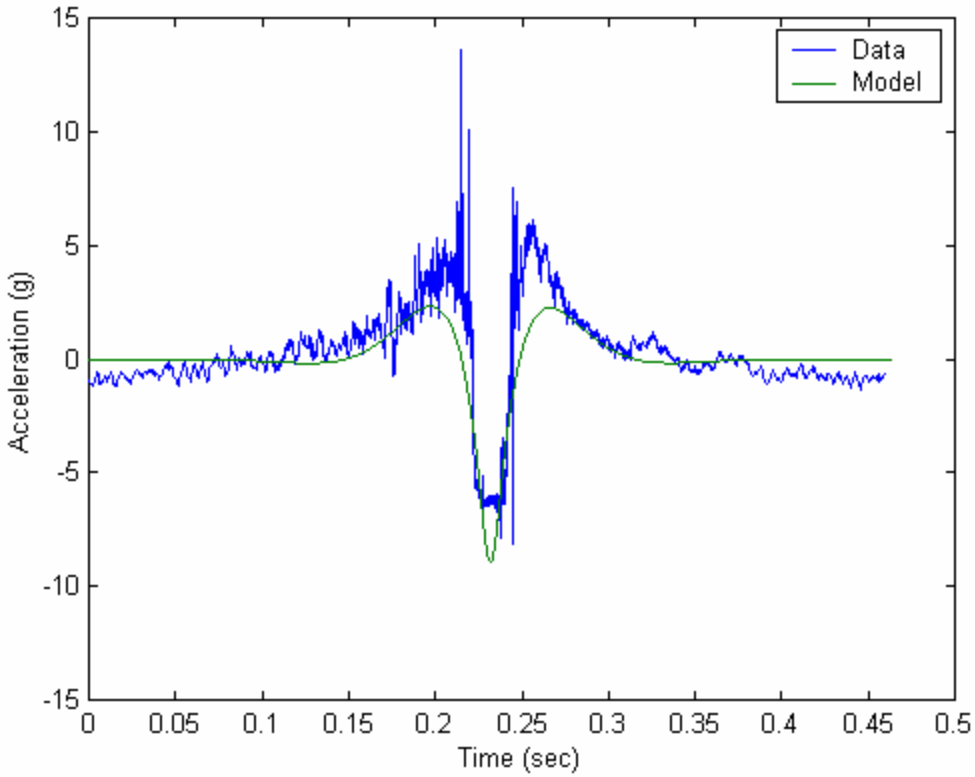

Figure A-29: Analytic model compared with measured radial acceleration at 10 mph on smooth pavement.

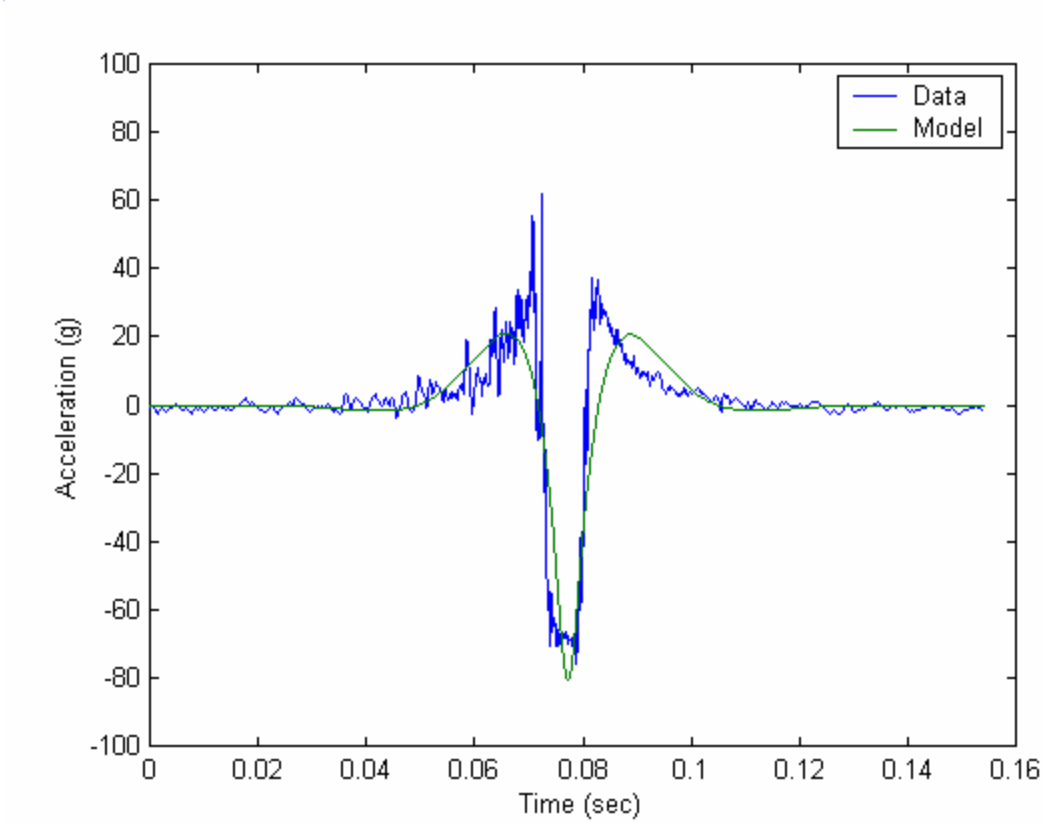

Figure A-30: Analytic model compared with measured radial acceleration at 30 mph on smooth pavement.

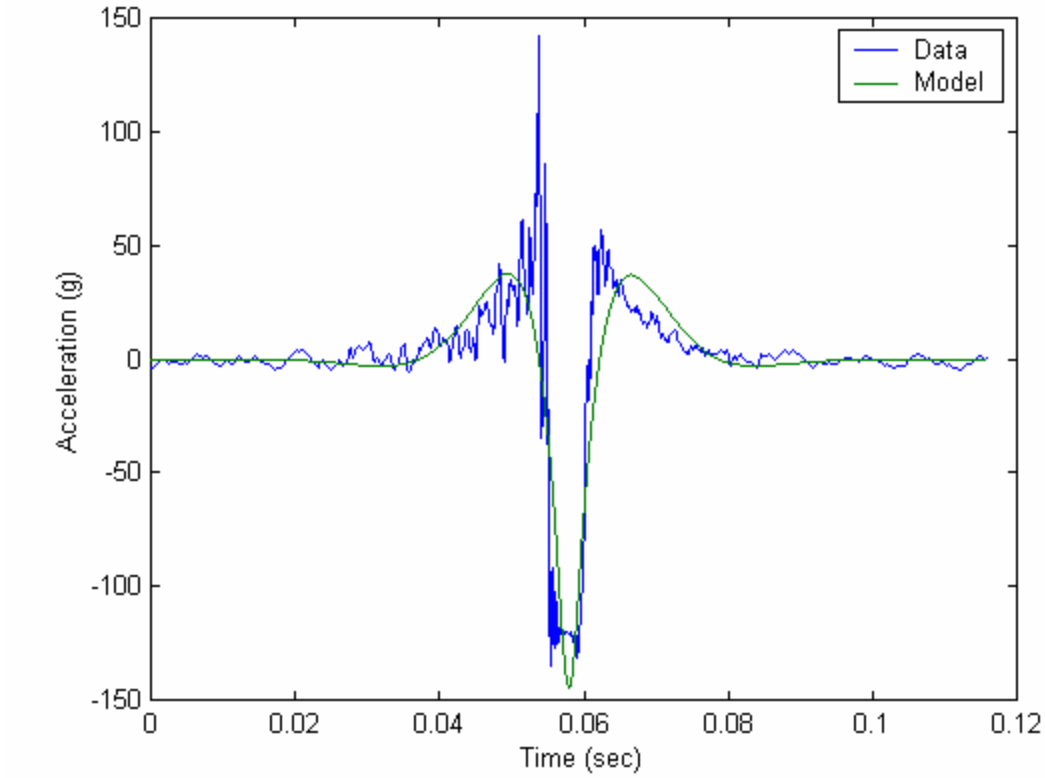

Figure A-31: Analytic model compared with measured radial acceleration at 40 mph on smooth pavement.

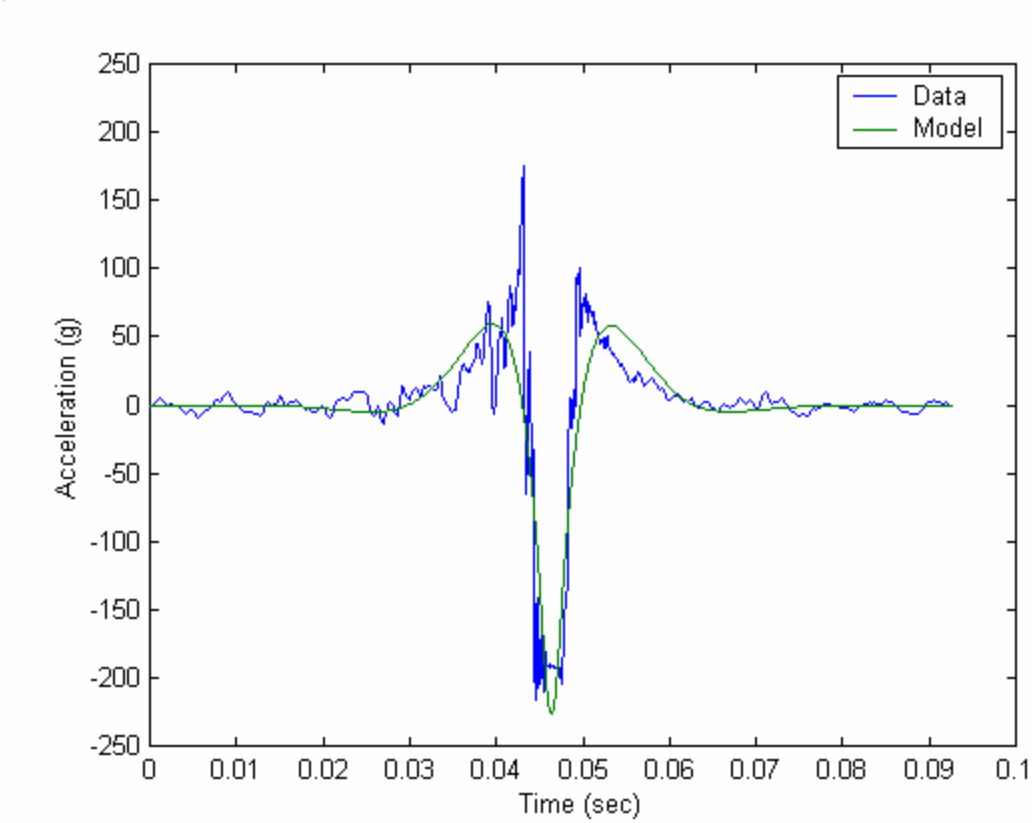

Figure A-32: Analytic model compared with measured radial acceleration at 50 mph on smooth pavement.